Science Advances

AAAS

advances.sciencemag.org/cgi/content/full/4/6/eaat3198/DC1

Supplementary Materials for

Practical water production from desert air

Farhad Fathieh, Markus J. Kalmutzki, Eugene A. Kapustin, Peter J. Waller, Jingjing Yang, Omar M. Yaghi

Published 8 June 2018, *Sci. Adv.* **4**, eaat3198 (2018)
DOI: 10.1126/sciadv.aat3198

The PDF file includes:

- fig. S38. The increase of the sample temperature with time under a flux of 1000 W m^{-2} for MOF-303 and MOF-303/G.
- fig. S39. Diffuse reflectance spectra of zeolite 13X, MOF-801, MOF-801/G, MOF-303, and MOF-303/G recorded between 285 and 2500 nm.
- fig. S40. Absorption spectra of zeolite 13X, MOF-801, MOF-801/G, MOF-303, and MOF-303/G between 285 and 2500 nm.
- fig. S41. Comparison of water sorption kinetics for zeolite 13X, MOF-801, MOF-303, MOF-801/G, and MOF-303/G.
- fig. S42. The temperature response with time under a flux of 1000 W m^{-2} measured for circular pieces of PMMA (diameter, 20 mm) with a thickness of $^1/_4$″ and $^1/_8$″.
- fig. S43. The temperature response with time under a flux of 1000 W m^{-2} measured for circular pieces of PMMA (diameter, 20 mm) of the same thickness ($^1/_4$″) coated with a white (red) and clear coating (black).
- fig. S44. The temperature response with time under a flux of 1000 W m^{-2} measured for circular pieces of PMMA (diameter, 20 mm) of the same thickness ($^1/_4$″) coated with solar absorber coating (Pyromark paint).
- fig. S45. Absorption of PMMA (blue) compared to the spectral irradiance of the sun (red) and an incandescent lamp (orange) between 285 and 3000 nm.
- fig. S46. Comparison of absorption spectra for PMMA (light blue), PMMA coated with primer (light gray), and PMMA coated with white paint (orange).
- fig. S47. Water sorption unit.
- fig. S48. Schematic of the case, cover, and water sorption unit with dimensions.
- fig. S49. Locations of thermocouples and humidity sensors inside the case.
- fig. S50. Calibration curve for humidity sensor converting the voltage output readings into the corresponding RH.
- fig. S51. Calibration curve for the temperature sensor.
- fig. S52. Artificial solar irradiance for low flux condition.
- fig. S53. Artificial solar irradiance for high flux condition.
- fig. S54. Image of the artificial flux generator in two lamps configuration.
- fig. S55. Relative humidity and temperature profiles for empty sorbent container under low flux artificial solar irradiance.
- fig. S56. Relative humidity and temperature profiles for 0.25 kg graphite under low flux artificial solar irradiance.
- fig. S57. Relative humidity and temperature profiles for 0.5 kg of zeolite 13X under low flux artificial solar irradiance.
- fig. S58. Relative humidity and temperature profiles for 0.5 kg of zeolite 13X under high flux artificial solar irradiance.
- fig. S59. Relative humidity and temperature profiles for 1.65 kg of MOF-801/G under low flux artificial solar irradiance.
- fig. S60. Relative humidity and temperature profiles for 1.65 kg of MOF-801/G under high flux artificial solar irradiance.
- fig. S61. Relative humidity and temperature profiles for 0.825 kg of MOF-801/G under low flux artificial solar irradiance.

- table S1. Crystal data and structure determination for MOF-303 with single crystal data set.
- table S2. Atomic positions for MOF-303 from the Pawley refinement model.
- table S3. The average hemispherical absorptivity and transmissivity of materials for artificial and solar radiation within the range of 285 to 2500 nm.
- table S4. Test conditions for the water harvesting in the laboratory.
- table S5. The performance parameters for water production under laboratory conditions.
- table S6. Total flux received by different sorbents for the laboratory experiment using low and high fluxes.
- Legends for movies S1 to S4
- References (*24*–*32*)

Other Supplementary Material for this manuscript includes the following:
(available at advances.sciencemag.org/cgi/content/full/4/6/eaat3198/DC1)

- movie S1 (.mp4 format). Initial stage of water condensation on the side walls of the case at 10,000% speed.
- movie S2 (.mp4 format). Formation of running droplets of water on the side walls of the case at 10,000% speed.
- movie S3 (.mp4 format). Coalescence of water droplets into puddles of liquid water at the condenser at 700% speed.
- movie S4 (.mp4 format). Collision of puddles of liquid water at the bottom of the case at 1000% speed.

section S1. Materials and analytical techniques for MOF synthesis and analysis

section S1.1. Materials

Zirconium oxychloride octahydrate ($ZrOCl_2 \cdot 8H_2O$, purity ≥ 99.8%), aluminum chloride hexahydrate ($AlCl_3 \cdot 6H_2O$, purity ≥ 99.8%), *N*,*N*-dimethylformamide (DMF) (HPLC grade), fumaric acid (purity ≥ 99%), 3,5-pyrazoledicarboxylic acid monohydrate (H_3PDC) (purity ≥ 97%), Zeolite 13X, sodium hydroxide were purchased form Sigma-Aldrich Co. Anhydrous DMF and formic acid (purity ≥ 99.8%) were obtained from EMD Millipore Chemicals. Extra-fine graphite powder was obtained from AGS Company. Methanol (HPLC grade) was purchased from Fisher Scientific. Deuterated solvents were obtained from Cambridge Isotope Laboratories. All chemicals obtained were used without further purification. Pyrex screw-capped media storage jars were used for synthesis, solvent exchange and storage.

section S1.2. Analytical techniques

Powder X-ray diffraction (PXRD) patterns were acquired with a Bruker D8 Advance diffractometer (Göbel-mirror monochromated Cu Kα1 radiation, λ = 1.54056 Å). Single crystal X-ray diffraction (SXRD) data of MOF-303 was collected using as-synthesized crystals at beamline 11.3.1 of the Advanced Light Source at Lawrence Berkeley National Lab. N_2 adsorption isotherms were recorded on a Quantachrome Quadrasorb-SI volumetric gas adsorption analyzer. A liquid nitrogen bath was used for the measurements at 77 K. The framework density of all MOF and MOF/G samples was measured using a pycnometer (Ultrapyc 1200e, Quantachrome). Attenuated-total-reflectance Fourier-transform infrared (ATR-FTIR) spectra were recorded on a Bruker ALPHA Platinum ATR-FTIR Spectrometer. Thermogravimetric analysis (TGA) traces was measured on a TA Instruments SDT Q600 series thermal gravimetric analyze. Gases were humidified by bubbling dry air through a 2 L bubbler humidifier before advection into the TGA chamber. The humidity and temperature were monitored using high-accuracy thermocouples and humidity sensors upstream the TGA chamber. Water isotherms and cyclic stability test were measured on a BEL Japan BELSORP-aqua3, and the water uptake estimated in cubic centimeters per gram. Prior to the water adsorption measurements, water (analyte) was flash frozen under liquid nitrogen and then evacuated under dynamic vacuum for at least three times to remove any gases in the water reservoir. The measurement temperature was controlled using a water circulator. Helium was used to estimate the dead space for both, gas and water adsorption measurements. Ultrahigh purity N_2, and He (Praxair, 99.999% purity) were used throughout all experiments. Scanning electron microscope (SEM) and energy-dispersive X-ray spectroscopy (EDS) images were recorded on a FEI Quanta 3D scanning electron microscope with 10 kV accelerating voltage. ^{1}H-NMR spectra were recorded with a Bruker DRX-500 spectrometer operating at 500 MHz. The aluminum and zirconium content in samples of harvested water were analyzed using an ICP-AES spectroscope (Optima 7000 DV, Perkin

Elmer). Diffuse reflectance spectra between 285 and 2500 nm were recorded on a Varian Cary 5000 spectrometer and absorption spectra between 285 and 3000 nm were recorded using a Shimadzu UV3600.

section S2. MOF-801 synthesis and characterization

section S2.1. Synthesis of MOF-801 microcrystalline powder

Pre-scaled-up synthesis of MOF-801, $Zr_6O_4(OH)_4$(fumarate)$_6$: In a 100 mL screw-capped jar, 1.16 g (50 mmol) of fumaric acid and 3.2 g (50 mmol) of $ZrOCl_2 \cdot 8H_2O$ were dissolved in a mixed solvent of DMF and formic acid (40 mL and 14 mL, respectively). The mixture was then heated in an isothermal oven at 130 ºC for 10 hours to give as-prepared MOF-801 as a white precipitate. The precipitate was collected by filtration using a membrane filter (45 µm pore size), washed three times daily with 100 mL DMF for three days, then three times daily with 100 mL methanol for three days, and subsequently dried in air. The air-dried MOF sample was transferred to a vacuum chamber. The chamber was first evacuated at room temperature for 5 hours until the pressure dropped below 1 kPa. After that, the sample was heated in vacuum at 70 ºC for 12 hours, and then at 150 ºC for another 48 hours yielding activated MOF-801 as a white powder (yield: 2 g). This batch was further used to determine the water sorption characteristic curves and TGA kinetics for adsorption and desorption.

Scaled-up synthesis: In a typical procedure in a 500 mL screw-capped jar, 5.8 g (50 mmol) of fumaric acid and 16 g (50 mmol) of $ZrOCl_2 \cdot 8H_2O$ were dissolved in a mixed solvent of DMF and formic acid (200 mL and 70 mL, respectively). The mixture was then heated in an isothermal oven at 130 ºC overnight to give as-prepared MOF-801 as a white precipitate. Yield: ~10 g. The combined precipitate from five reaction jars was collected, washed three times daily with 500 mL DMF for three days, then three times daily with 500 mL methanol for three days, and subsequently dried in air.

section S2.2. MOF-801 scaled-up activation

Air-dried MOF sample was transferred into a vacuum chamber. The chamber was first evacuated at room temperature for 5 hours until the pressure dropped below 1 kPa. After that, the sample was heated in vacuum at 70 ºC for 12 hours, and then at 150 ºC for another 48 hours. The combined product from 140 jars was then placed in the drying oven on an aluminum pan at 160 ºC for 10 days prior to the water production experiment. Overall, the yield of activated microcrystalline MOF-801 powder was 1100 g.

section S2.3. Characterization of activated MOF-801

PXRD, EDS analysis, and SEM images: Activated microcrystalline MOF-801 was examined by PXRD. A ground sample was placed on a zero-background sample holder and mounted on the diffractometer. The data was collected from 3 to 50 degrees with a step width of 0.01 and total data collection time of 30 minutes. SEM and EDS measurements were performed to study the morphology and elemental composition of bulk MOF powder.

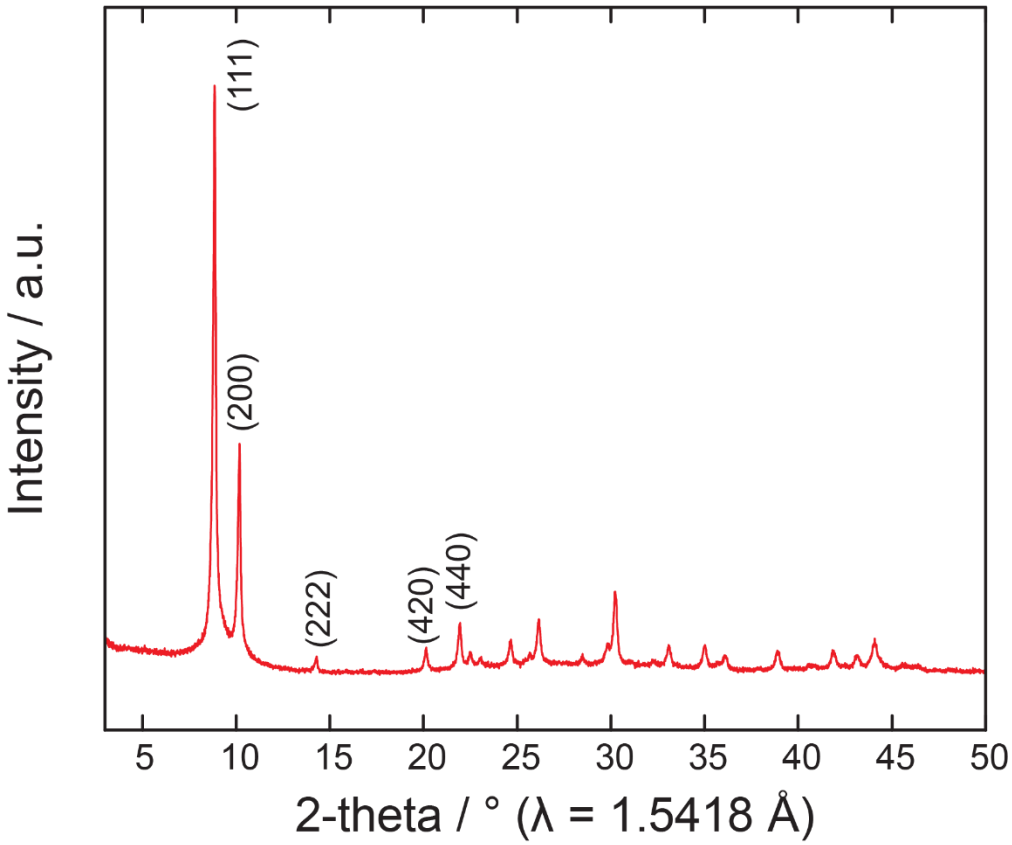

fig. S1. PXRD pattern of activated MOF-801.

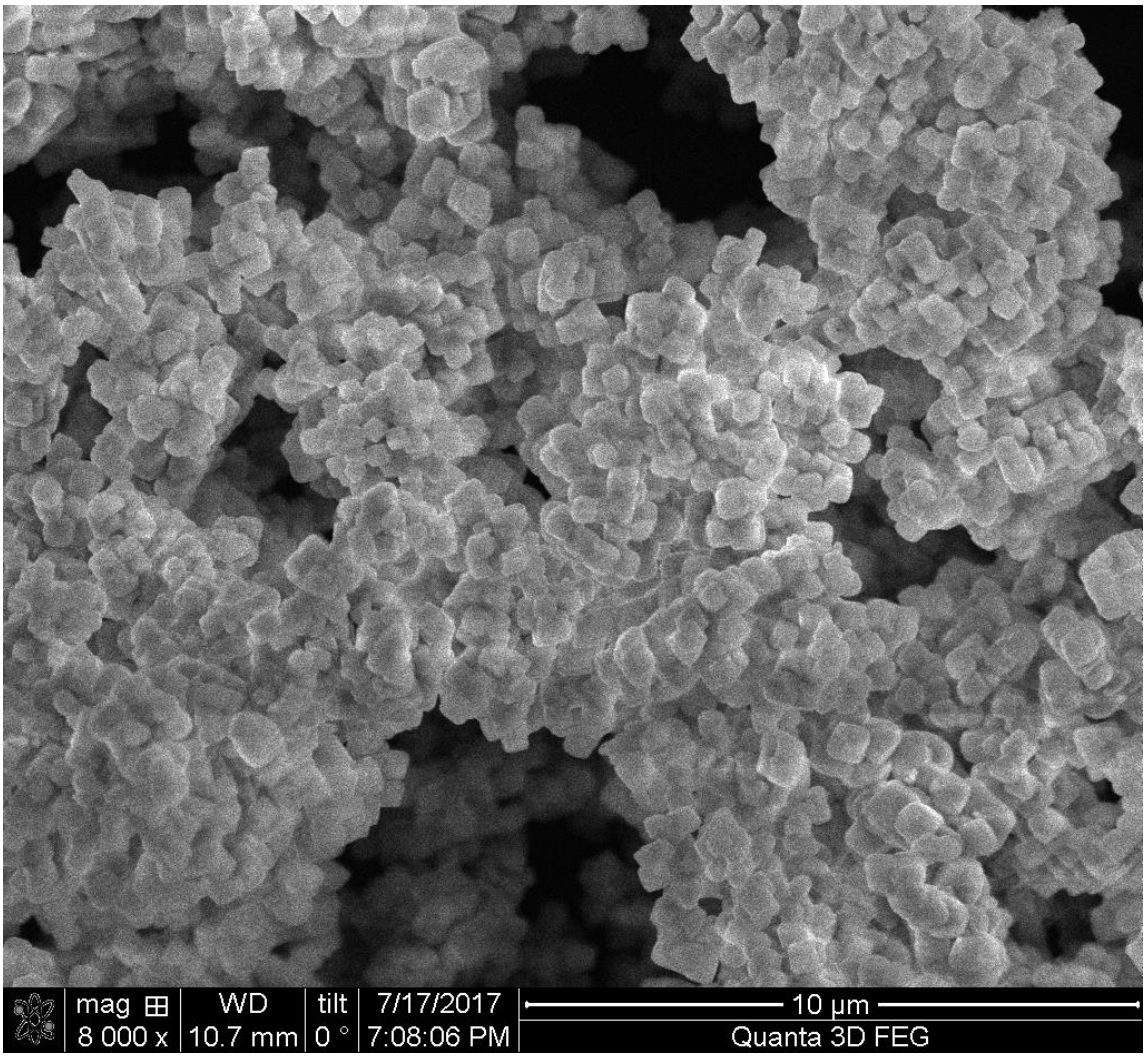

fig. S2. SEM image of activated MOF-801.

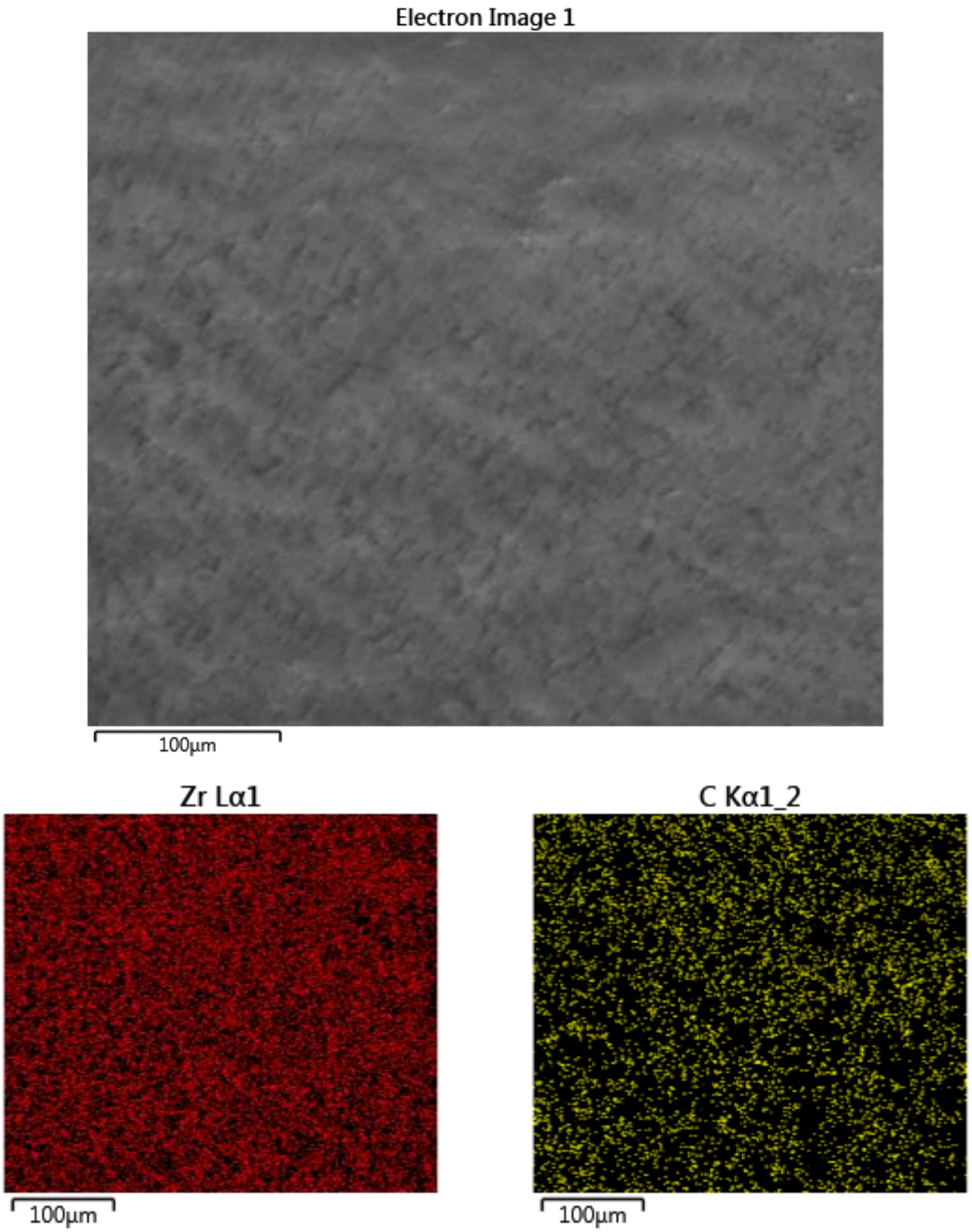

fig. S3. SEM and EDS images of MOF-801. SEM image of activated MOF-801 (top). Carbon and Zirconium EDS images of the MOF-801 (bottom).

Porosity and packing density analysis: A 35 mg sample was taken from 1100 g of well-mixed activated microcrystalline powder MOF-801 and transferred into a 9 mm bulb gas cell and charged with N_2 to avoid air contamination, then the cell was mounted on the instrument. 26 adsorption and 11 desorption points were collected.

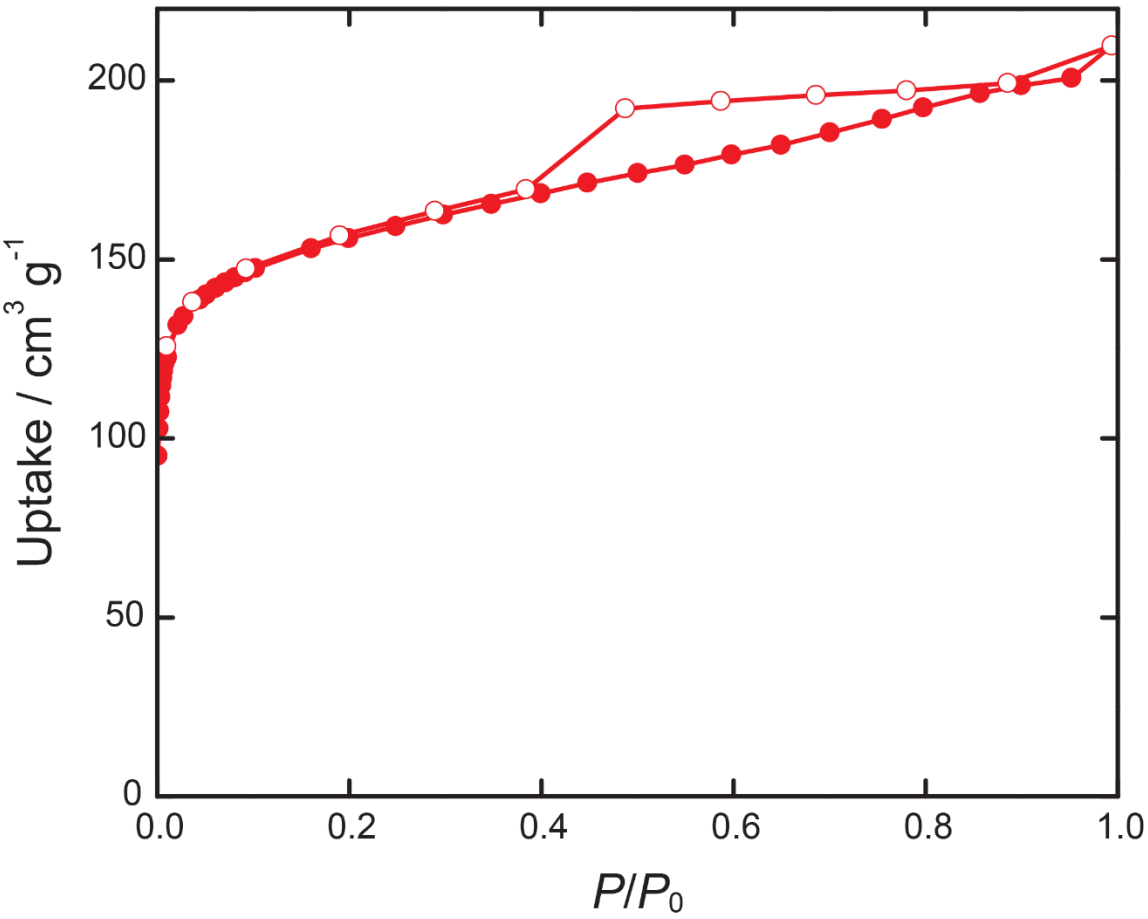

fig. S4. N_2 isotherm of activated MOF-801 recorded at 77 K. The BET surface area is 582 m^2 g^{-1}.

The powder particle density (ρ_p) of activated MOF-801 was estimated to be 1.401 g cm^{-3} from the pycnometer measurement (the framework density ρ_s = 2.3116 ± 0.0075 g cm^{-3}) and BET pore volume measurements (V_p = 0.2810 cm^3 g^{-1}) (see equation (1))

$$\rho_p = \frac{1}{\left(V_P + \frac{1}{\rho_s}\right)} \quad (1)$$

section S2.4. Evaluation of water capacity properties

A 34 mg sample was taken from an activated pre-scaled-up batch of MOF-801 and transferred to a 9 mm bulb gas cell and charged with N_2 to avoid air contamination, then the cell was mounted on the instrument. The temperature of the adsorbent was controlled using a water bath.

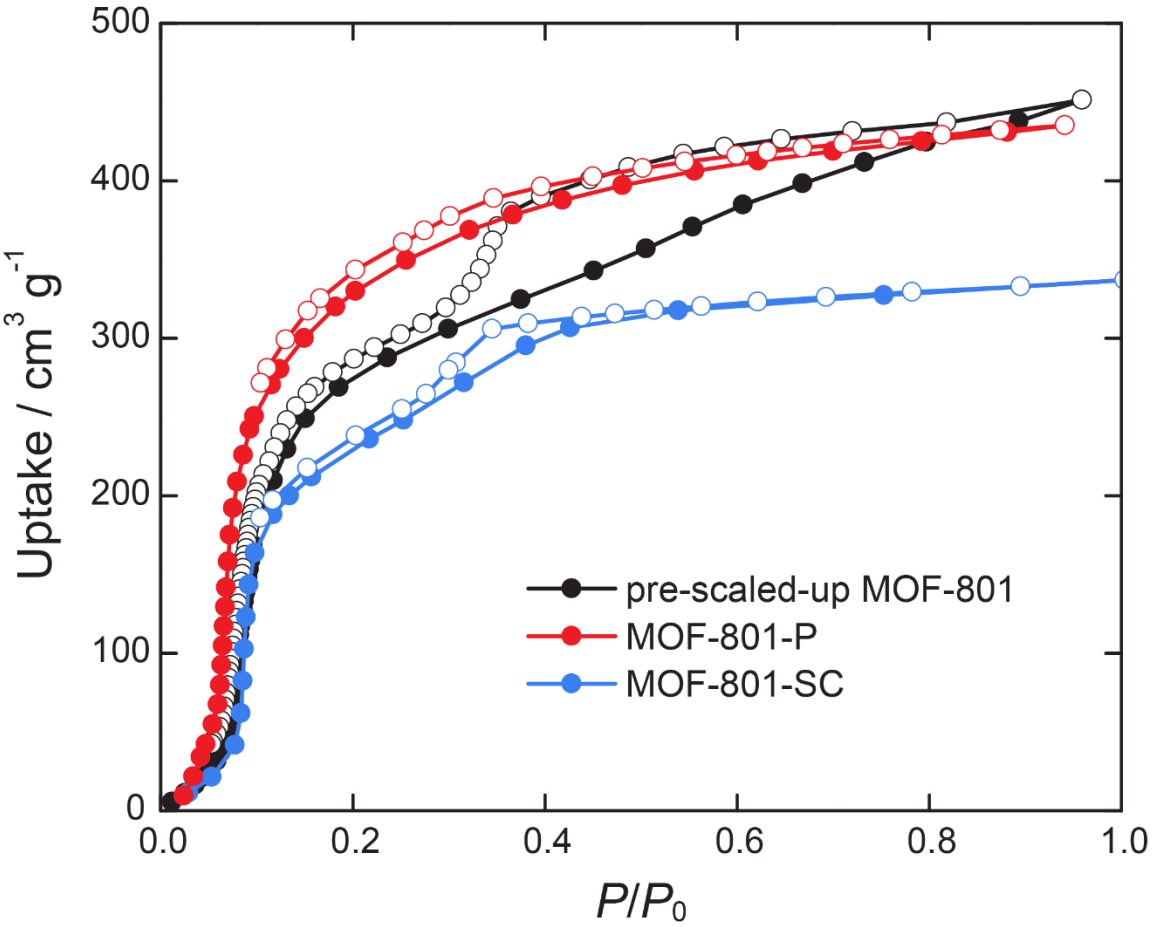

fig. S5. Water sorption isotherms of pre–scaled-up MOF-801 sample (black, this work), MOF-801-P (red), and MOF-801-SC (blue) (*7*).

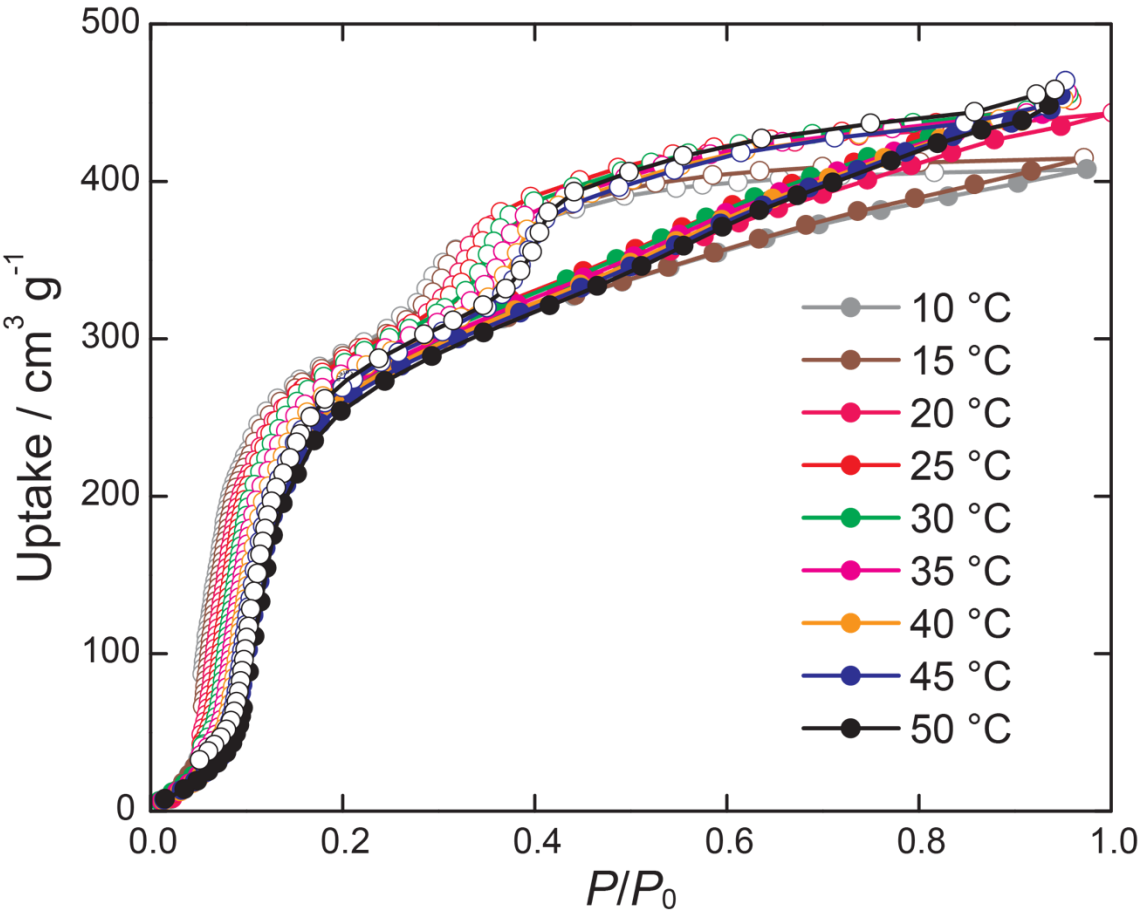

fig. S6. Water sorption isotherms of pre–scaled-up MOF-801 recorded at different temperatures.

Characteristic curves and isosteric heat of adsorption of activated MOF-801: The characteristic *A*-*W* water sorption curves were estimated using the Polanyi adsorption potential theory (equations (2,3))

$$A = RT \ln \frac{p_0(T)}{p} \tag{2}$$

$$W = \frac{q(p,T)}{\rho_{liq}^{wf}(T)} \tag{3}$$

where A is the molar Gibbs free energy of adsorption, p_0 is the temperature-dependent vapor pressure of water, W is the volume liquid adsorbed, q is the mass adsorbed, and ρ_{liq}^{wf} is the liquid density of water (*24*).

The isosteric heat of adsorption was estimated using the Clausius-Clapeyron relation.

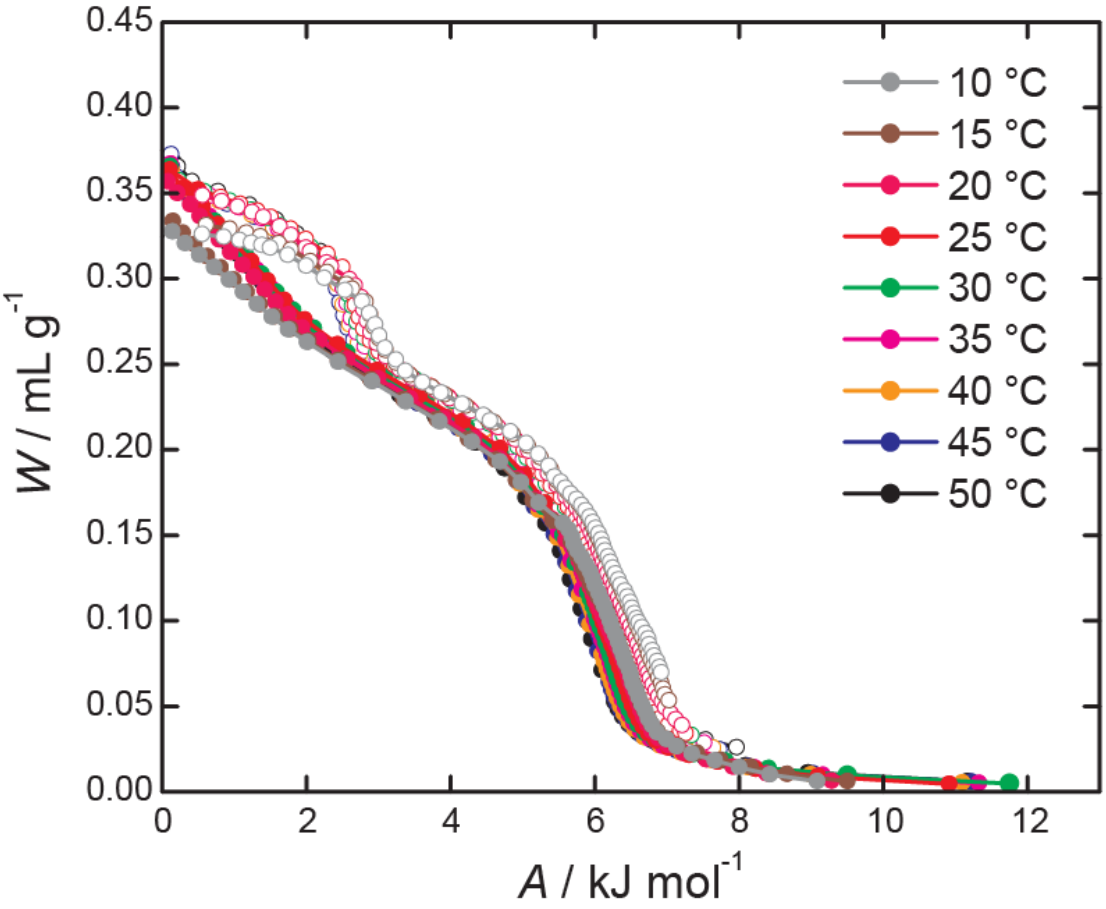

fig. S7. Characteristic curves for activated pre–scaled-up MOF-801 determined using Eqs. 2 and 3 based on the sorption isotherms measured at different temperatures.

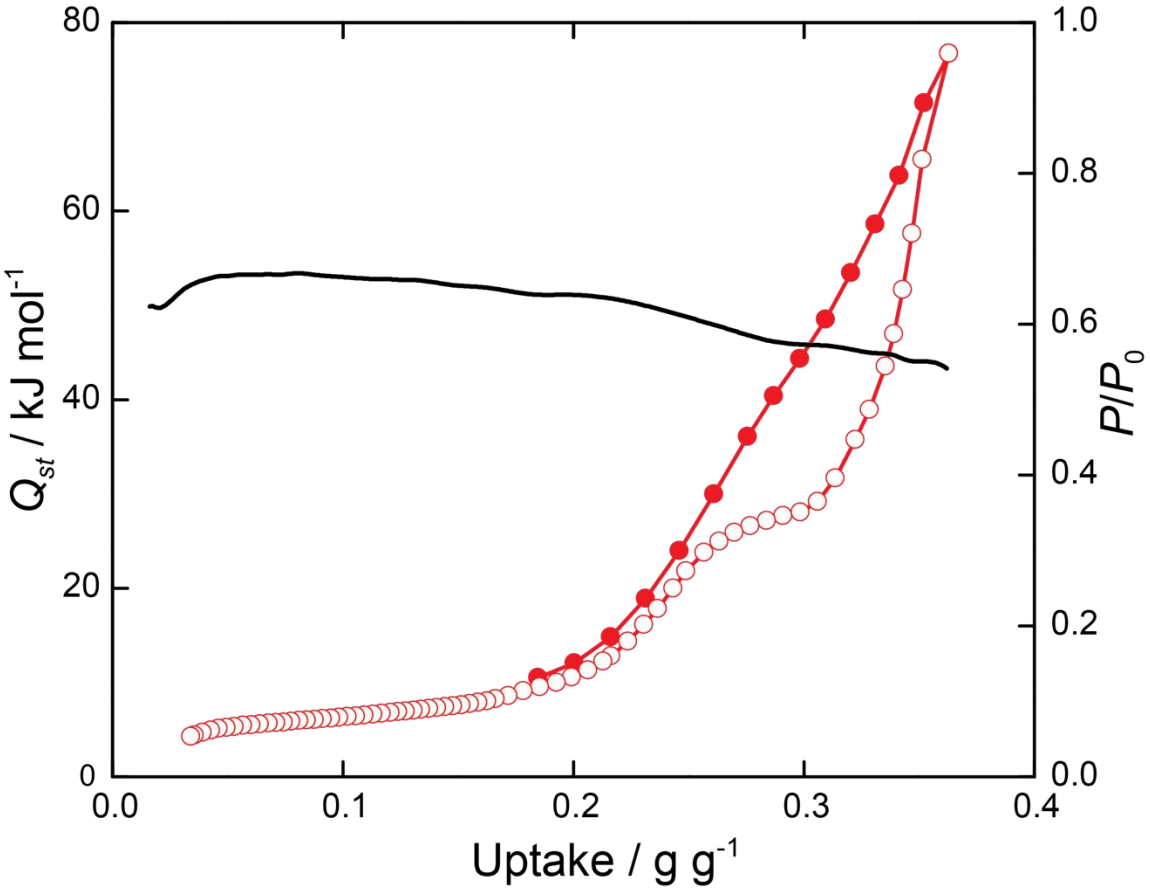

fig. S8. Isosteric heat of adsorption (black) and water sorption isotherm at 25°C (red) for activated MOF-801.

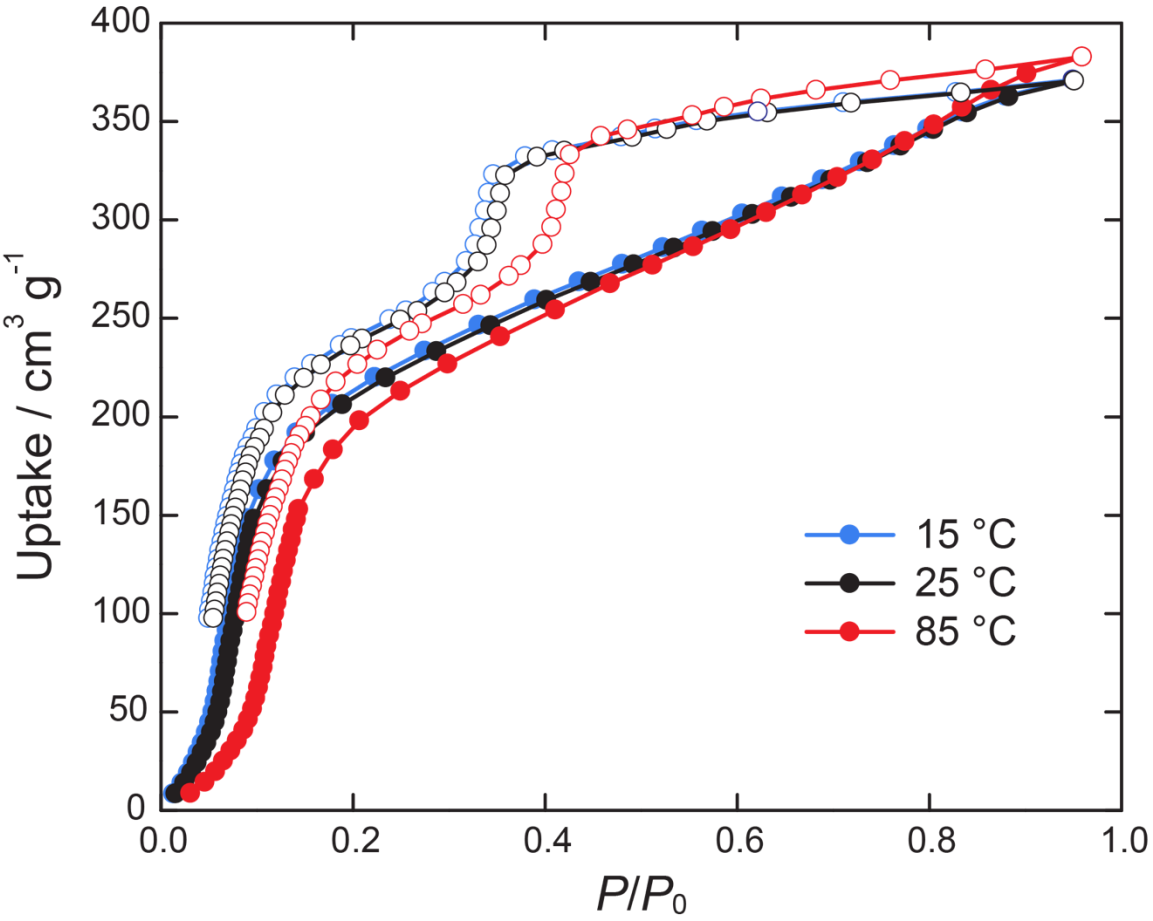

fig. S9. Experimental water sorption isotherm for activated scaled-up MOF-801 recorded at 25°C and calculated water sorption isotherms at 15 and 85°C. A 35 mg sample was taken from activated scaled-up MOF-801, transferred to a 9 mm bulb gas cell, and charged with N_2 to avoid air contamination. Then the cell was mounted on the instrument.

section S3. MOF-801/G preparation and characterization

section S3.1. Preparation of the mixture

1100 g of activated scaled-up microcrystalline MOF-801powder was mixed with 550 g of graphite powder in the 2 L jar to produce 1650 g of 67:33 wt% MOF-801-graphite mixture, termed MOF-801/G. The resulting mixture was thoroughly mixed by shaking the jar until the MOF/G powder had a homogenous gray color. Aggregation of MOF-801 powder into large particles was observed, these aggregates were crushed using a spatula and remixed. The resulting mixture was further characterized in terms of crystallinity, powder density, porosity and water uptake properties without any additional activation.

section S3.2. Characterization of MOF-801/G

PXRD of graphite, and PXRD, EDS analysis, and SEM images of activated MOF-801/G: Commercially available graphite powder was used for PXRD experiment without any modifications. A powder sample was placed on a zero-background sample holder and mounted on the diffractometer. The data was collected from 3 to 50 degrees with a step width of 0.01 and a total data collection time of 30 minutes. SEM and EDS images were taken to study the morphology and elemental composition of bulk MOF-801/G powder.

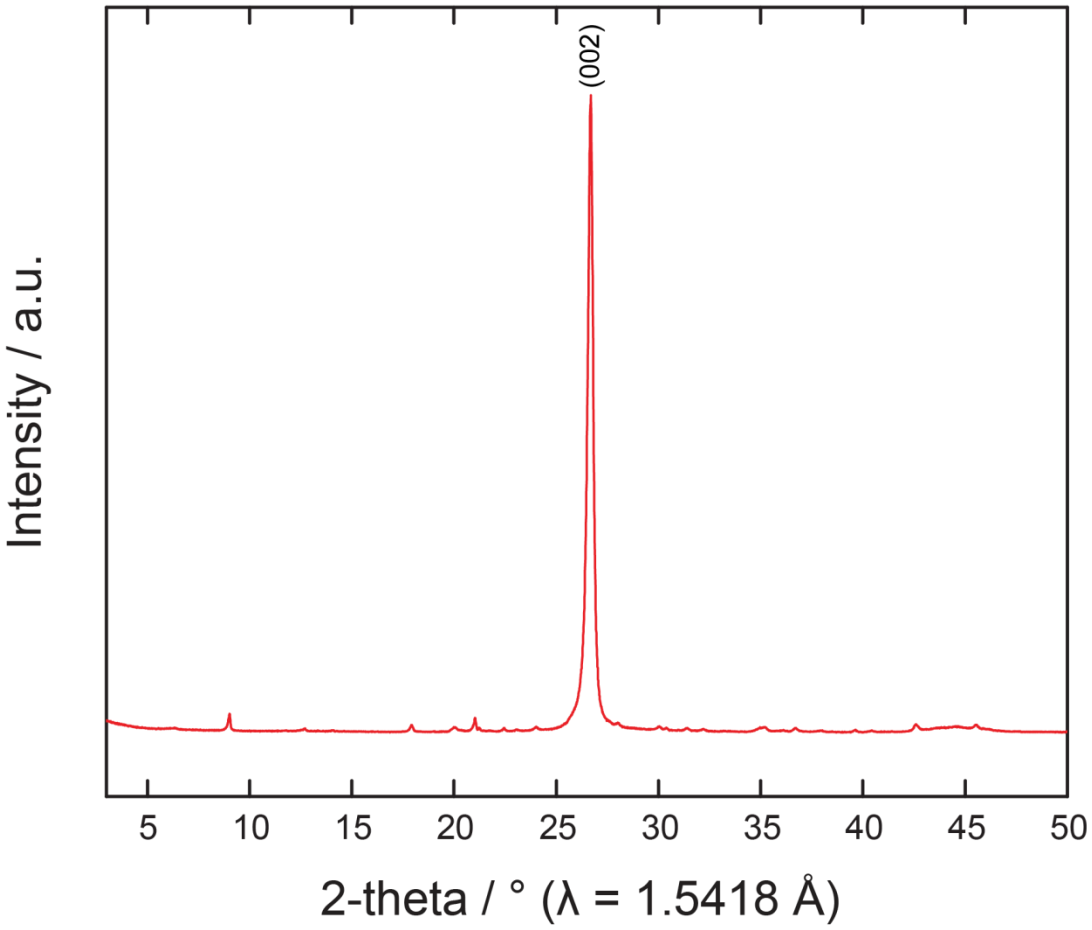

fig. S10. PXRD pattern of the graphite sample.

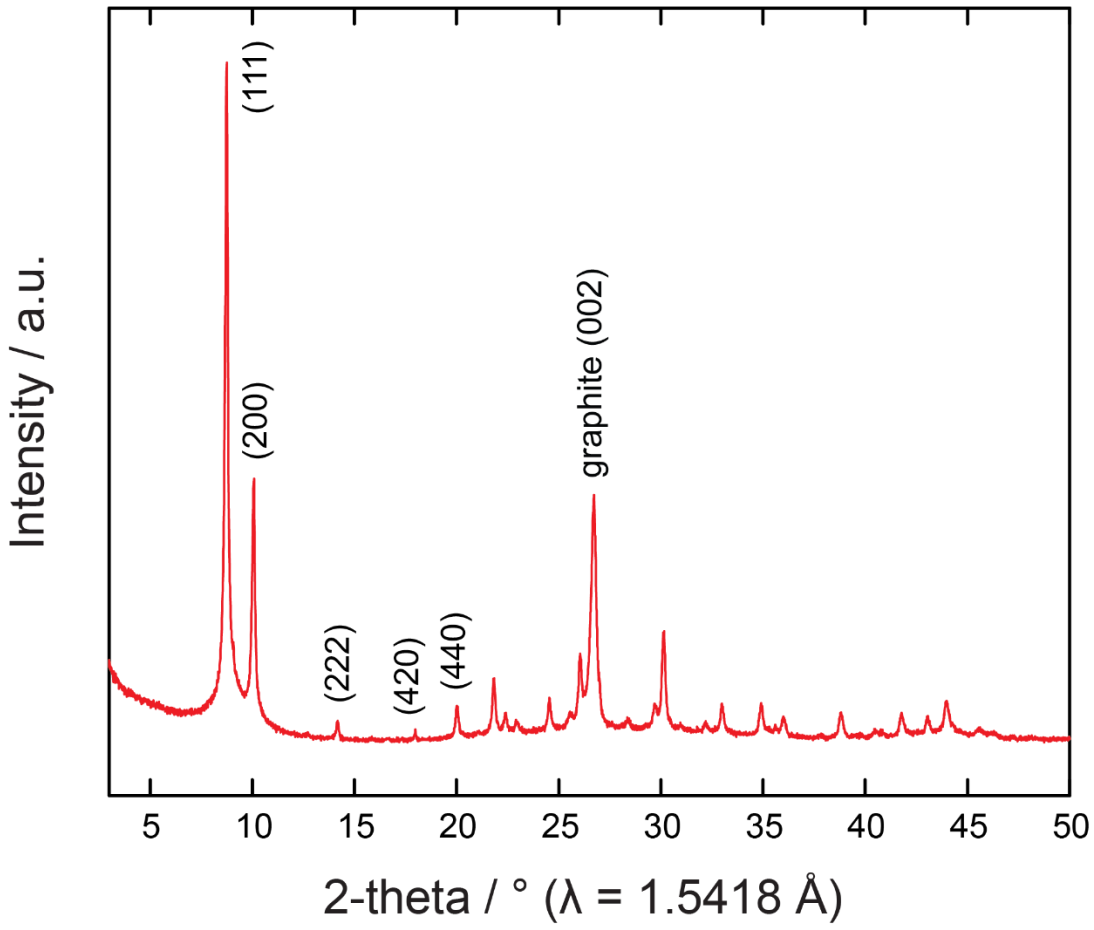

fig. S11. PXRD pattern of activated sample of MOF-801/G. A ground sample was placed on a zero-background sample holder and mounted on the diffractometer. The data was collected from 3-50 degrees with a step width of 0.01and a total data collection time of 30 minutes. The peak at 26.5º corresponds to the (002) reflection of graphite.

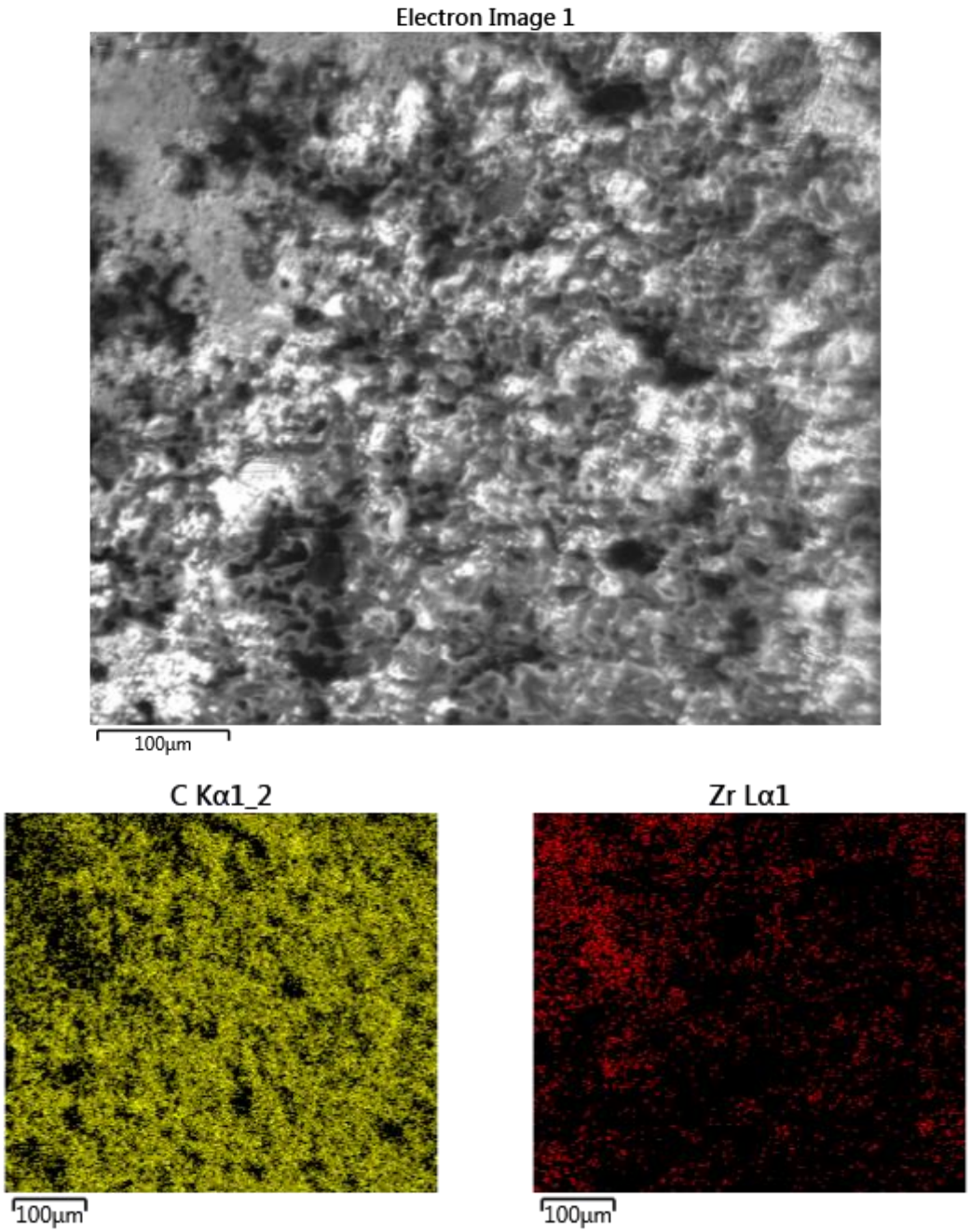

fig. S12. SEM and EDS images of MOF-801/G. SEM image of activated MOF-801/G (top). Carbon and Zirconium EDS images of the MOF-801/G (bottom).

Porosity and packing density analysis: Due to the extremely low porosity of the graphite used in this work, the measurement of its N_2 isotherm at 77 K was complicated by large instrumental errors. Therefore, N_2 isotherms of pure graphite are not shown.

78 mg of well-mixed activated MOF-801/G were transferred to a 9 mm bulb gas cell and charged with N_2 to avoid air contamination, then the cell was mounted on the instrument. 26 adsorption and 11 desorption points were collected.

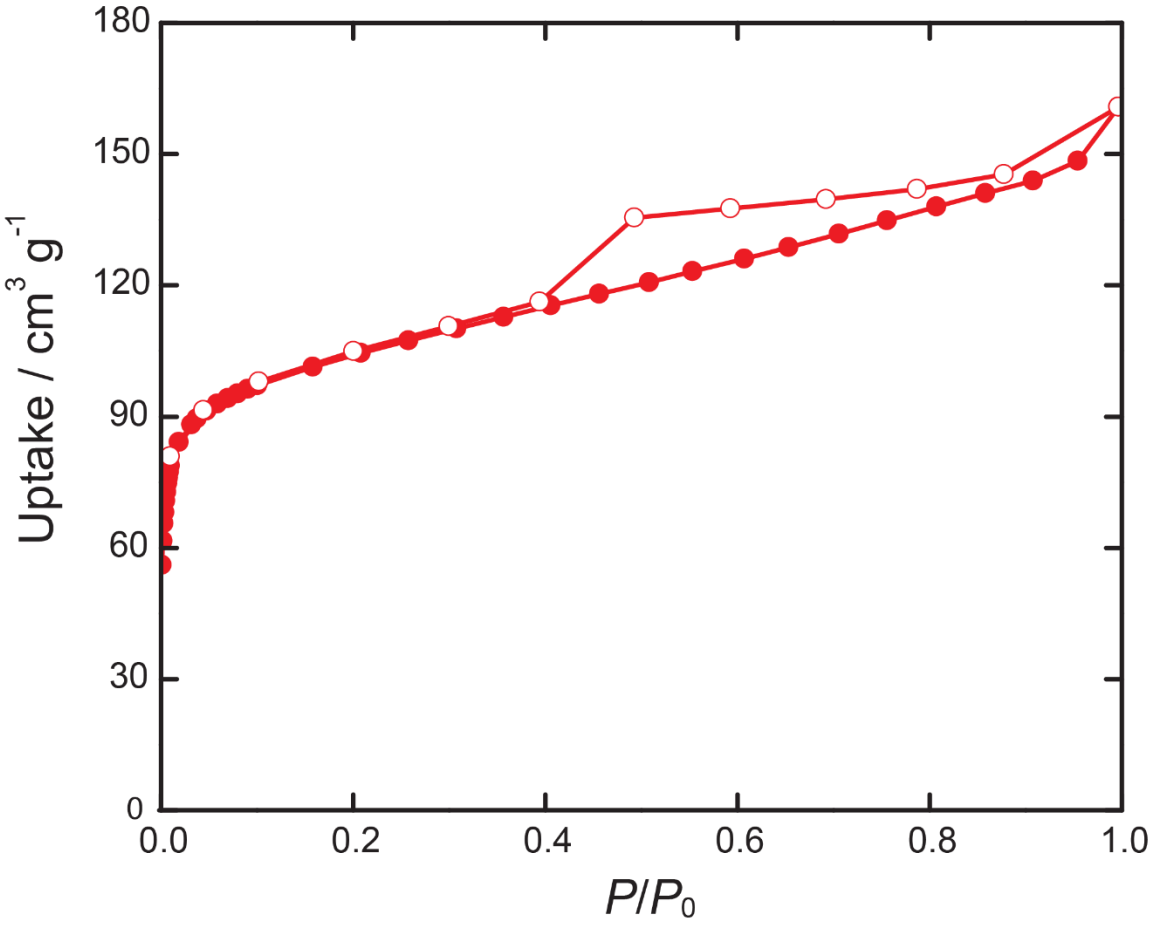

fig. S13. N_2 isotherm of the activated MOF-801/G recorded at 77 K. The BET surface area is 383 m^2 g^{-1}.

The expected BET surface area for the MOF-801/G was determined by multiplying the surface area of pure MOF-801 with the ratio of MOF within the mixture:
582 mg^{-1} × 67 wt% = 389 m^2 g^{-1}

The powder particle density (ρ_p) of activated MOF-801/G was estimated to be 1.552 g cm^{-3} from the pycnometer measurement (framework density ρ_s = 2.2822 ± 0.0105 g cm^{-3}) and BET pore volume measurements (V_p = 0.2060 cm^3 g^{-1}) (see equation (1)). The expected powder particle density was calculated as follows

$$\rho_{MOF-801/G} = \frac{m_{MOF-801/G}}{\frac{m_{MOF-801}}{\rho_{MOF-801}} + \frac{m_{graphite}}{\rho_{graphite}}} = \frac{1650\,\text{g}}{\frac{1100\,\text{g}}{1.401\,\text{g cm}^{-3}} + \frac{550\,\text{g}}{2.16\,\text{g cm}^{-3}}} = 1.587\,\text{g cm}^{-3}$$

section S3.3. Evaluation of water sorption properties
A 78 mg sample of activated MOF-801/G was transferred to a 9 mm bulb gas cell and charged with N_2 to avoid air contamination. Subsequently the cell was mounted on the instrument.

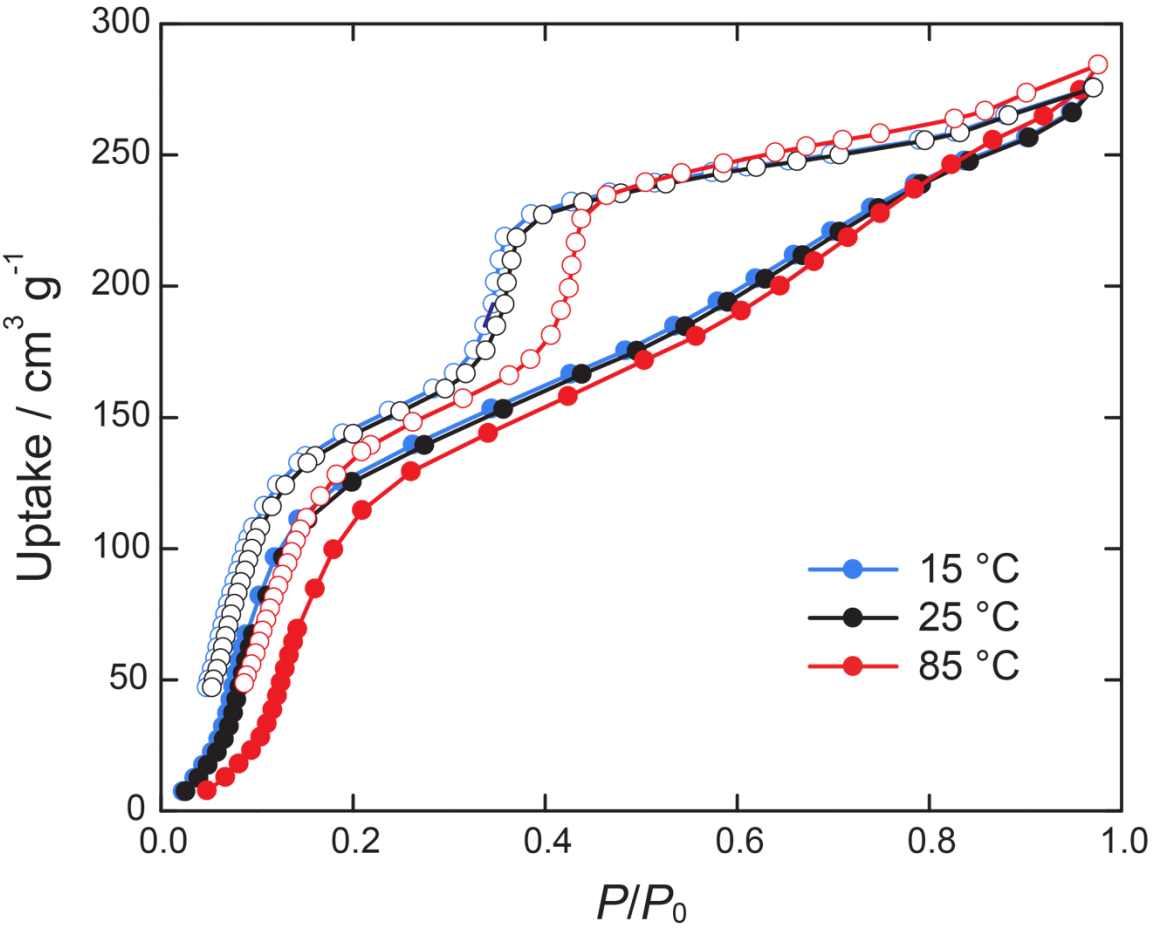

fig. S14. Experimental water sorption isotherm for MOF-801/G at 25°C and calculated water sorption isotherms at 15° and 85°C.

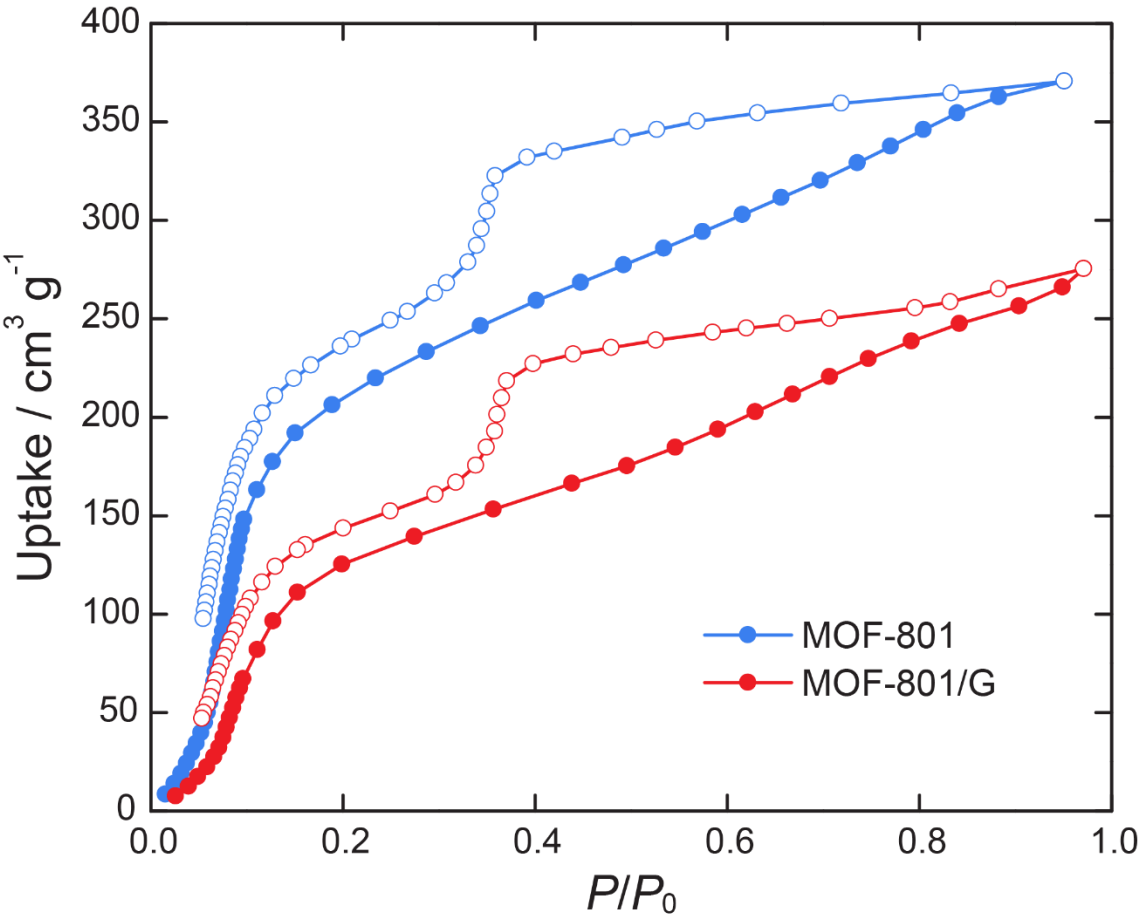

fig. S15. Comparison of water sorption isotherms for scaled-up MOF-801 and MOF-801/G at 25°C. As expected, the water uptake drops by ~ 33 wt% after mixing with non-porous graphite, however, the general shape of the isotherm remains the same.

section S4. MOF-303 synthesis and characterization

section S4.1. Synthesis of microcrystalline MOF-303 powder

MOF-303, Al(OH)(HPDC)(H_2O): 10.4 g Aluminum chloride hexahydrate ($AlCl_3 \cdot 6H_2O$, 43.08 mmol) and 7.5 g 3,5-pyrazoledicarboxylic acid monohydrate (H_3PDC, 43.08 mmol) were dissolved in 720 mL water in a 1 L glass jar, 30 mL aqueous NaOH (2.6 g, 65 mmol) were added dropwise to the above mixture under stirring. The jar was then sealed and heated in a 100 ºC isothermal oven for 24 h. (Yield: 3.0 g, 35% based on the linker). Single crystals suitable for X-ray diffraction study were prepared by combining 0.6 mmol $AlCl_3 \cdot 6H_2O$, 0.6 mmol H_3PDC, and 0.7 mmol NaOH in 4 mL H_2O. The resulting mixture was sealed in a 23 mL autoclave and placed in a 100 ºC isothermal oven for 7 days, EA: Calcd. for $Al(OH)(C_5H_2O_4N_2)(H_2O)$: C, 27.79; H, 2.33; N, 12.96%. Found: C, 27.62; H, 2.26; N, 12.74%. ATR-FTIR (4000-400 cm^{-1}): 1667(w), 1601(s), 1525(m), 1482(w), 1440(m), 1386(s), 1193(m), 1106(m), 998(s), 848(w), 791(s), 588(br), 456(s), 422(w).

section S4.2. MOF-303 activation

The white crystalline as-synthesized MOF-303 powder was collected by filtration and washed three times daily with water for three days, then with methanol three times daily for three days, and was then filtered and dried in air. The air-dried MOF sample was evacuated at room temperature until the pressure dropped below 1 kPa. After that, the sample was heated in vacuum at 100 ºC for 24 hours, and then at 150 ºC for another 48 hours. The combined MOF powder from 150 jars was then placed on an aluminum pan and transferred into a drying oven and heated at 160 ºC for 10 days prior to the characterization. Overall, 450 g of activated microcrystalline MOF-303 powder were prepared.

section S4.3. Characterization of single crystal and microcrystalline powder MOF-303

Single crystal X-ray diffraction analysis: Single crystal X-ray diffraction data were collected for a colorless plate-shaped (20 μm × 20 μm × 10 μm) crystal of as-synthesized MOF at beamline 11.3.1 of the ALS at LBNL, equipped with a Bruker Photon 100 CMOS area detector using synchrotron radiation (10-17 KeV), at 0.7749 Å. The crystal was mounted on a MiTeGen® kapton loop and placed under a 100 (2) K nitrogen cold stream. Data were processed using the Bruker APEX2 software package (*25*), integrated using SAINT v8.34A and corrected for the absorption by SADABS routines (no correction was made for extinction or decay). The structures were solved by intrinsic phasing (SHELXT) and refined by full-matrix least squares on F^2 (SHELXL) (*26*). Atomic positions of MOF-303 were obtained from the single crystal data, but the anisotropic refinement remains unstable due to the poor diffraction of the crystals. Based on the structural model obtained from single-crystal data, the Pawley structural

refinement was performed using the *Reflex* module in BIOVIA Materials Studio 7.0 (*27*). Selected crystal data and atomic position are given in table S1, S2.

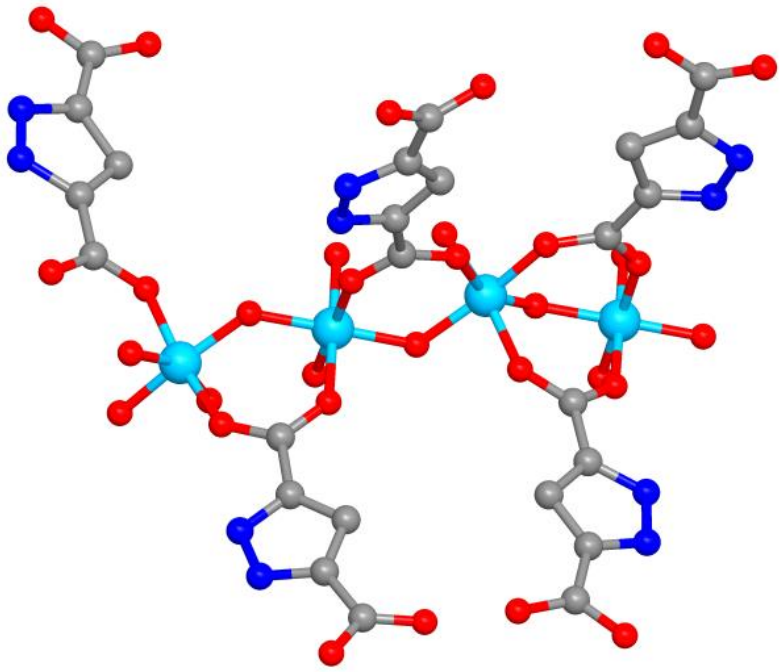

fig. S16. Asymmetric unit in the single-crystal structure of MOF-303 (atoms are shown isotropically). Hydrogen atoms are omitted for clarity. Color code: C, gray; N, blue; O, red; Al, cyan.

table S1. Crystal data and structure determination for MOF-303 with single crystal data set.

Compound	MOF-303
Chemical formula	$C_{20}H_{12}O_{20}N_8Al_4$
Formula mass	792.30
Crystal system	monoclinic
Space group	$P2_1$
λ (Å)	0.7749(1)
a (Å)	12.2714(16)
b (Å)	14.572(2)
c (Å)	14.253(2)
β (°)	101.787(10)
Z	4
V (Å^3)	2495.0(6)
Temperature (K)	100(2)
Size (mm^3)	0.01 × 0.02 × 0.02
Density (g cm^{-3})	1.159
Measured reflections	16277
Unique reflections	3425
Parameters	209
Restraints	1
R_{int}	0.172
θ range (°)	2.2-19.7
R_1, wR_2	0.2948 0.6525
S (GOF)	2.86
Max/min res. dens. (e Å^{-3})	2.32/-1.38

table S2. Atomic positions for MOF-303 from the Pawley refinement model. Space group $P2_1$. a = 12.2943 Å; b = 14.9784 Å; c = 14.6004 Å, β = 104.8238°

Atom name	Atom	*x* (Å)	*y* (Å)	*z* (Å)
Al1	Al	-2.5E-4	0.41685	0.73197
Al2	Al	0.5052	0.41616	0.7551
Al3	Al	0.26447	0.46312	0.79057
O4	O	0.14515	0.39394	0.75591
Al5	Al	0.74609	0.36962	0.71973
O6	O	0.65215	0.40091	0.78631
N7	N	0.65911	0.58781	0.4947
C8	C	0.0777	0.72771	0.46665
O9	O	0.02071	0.48883	0.83088
O10	O	0.35992	0.54594	0.8577
O11	O	0.51428	0.48687	0.65752
O12	O	0.65113	0.28639	0.65304
O13	O	0.20455	0.79397	0.38367
O14	O	0.99421	0.32564	0.85138
O15	O	0.52653	0.5122	0.82915
O16	O	0.68747	0.86186	1.12576
O17	O	0.80737	0.29639	0.8177
O18	O	0.20357	0.53672	0.69279
O19	O	0.20467	0.52545	0.87179
O20	O	0.68679	0.45674	0.63717
C21	C	0.58013	0.74842	1.02908
O22	O	0.51482	0.8318	1.14595
O23	O	0.35832	0.4318	0.72388
C24	C	0.48855	0.62779	0.50452
C25	C	0.10427	0.7884	0.39472
O26	O	0.01647	0.50848	0.65931
C27	C	0.14816	0.67003	0.53056
C28	C	0.52411	0.63714	0.92751
C29	C	0.07584	0.62466	0.57419
C30	C	0.59392	0.81827	1.10442
N31	N	0.62682	0.65447	0.43447
N32	N	0.62957	0.66206	0.92768
N33	N	-0.02885	0.71705	0.47343
O34	O	0.02097	0.8318	0.34361
C35	C	0.52304	0.68081	0.43799
C36	C	0.46556	0.56083	0.86836
C37	C	0.10124	0.55222	0.6462

C38	C	0.59316	0.50019	0.61568
O39	O	-0.14575	0.43922	0.70804
N40	N	-0.02924	0.65543	0.538
C41	C	0.10416	0.53187	0.8822
C42	C	0.90971	0.28167	0.86469
C43	C	0.8626	0.16279	0.97928
O44	O	0.48424	0.31984	0.68133
C45	C	0.93541	0.21017	0.93777
N46	N	0.66352	0.72837	0.98804
C47	C	0.4886	0.69163	0.99217
C48	C	0.57862	0.5694	0.53944
C49	C	0.54559	1.2441	0.64244
H50	H	0.68419	0.41194	0.84501
H51	H	0.32626	0.42087	0.66517
H52	H	0.16077	0.3388	0.74793
H53	H	0.73686	0.55587	0.50546
H54	H	0.41136	0.63246	0.52626
H55	H	0.23757	0.66099	0.54205
H56	H	0.67951	0.63378	0.88722
H57	H	-0.10175	0.63464	0.55666
H58	H	0.40953	0.6893	1.01121
C59	C	0.07726	0.59351	0.9532
N60	N	-0.02996	0.60721	0.95675
N61	N	-0.03044	0.66888	1.02125
H62	H	0.84905	0.49433	0.76191
H63	H	0.77244	0.16904	0.96483
H64	H	-0.10353	0.69193	1.0374

PXRD, EDS analysis, and SEM images: Activated microcrystalline MOF-303 was used for PXRD experiments. A ground sample was placed on a zero-background sample holder and mounted on the diffractometer. The data was collected from 3 to 50 degrees with a step width of 0.01 and a total data collection time of 30 minutes. SEM and EDS images were taken to study the morphology and elemental composition of bulk MOF-303 powder.

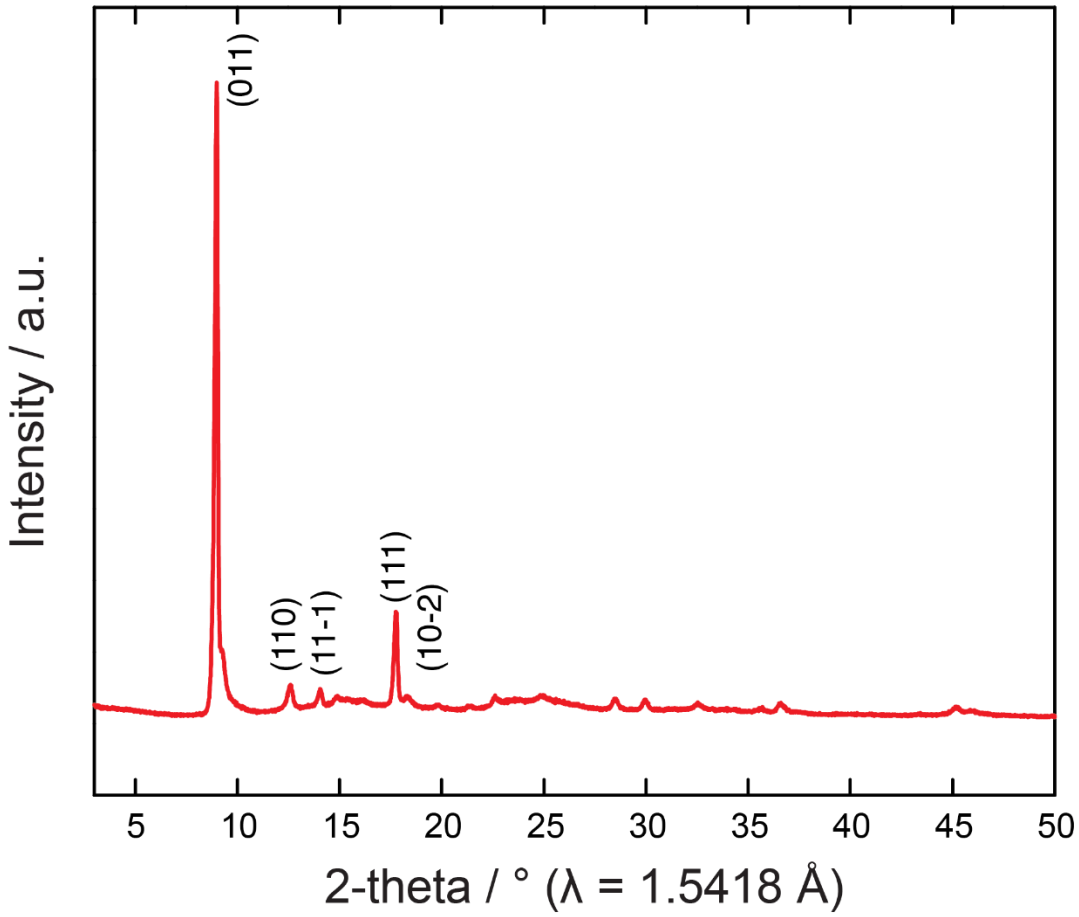

fig. S17. PXRD pattern of activated MOF-303.

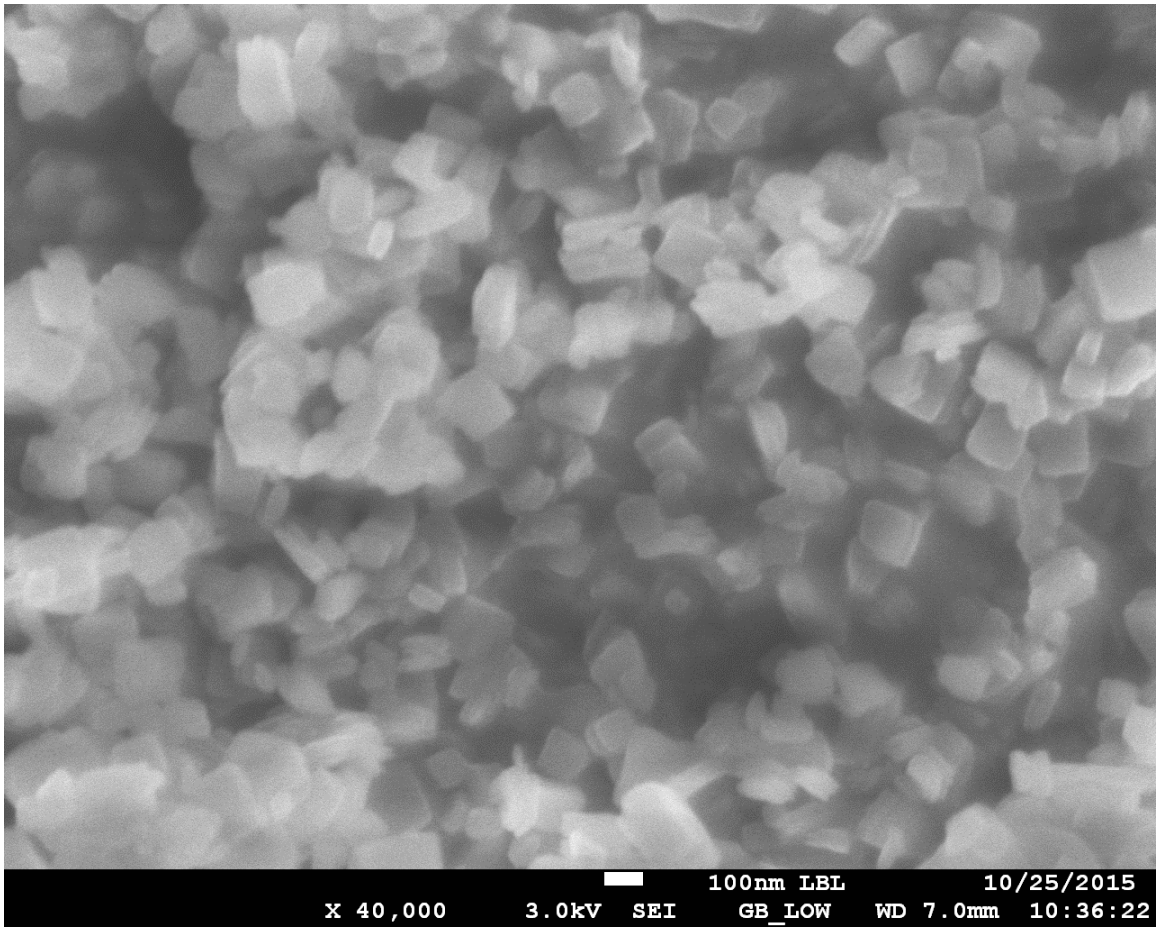

fig. S18. SEM image of activated MOF-303.

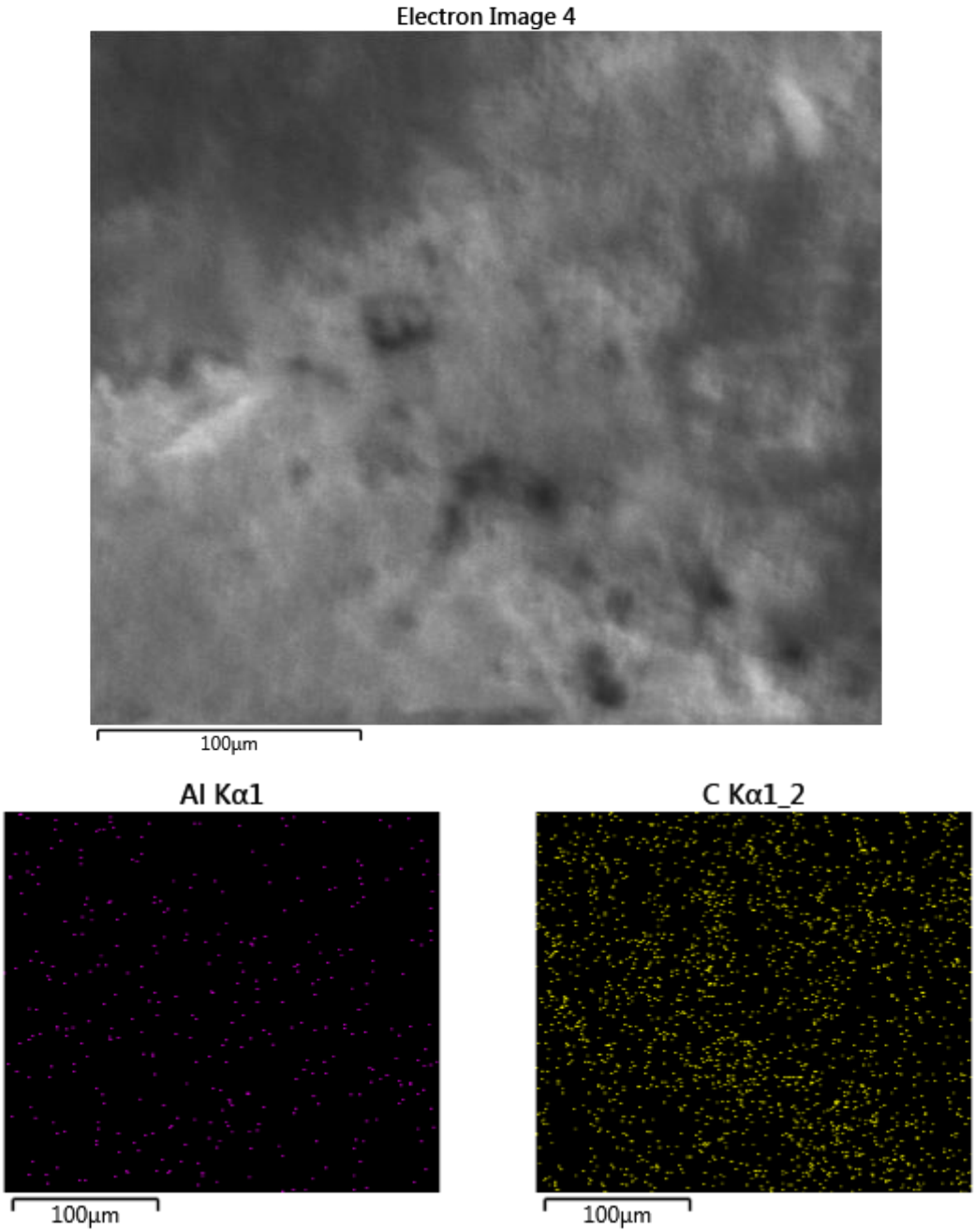

fig. S19. SEM and EDS images of MOF-303. SEM image of activated MOF-303 (top). Carbon and Aluminum EDS images of the activated MOF-303 (bottom).

Porosity and packing density analysis: A 45 mg sample was taken from 450 g of well-mixed activated MOF-303, transferred to a 9 mm bulb gas cell and charged with N_2 to avoid air contamination. Then, the cell was mounted on the instrument. 26 adsorption and 11 desorption points were collected.

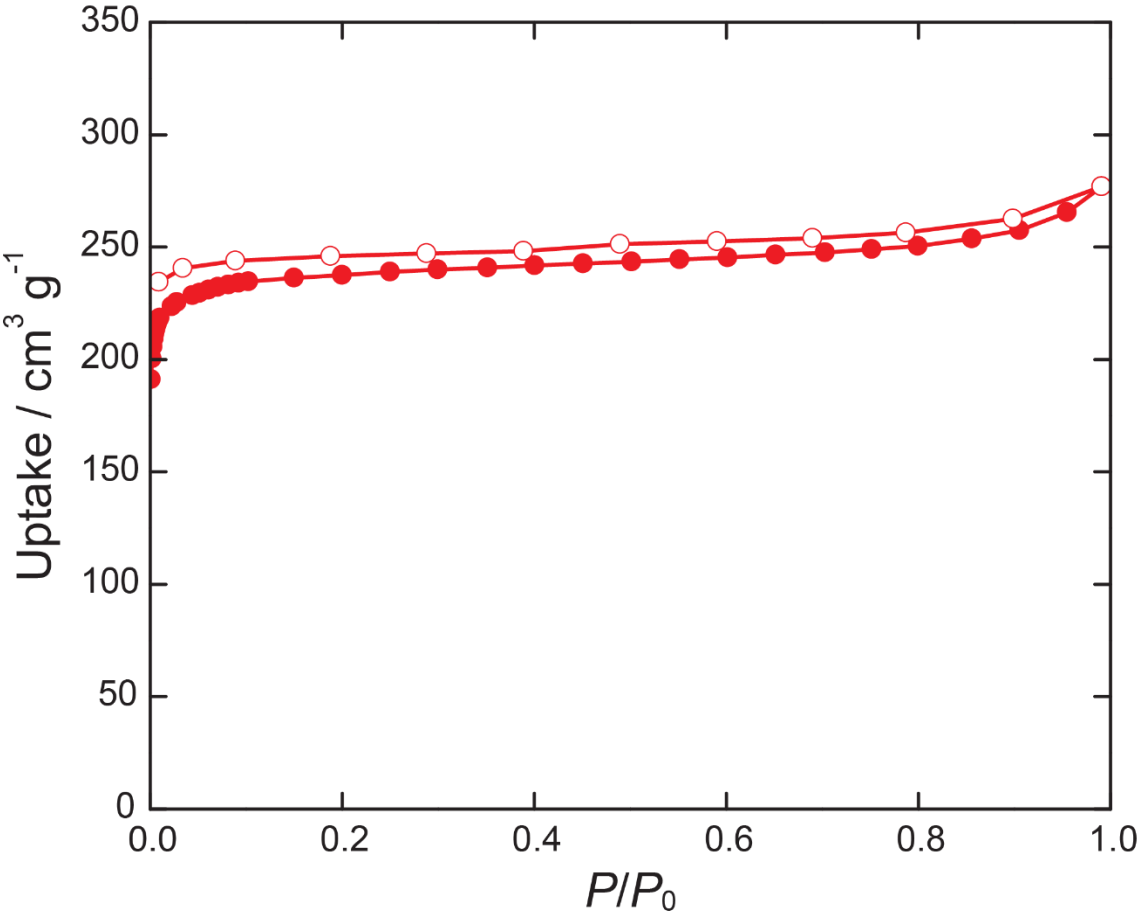

fig. S20. N_2 isotherm of activated scaled-up MOF-303 at 77 K. BET surface area is 989 $m^2 g^{-1}$.

The powder particle density (ρ_p) of activated scaled-up MOF-303 was estimated to be 1.293 g cm^{-3} from the pycnometer measurement (framework density ρ_s = 2.4591 ± 0.0037 g cm^{-3}) and BET pore volume measurements (V_p = 0.3670 cm^3 g^{-1}) (see equation (1)).

section S4.4. Evaluation of water capacity properties

A 38 mg sample was taken from the activated scaled-up MOF-303, transferred to a 9 mm bulb gas cell, and charged with N_2 to avoid air contamination. Then the cell was mounted on the instrument. The temperature of the adsorbent was controlled using a water bath. In case of pre-scaled-up MOF-303, 27 mg of sample was analyzed.

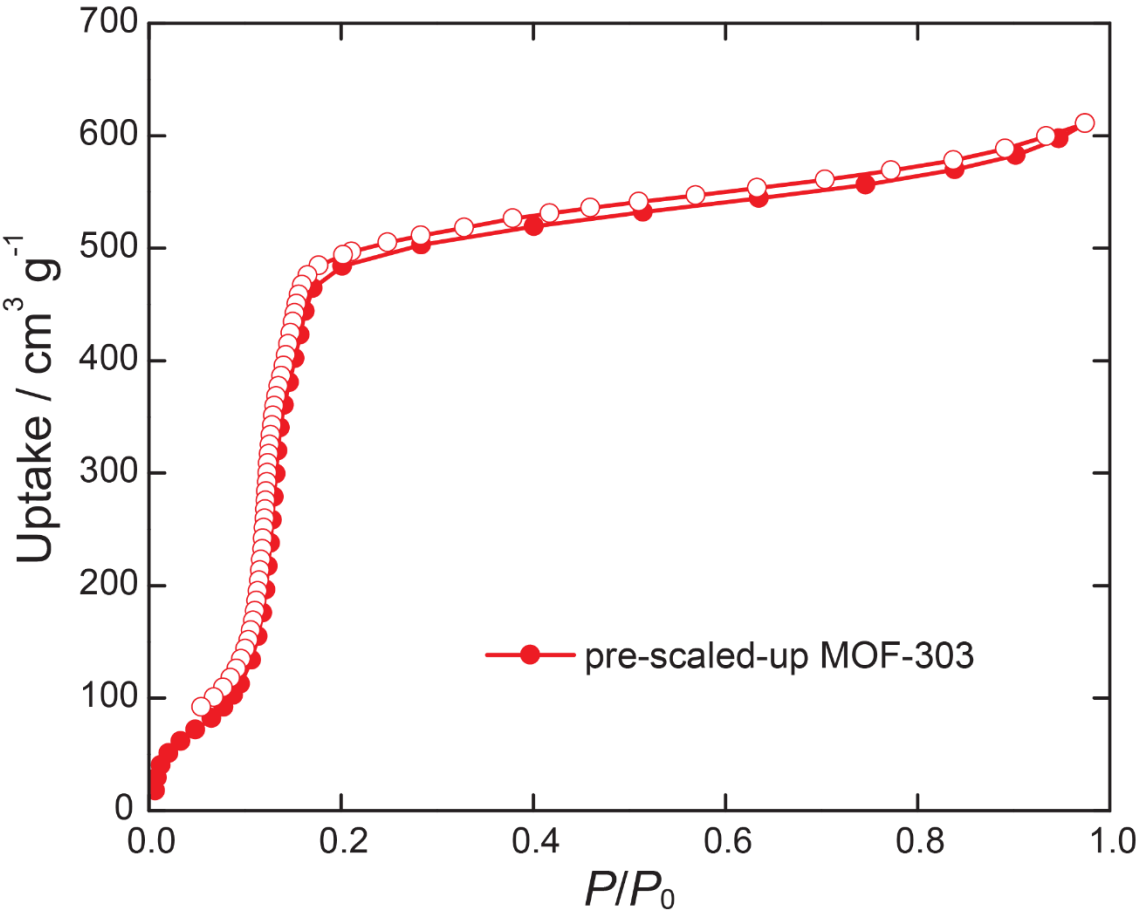

fig. S21. Water sorption isotherm of pre–scaled-up activated MOF-303 recorded at 25°C.

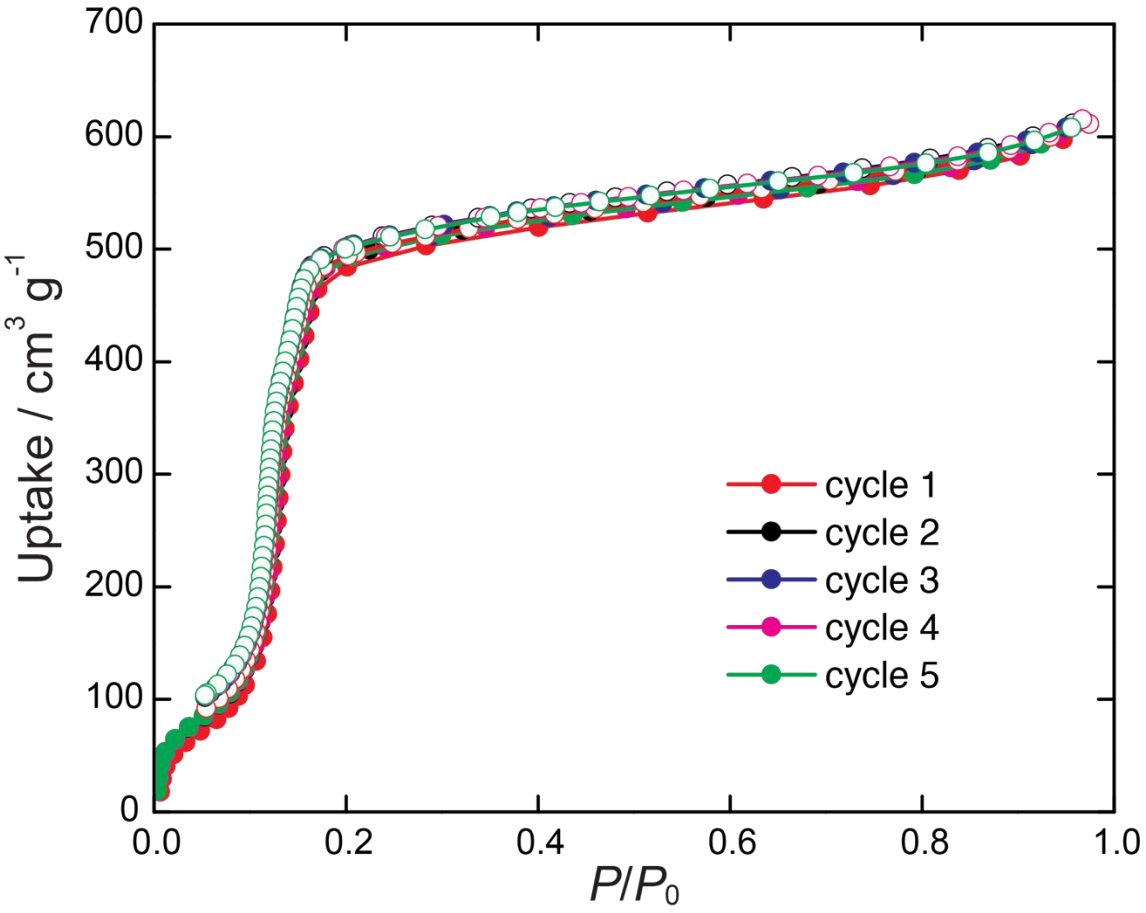

fig. S22. Cycling experiment of MOF-303. Five subsequent adsorption-desorption cycles recorded 25°C are shown.

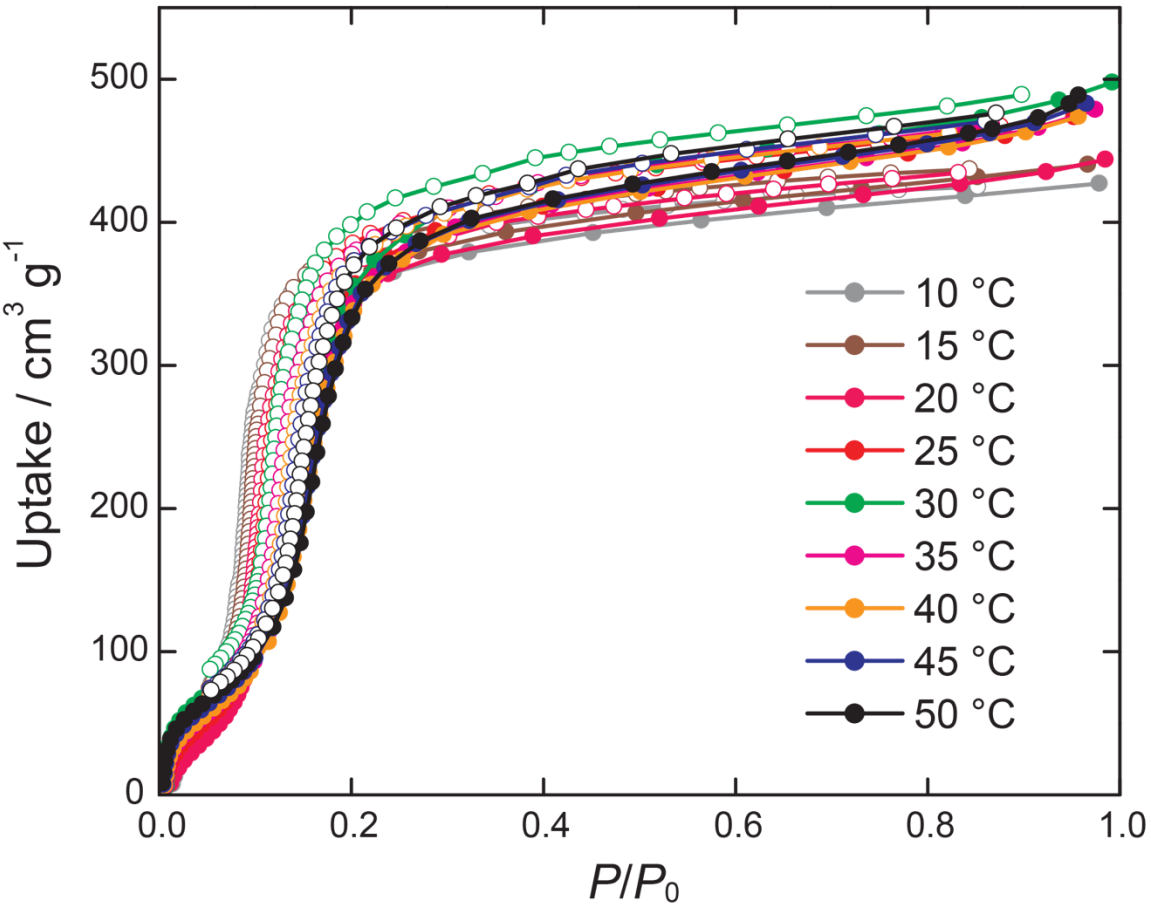

fig. S23. Water sorption isotherms of activated scaled-up MOF-303 at different temperatures.

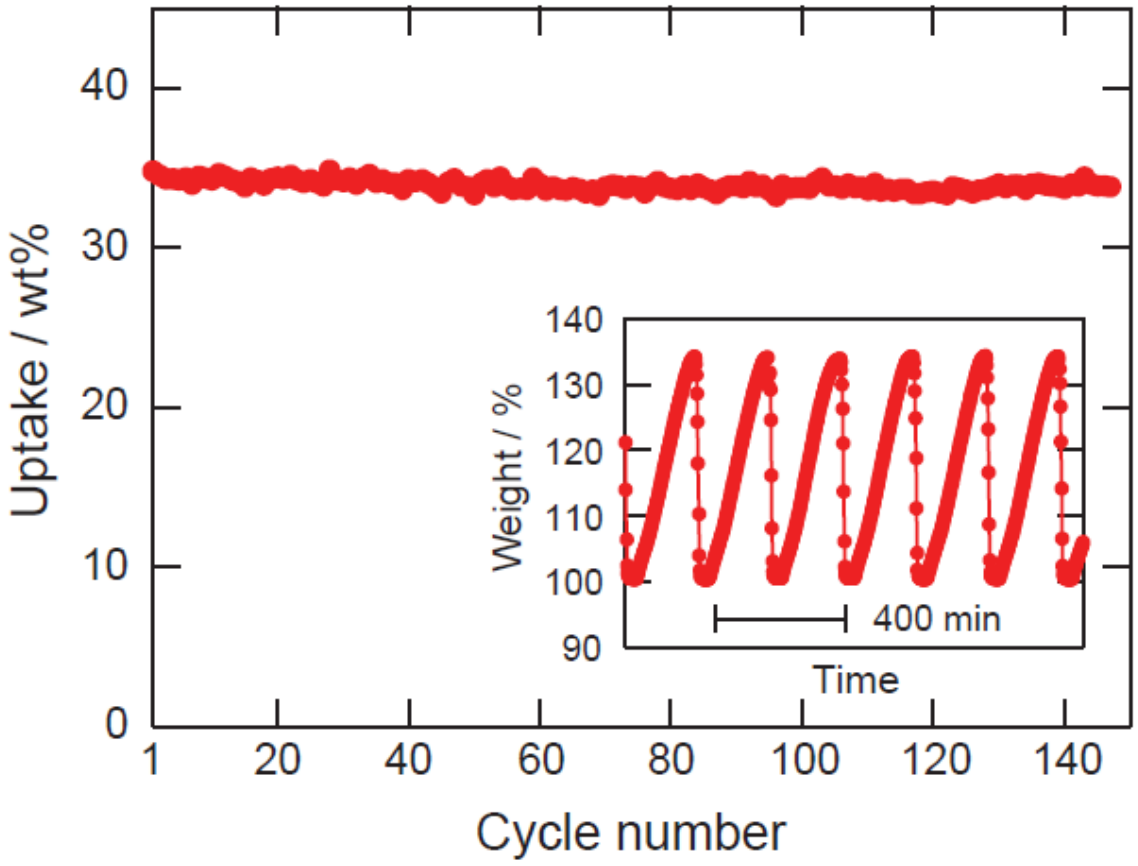

fig. S24. One hundred fifty cycles of RH swing cycling of scaled-up activated MOF-303 at 25°C in a TGA. The sample was purged a N_2 flow with 40% RH and then regenerated after saturation by purging with a dry N_2 flow at 85°C for 30 minutes before commencing the next cycle. Weight percentage was estimated as (mass of activated material + mass of adsorbed water) / (mass of activated material).

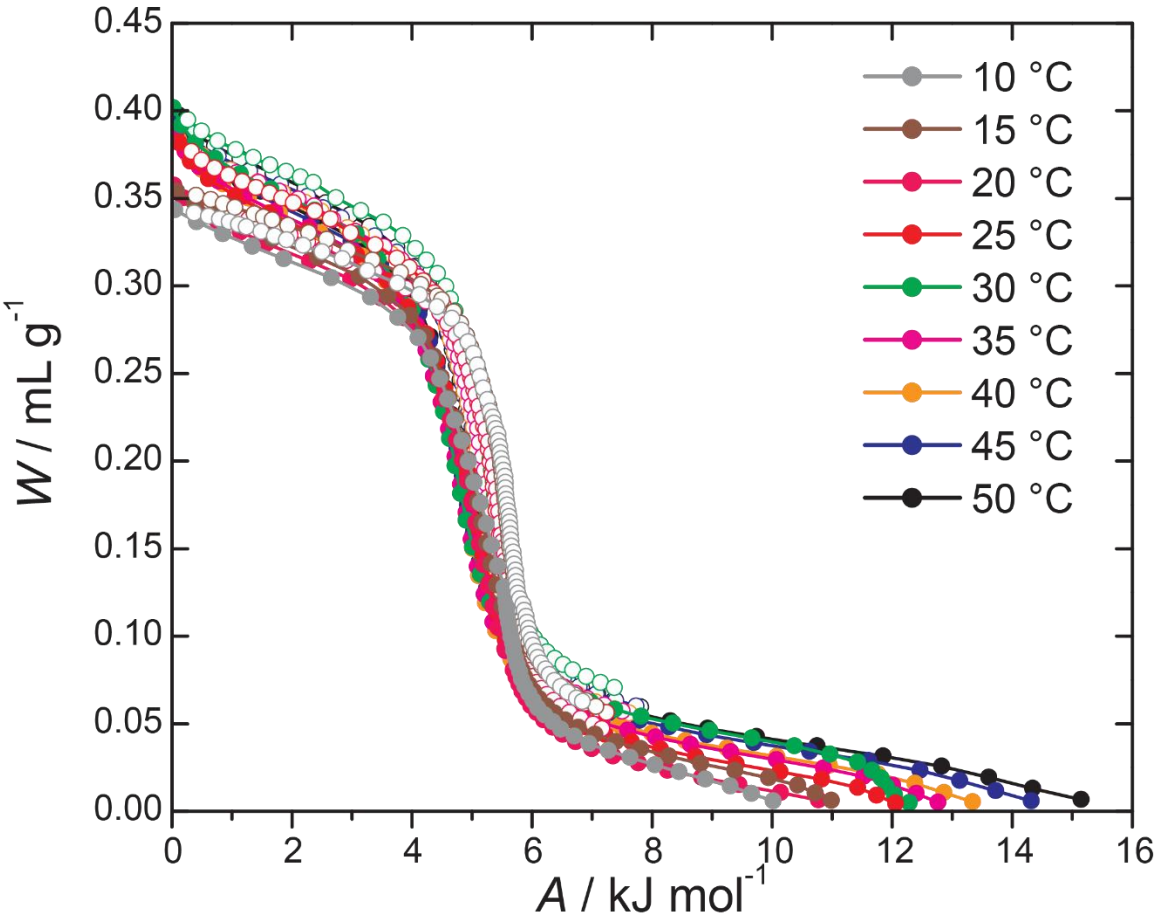

fig. S25. Characteristic curves determined using Eqs. 2 and 3 based on sorption isotherms for MOF-303 measured at different temperatures.

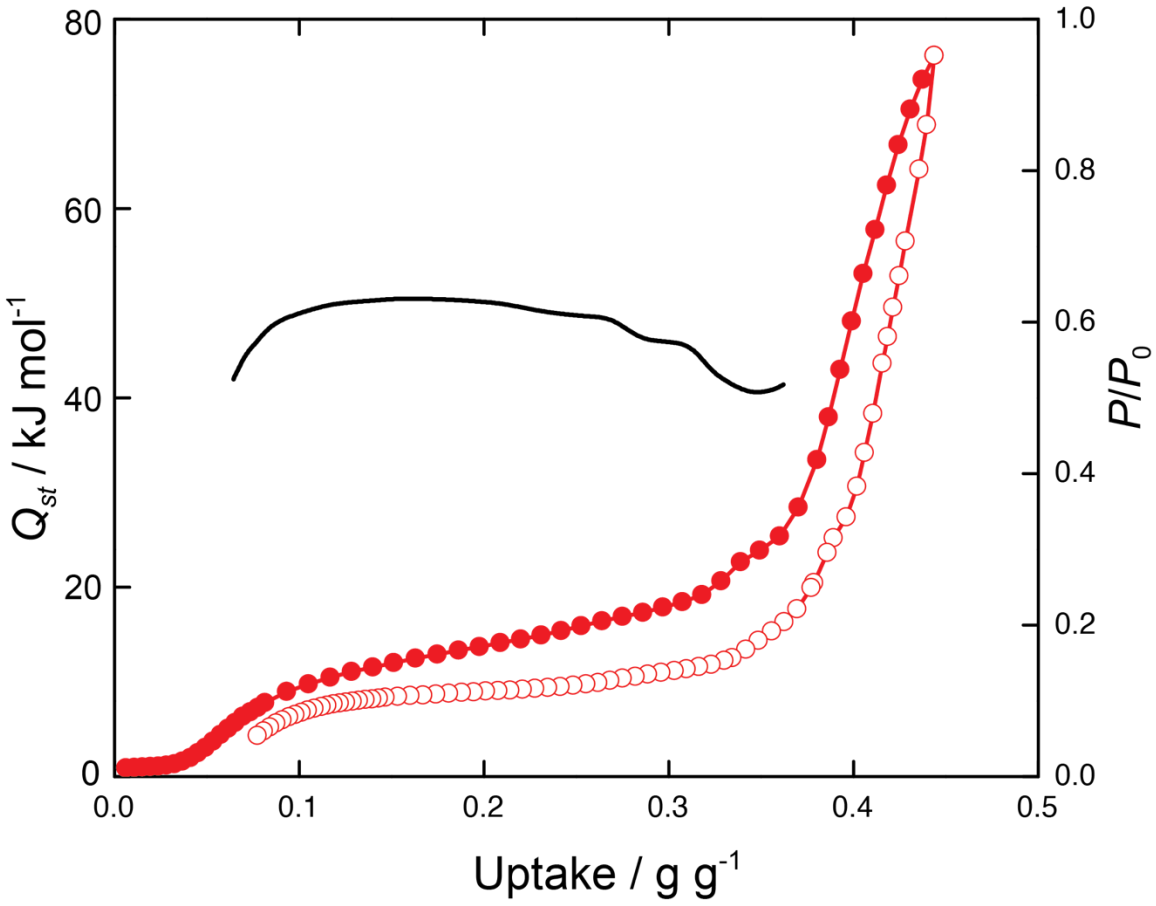

fig. S26. Isosteric heat of adsorption (black) versus water sorption isotherm at 25°C (red) for activated MOF-303.

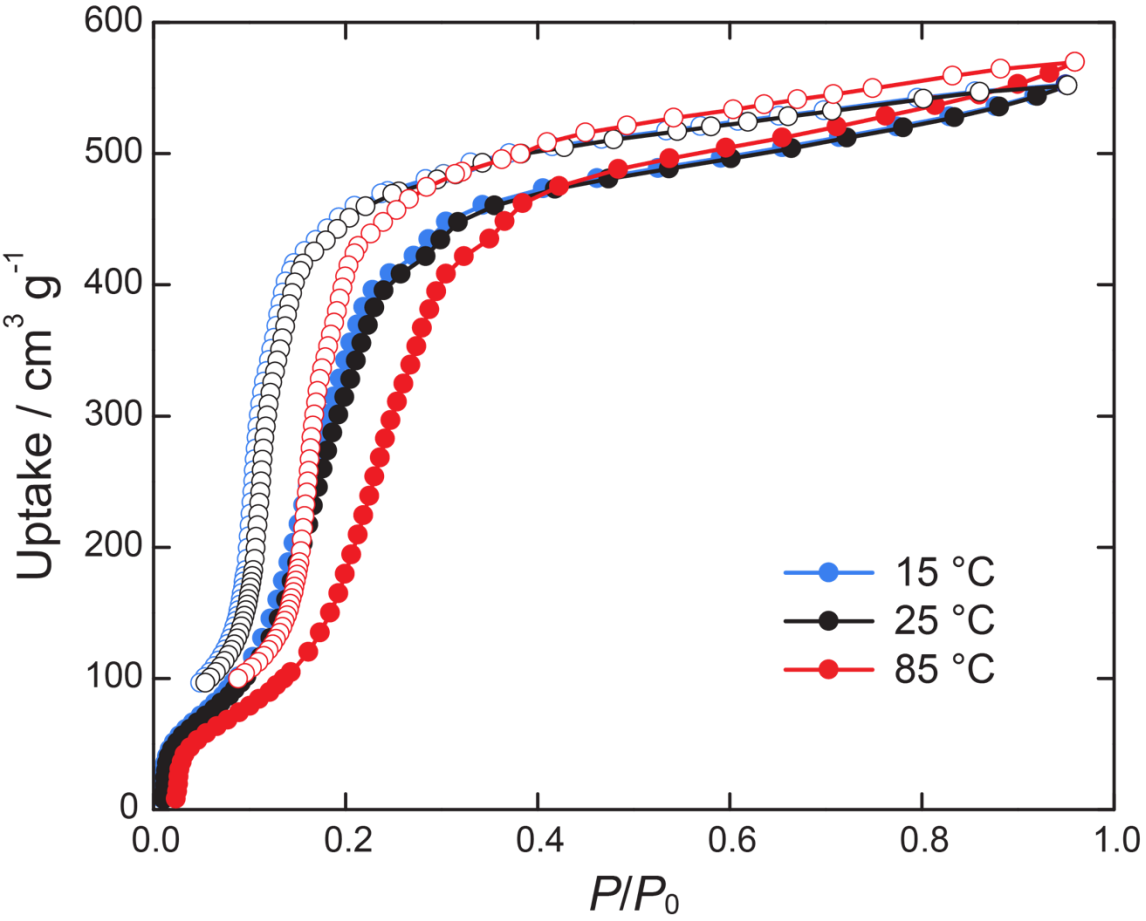

fig. S27. Experimental water sorption isotherm for activated scaled-up MOF-303 at 25°C and calculated water isotherms at 15° and 85°C. A 45 mg sample was taken from 450 g of activated scaled-up microcrystalline powder MOF-303, transferred to a 9 mm bulb gas cell, and charged with N_2 to avoid air contamination. Then the cell was mounted on the instrument.

section S5. MOF-303/G preparation and characterization

section S5.1. Preparation of the mixture

450 g of activated scaled-up MOF-303 was mixed with 150 g of graphite powder in the 2 L jar to produce 600 g of 67:33 wt% MOF-303/G. The resulting mixture was thoroughly mixed by shaking the jar until the MOF-303/G mixture had homogenous gray color. Aggregation of MOF-303 powder into large particles was observed. These aggregates were further crushed using a spatula and remixed. The resulting mixture was further characterized in terms of crystallinity, powder density, porosity and water uptake properties without any additional activation.

section S5.2. Characterization of MOF-303/G

PXRD, EDS analysis, and SEM images of activated MOF-303/G: A powder sample was placed on a zero-background sample holder and was mounted on the diffractometer. The data was collected from 3 to 50 degrees with a step width of 0.01 and a total data collection time of 30 minutes. SEM and EDS images were taken to study the morphology and elemental composition of bulk MOF-303/G powder.

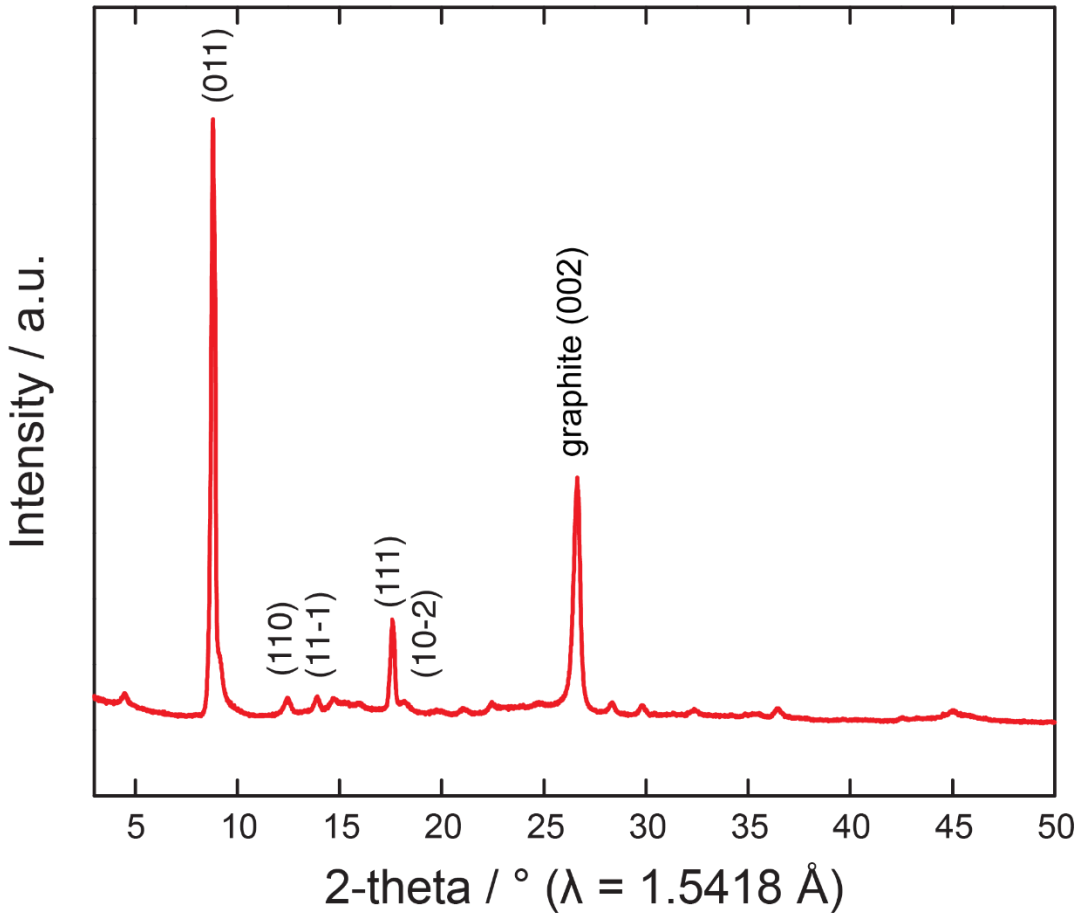

fig. S28. PXRD pattern of activated sample of MOF-303/G. The peak at 26.5º corresponds to the (002) reflection of graphite.

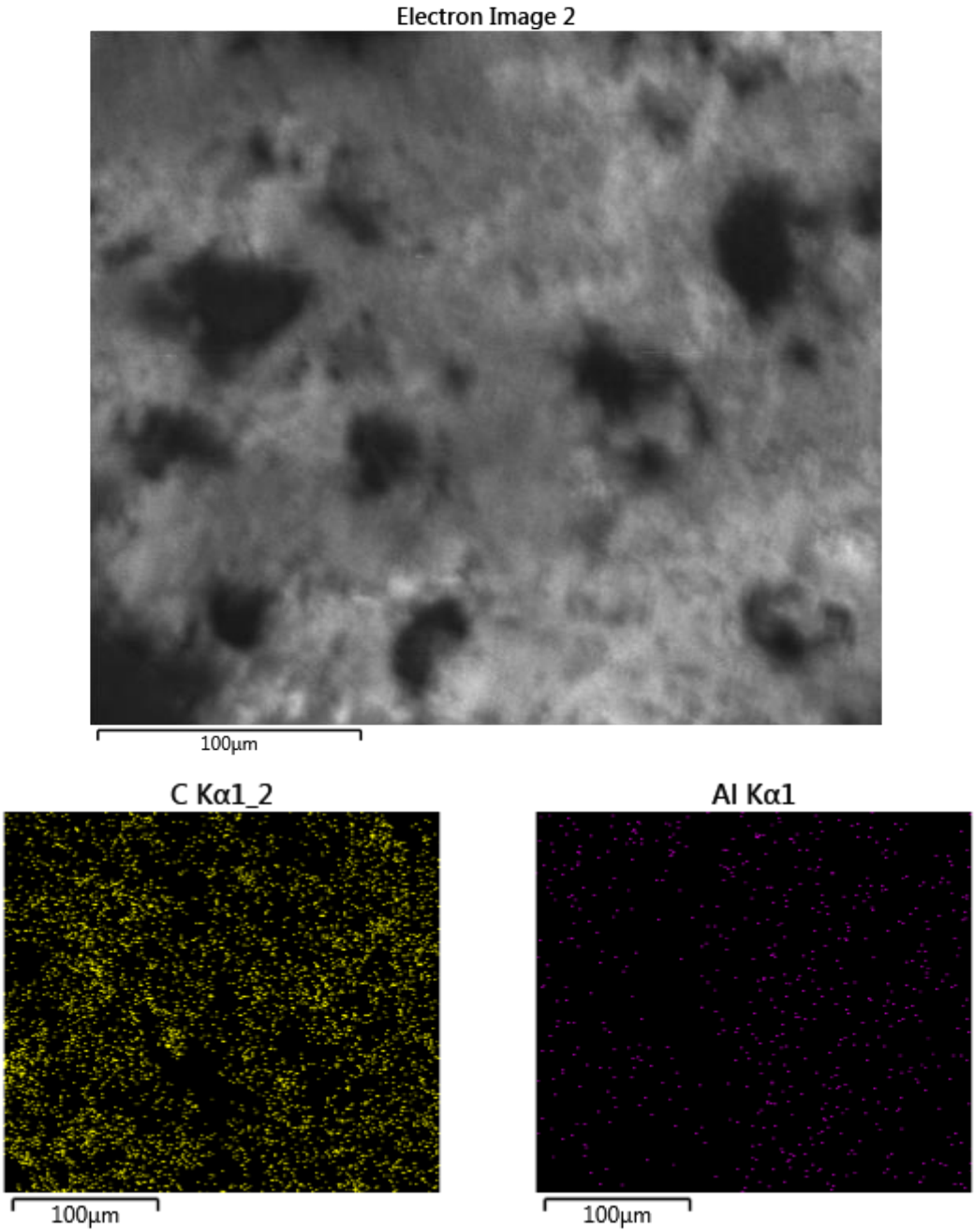

fig. S29. SEM and EDS images of MOF-303/G. SEM image of activated MOF-303/G (top). Carbon and Aluminum EDS images of the MOF-303/G (bottom).

Porosity and packing density analysis: A 65 mg sample was taken from 600 g of well-mixed activated MOF-303/G, transferred to a 9 mm bulb gas cell and charged with N_2 to avoid air contamination. Then the cell was mounted on the instrument. 26 adsorption and 11 desorption points were collected.

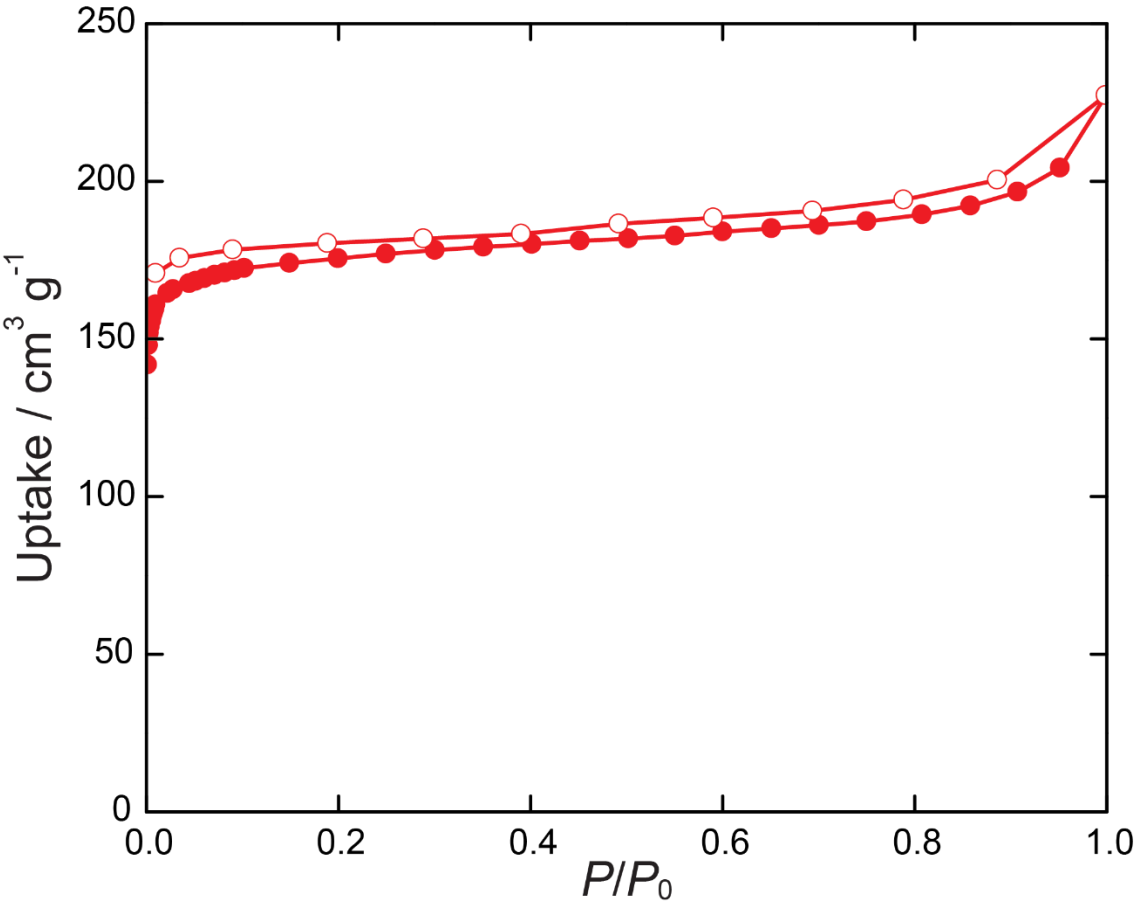

fig. S30. N_2 isotherm of activated MOF-303/G at 77 K. The BET surface area is 701 $m^2 g^{-1}$.

The expected BET surface area for MOF-303/G was determined by multiplying the surface area of pure MOF-303 with the ratio of MOF within in the mixture:
989 m^2 g^{-1} × 67 wt% = 662 m^2 g^{-1}.

The powder particle density (ρ_p) of activated MOF-303/G was estimated to be 1.482 g cm^{-3} from the pycnometer measurement (framework density ρ_s = 2.5452 ± 0.0015 g cm^{-3}) and BET pore volume measurements (V_p = 0.2820 cm^3 g^{-1}) (see equation (1)). The expected powdered particle density is calculated as follows

$$\rho_{MOF-303/G} = \frac{m_{MOF-303/G}}{\frac{m_{MOF-303}}{\rho_{MOF-303}} + \frac{m_{graphite}}{\rho_{graphite}}} = \frac{600\,\text{g}}{\frac{450\,\text{g}}{1.293\,\text{g cm}^{-3}} + \frac{150\,\text{g}}{2.16\,\text{g cm}^{-3}}} = 1.437\ \text{g cm}^{-3}.$$

section S5.3. Evaluation of water capacity properties
A 65 mg sample was taken from the activated MOF-303/G, transferred to a 9 mm bulb gas cell and charged with N_2 to avoid air contamination. Then, the cell was mounted on the instrument.

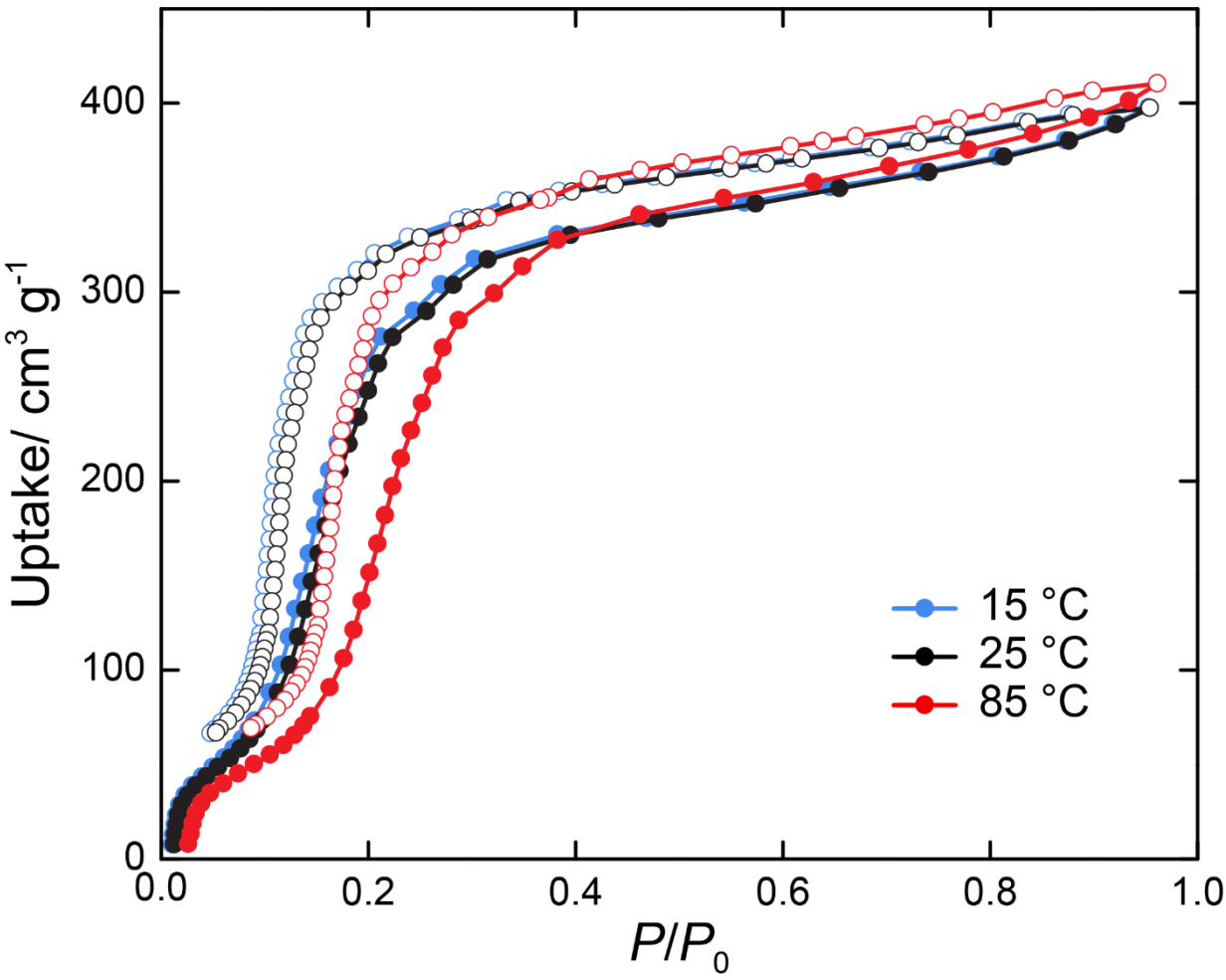

fig. S31. Experimental water sorption isotherm for MOF-303/G at 25°C and calculated water isotherms at 15° and 85°C.

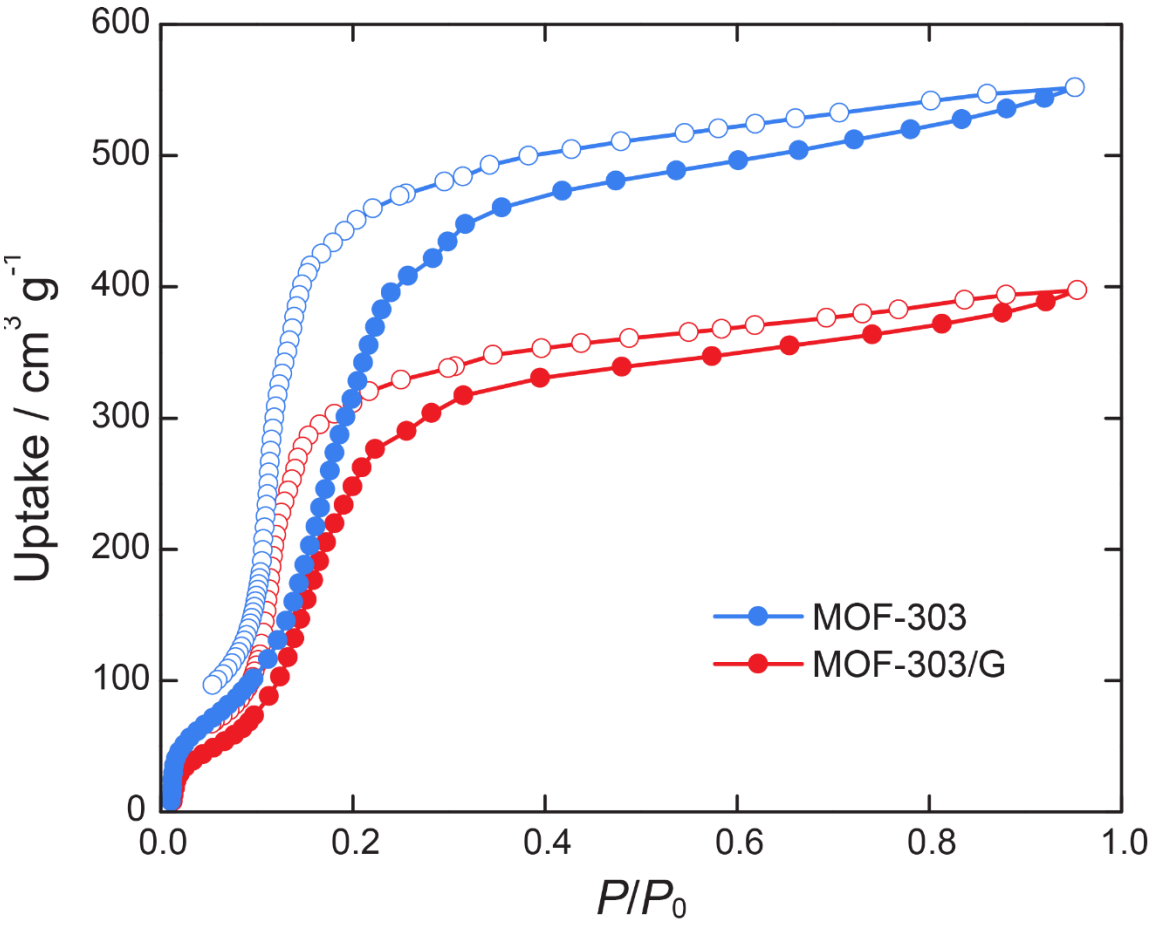

fig. S32. Comparison of water sorption isotherms of scaled-up MOF-303 and MOF-303/G at 25°C. As expected, the water uptake drops by ~ 33 wt% after mixing MOF-303 with 33 wt% of non-porous graphite sample, however, the general shape of the isotherm remains the same.

section S6. Comparison of sorbents

section S6.1. Characterization of Zeolite 13X

A commercially available Zeolite 13X sample was used without any modifications prior PXRD measurement. A powder sample was placed on a zero-background sample holder and was mounted on the diffractometer. The data was collected from 3 to 50 degrees with a step width of 0.01 and a total data collection time of 30 minutes.

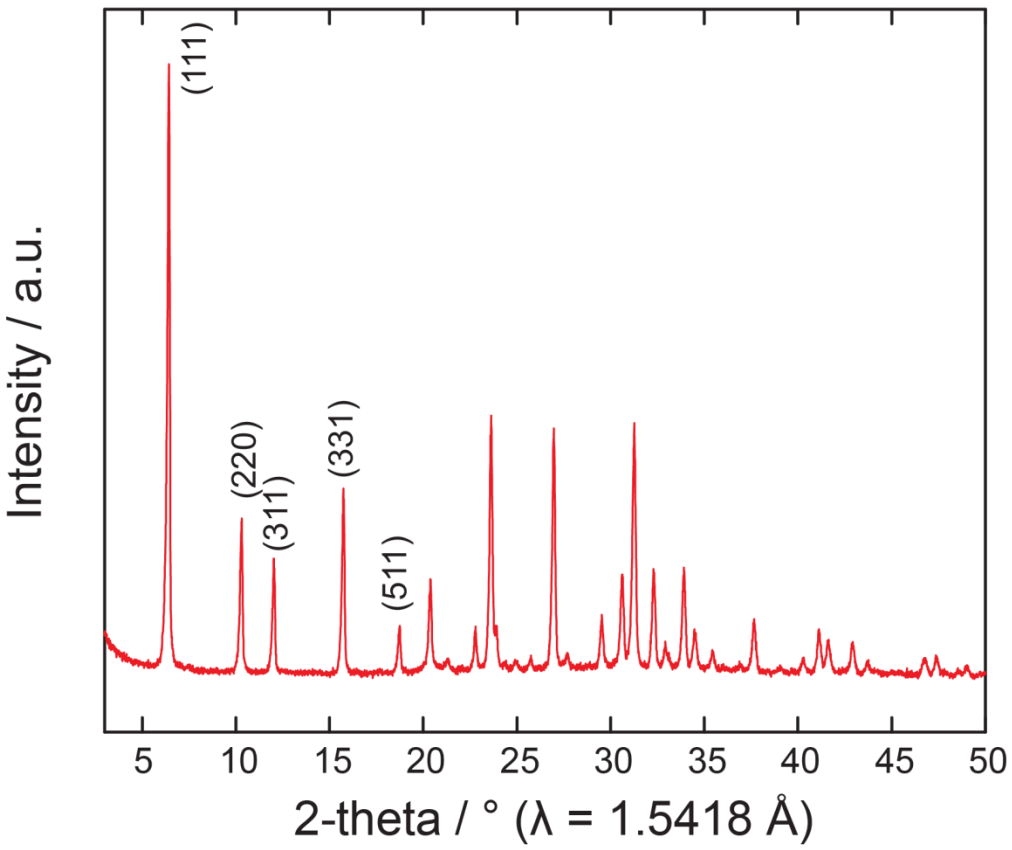

fig. S33. PXRD pattern of zeolite 13X.

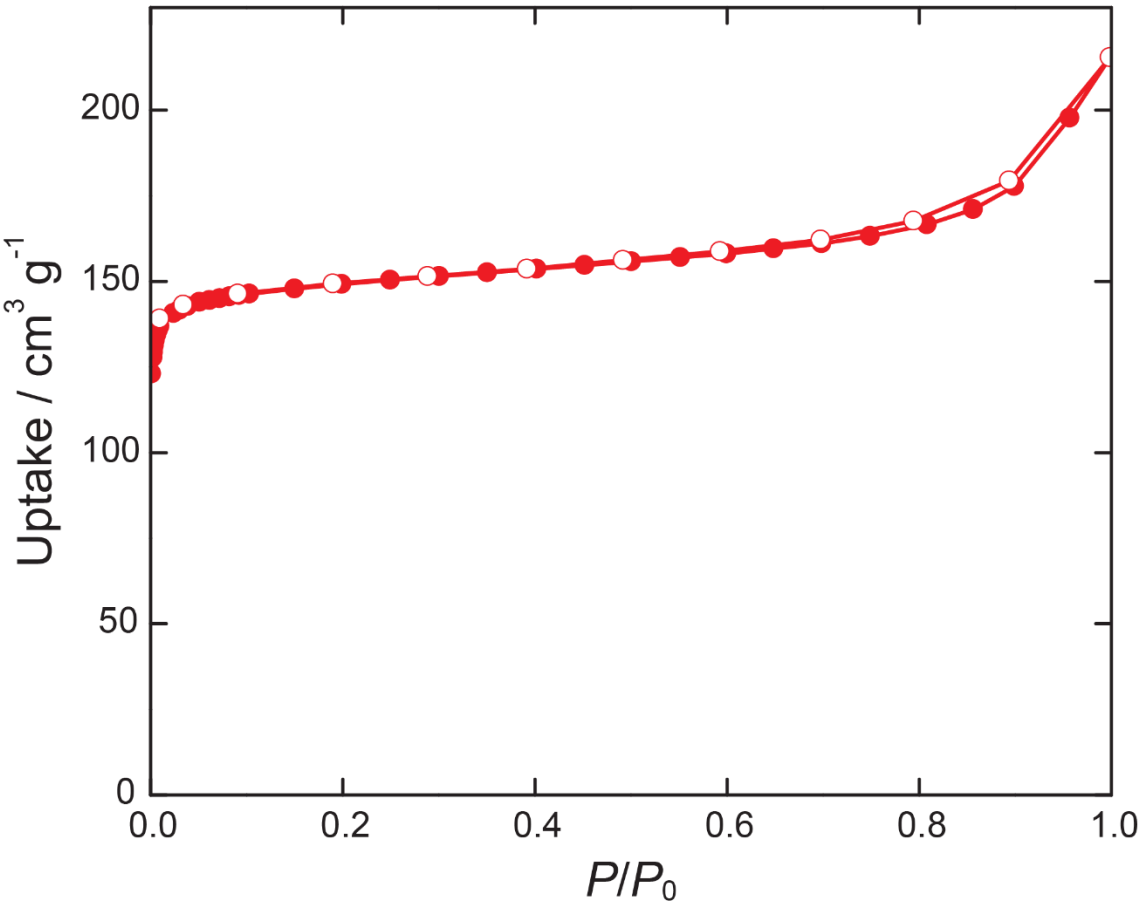

fig. S34. N_2 isotherm of zeolite 13X recorded at 77 K. The BET surface area is 602 m^2 g^{-1}. 53 mg of activated Zeolite 13X were transferred to a 9 mm bulb gas cell and charged with N_2 to avoid air contamination. Then the cell was mounted on the instrument. 26 adsorption and 11 desorption points were collected.

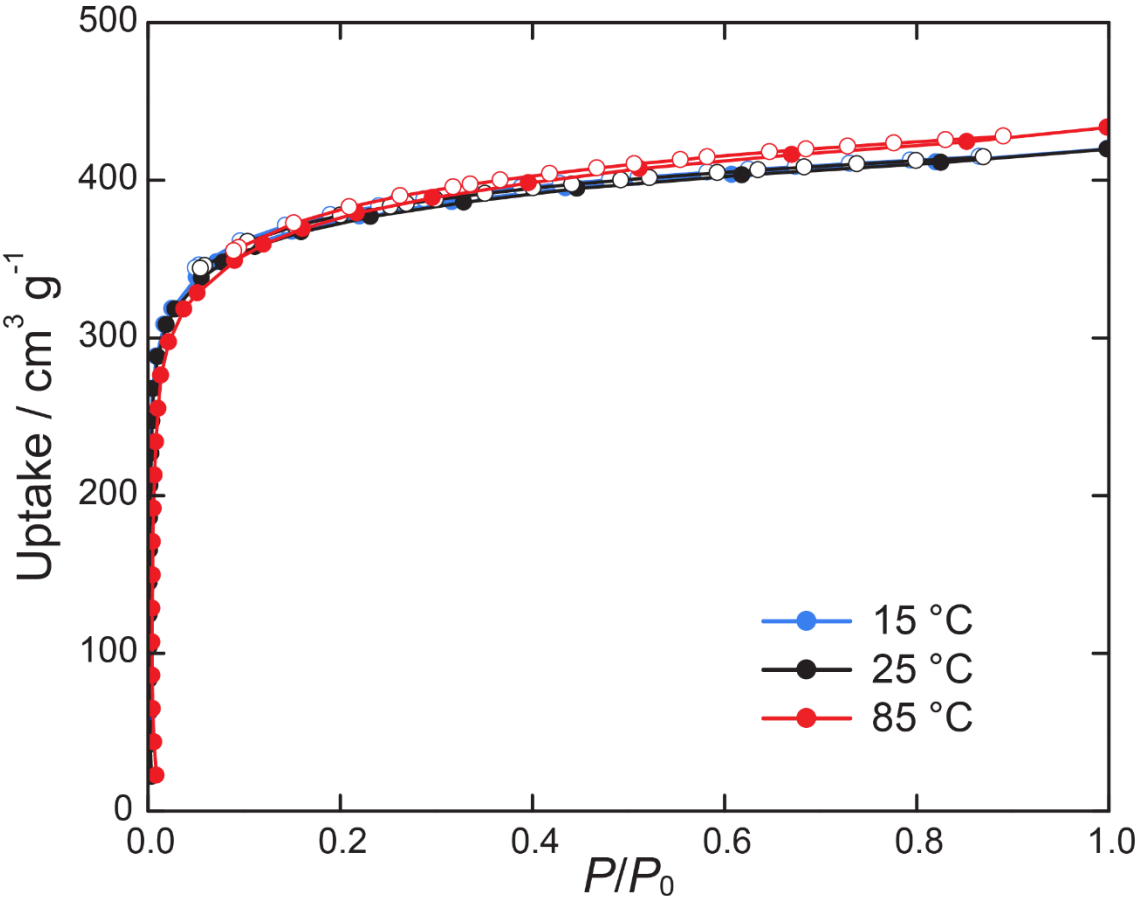

fig. S35. Experimental water sorption isotherm for zeolite 13X at 25°C and calculated water isotherms at 15° and 85°C. 53 mg of activated Zeolite 13X were transferred to a 9 mm bulb gas cell and charged with N_2 to avoid air contamination. Then, the cell was mounted on the instrument to measure the water uptake capacity at 25°C.

section S6.2. Solar flux response

The powder samples were packed in the insulation cell made of extruded polystyrene foam. An incandescent lamp (150 W) was placed 60 cm above the cell to ensure the flux of 1000 ± 30 W m^{-2} with ideal vertical exposure of the cell. The cell temperature was equilibrated with the surroundings prior the flux exposure. The pyranometer was used to monitor the solar flux and the temperature readings were taken at the bottom of the cell. The measurement was done at ambient temperature of 25 ± 0.5°C. 1 g of powder sample was used in all measurements.

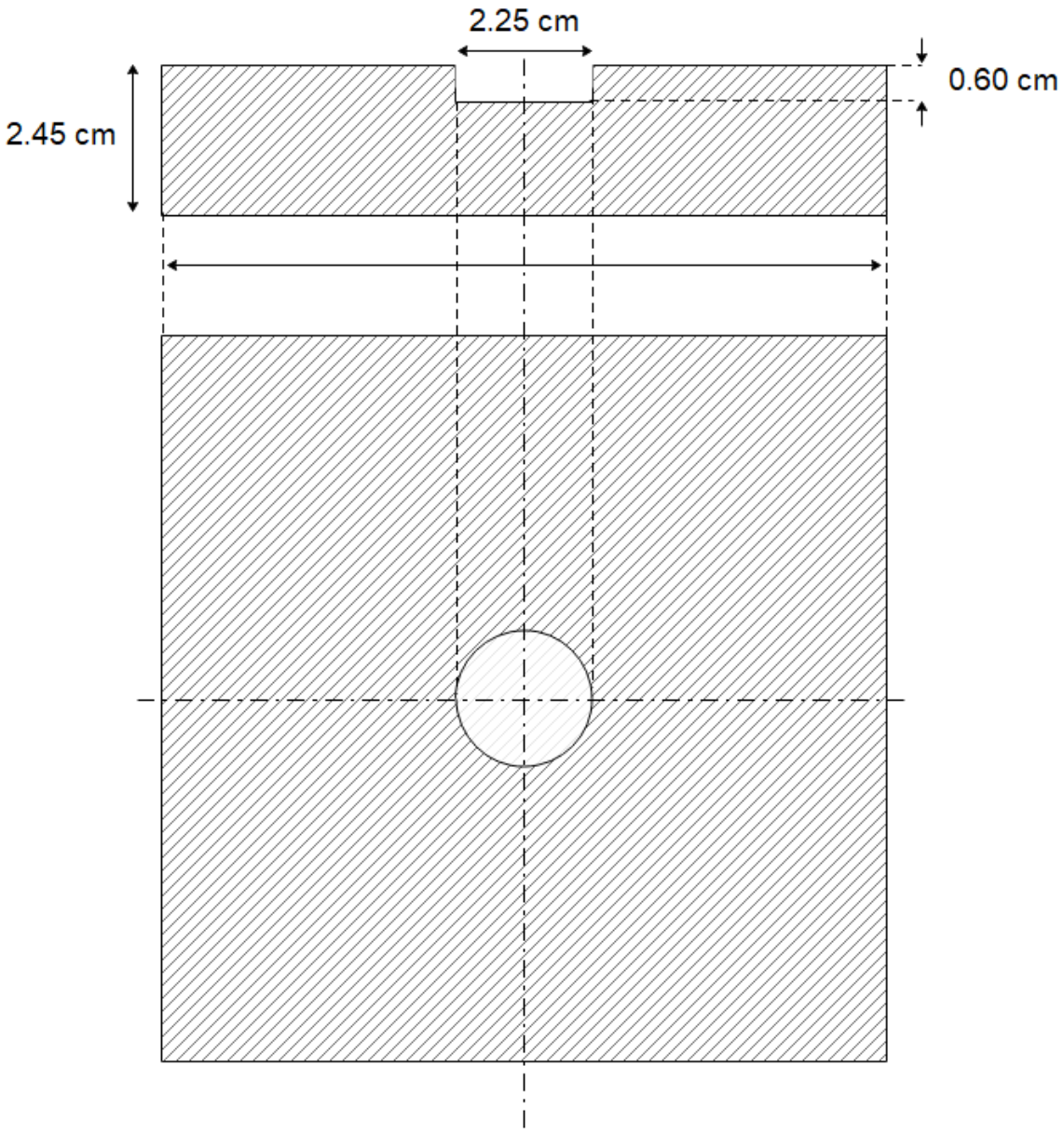

fig. S36. Schematic of insulation cell used for solar flux–temperature response measurements.

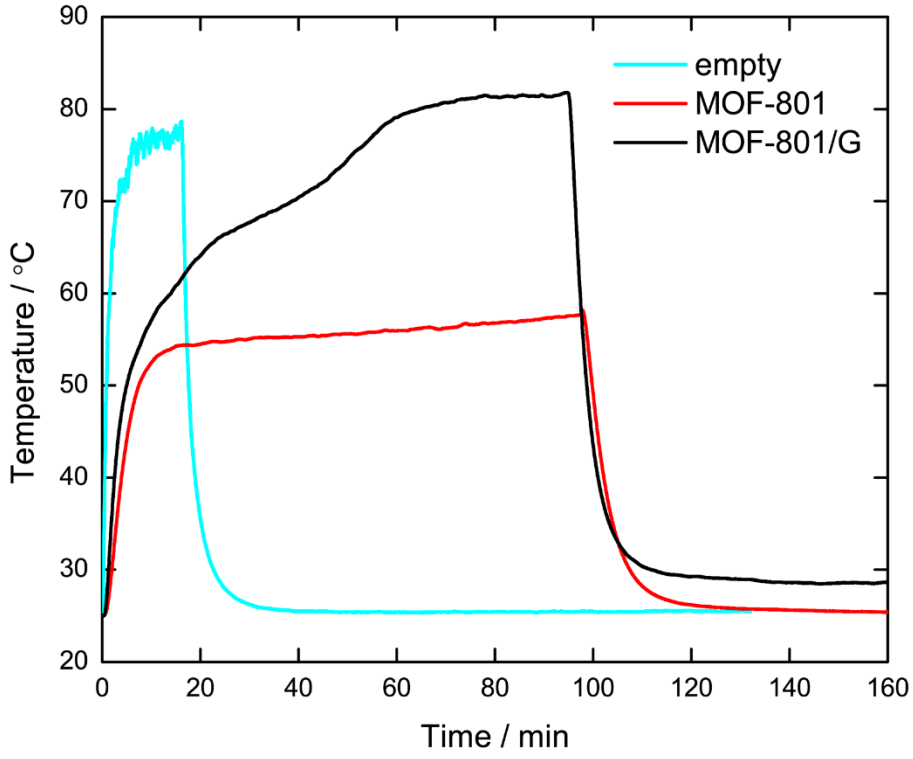

fig. S37. The increase of the sample temperature with time under a flux of 1000 W m^{-2} for MOF-801 and MOF-801/G. The measurement of an empty cell is shown for comparison. The sudden change in temperature increase for MOF-801/G at 70°C is due to desorption of water.

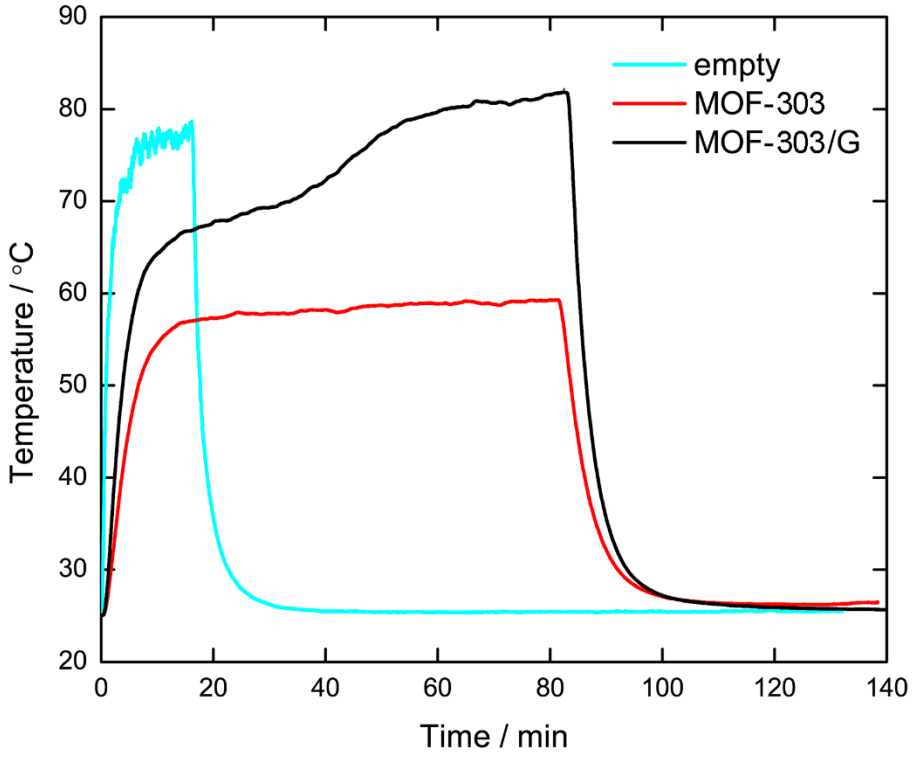

fig. S38. The increase of the sample temperature with time under a flux of 1000 W m^{-2} for MOF-303 and MOF-303/G. The measurement of empty cell is shown for comparison. The sudden change in temperature increase for MOF-303/G at 70°C is due to desorption of water.

section S6.3. Near-IR properties

For the measured samples, a transmission of zero was assumed and the reflectance was transformed into absorption according to equations (4) or (5) for samples of high or low absorption, respectively

$$\alpha = log_{10}\left(\frac{1}{R}\right) \tag{4}$$

$$\alpha = \frac{(1-R)^2}{2R} \tag{5}$$

where α is the absorption, R is the reflectance. A significant increase of the absorption was observed for both MOF-801/G and MOF-303/G compared to the pure samples.

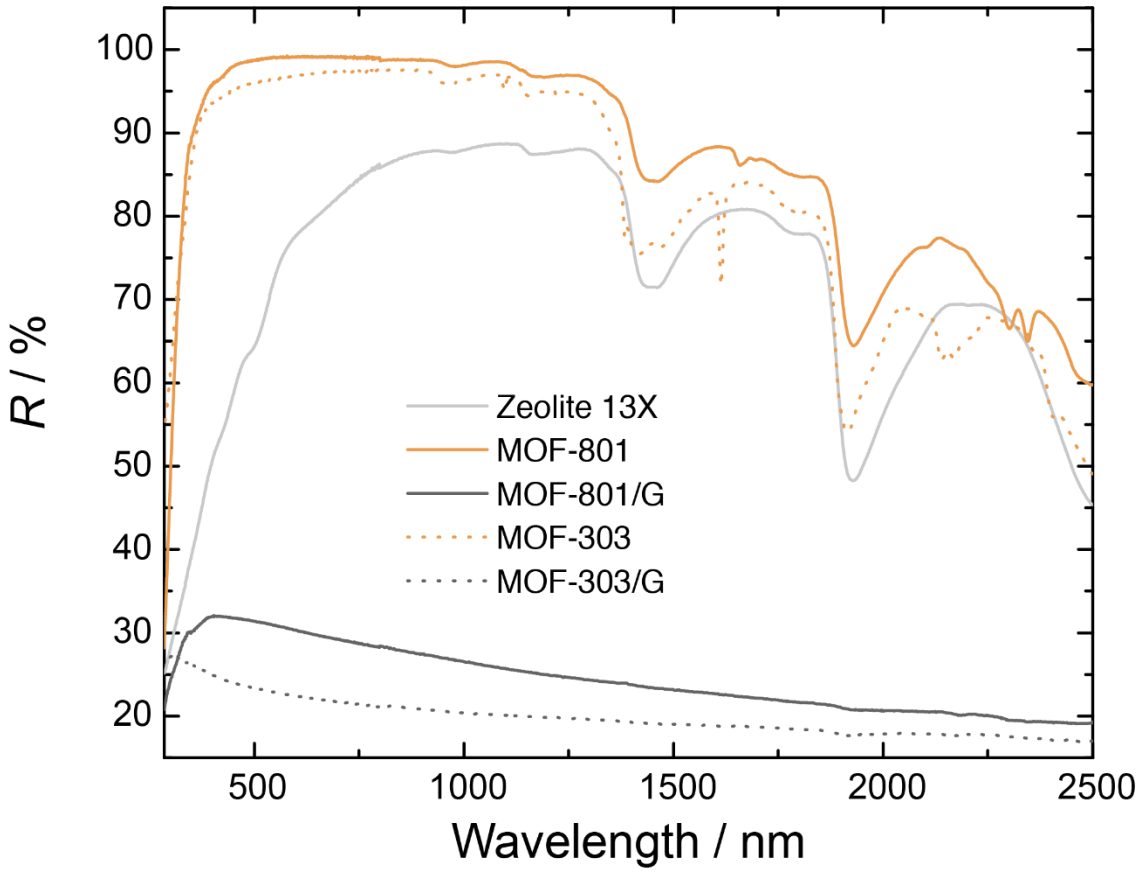

fig. S39. Diffuse reflectance spectra of zeolite 13X, MOF-801, MOF-801/G, MOF-303, and MOF-303/G recorded between 285 and 2500 nm.

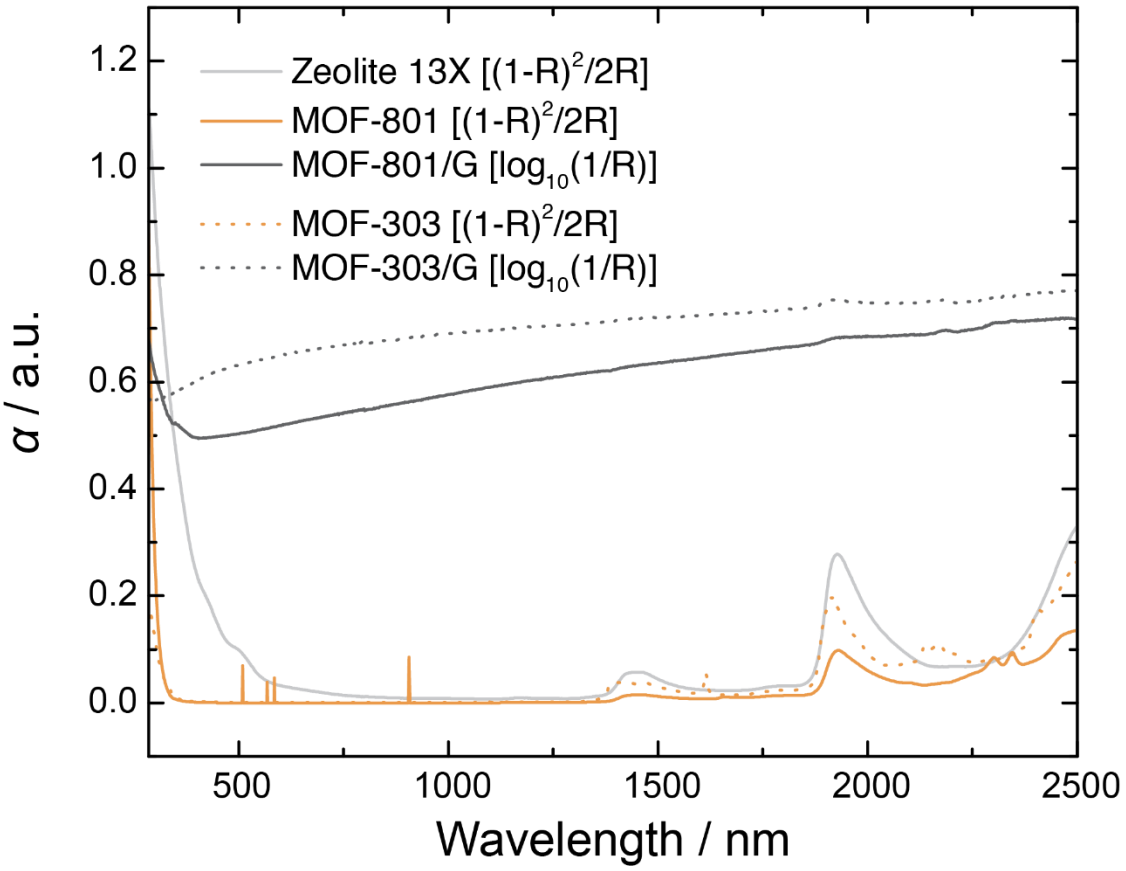

fig. S40. Absorption spectra of zeolite 13X, MOF-801, MOF-801/G, MOF-303, and MOF-303/G between 285 and 2500 nm. The spectra are calculated from the diffuse reflectance data presented in fig. S39 using equations (4) or (5).

section S6.4. Comparison of water kinetics

The powder samples were placed into a platinum pan and heated to 150°C at 0% RH (dry air). Then, the temperature was allowed to equilibrate for 24 hours at 25°C and 0% RH. The adsorption measurement was performed at 25°C and 40% RH; the desorption measurement was performed at 85°C and 0% RH. Weight percentage was estimated as (mass of activated material + mass of adsorbed water) / (mass of activated material).

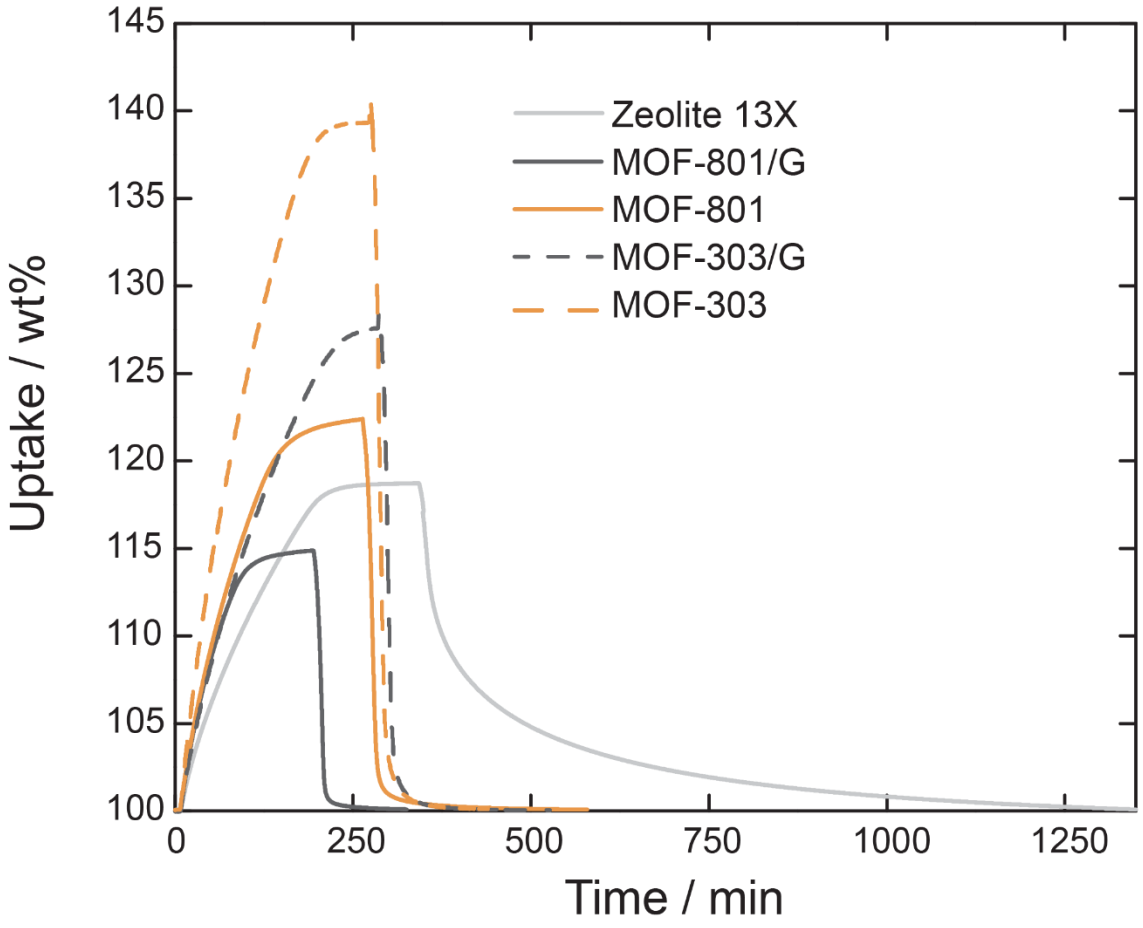

fig. S41. Comparison of water sorption kinetics for zeolite 13X, MOF-801, MOF-303, MOF-801/G, and MOF-303/G.

section S7. Water harvester

section S7.1. Materials

Transparent plexiglass/PMMA (0.5" and 0.25" thick) and T-slotted aluminum framing (Single Rail, Silver, 1-1/2" high × 1-1/2" wide) with connections joins were purchased from McMaster-Carr. The solar absorptive coating (Pyromark 1200 high-temperature paint) was purchased from LA-CO®. High lumen incandescent bulbs (150 watts, 2,710 lumens, 100 CRI) were manufactured by Bulbrite. Extruded polystyrene foams (24" × 24" wide, 1" thick) was purchased from Owens Corning®. Acrylic cement was manufactured by Scigrip. Primer, white and clear gloss 2X paints were manufactured by Rust-Oleum.

section S7.2. Solar flux response

Circular poly(methyl methacrylate) (PMMA) pieces were packed in the insulation cell made of extruded polystyrene foam. The lamp was placed 60 cm above the cell to ensure a flux of 1000 ± 30 W m^{-2} with ideal vertical exposure of the cell. The cell temperature was equilibrated with the surroundings prior the flux exposure. The pyranometer was used to monitor the flux and the temperature readings were taken at the bottom of the cell. All the measurements were carried out at the ambient temperature of 25 ± 0.5°C.

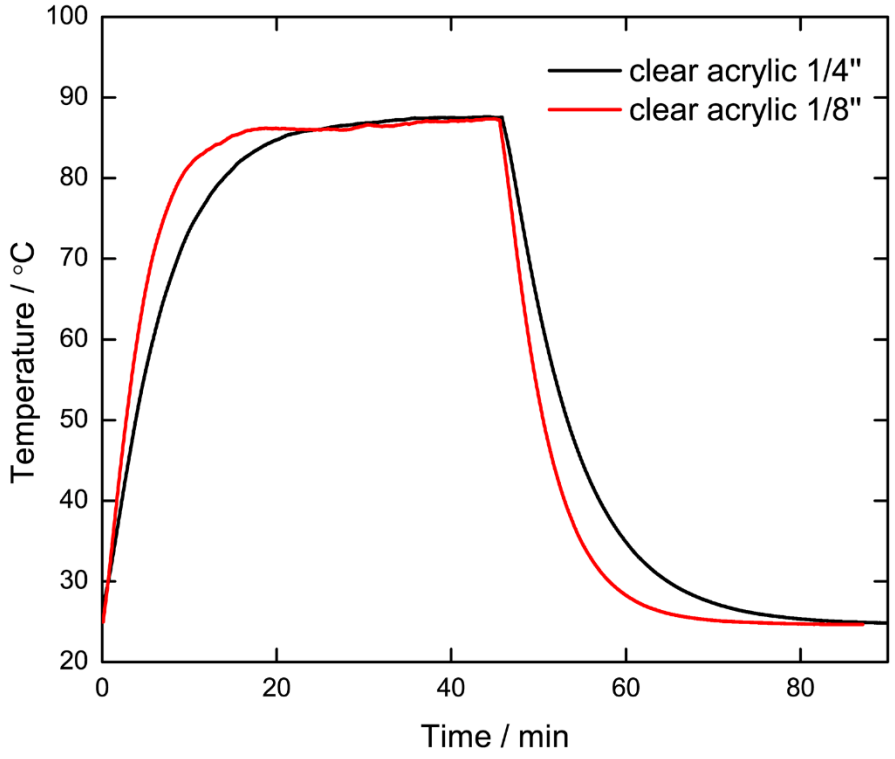

fig. S42. The temperature response with time under a flux of 1000 W m^{-2} measured for circular pieces of PMMA (diameter, 20 mm) with a thickness of $^{1}/_{4}''$ and $^{1}/_{8}''$.

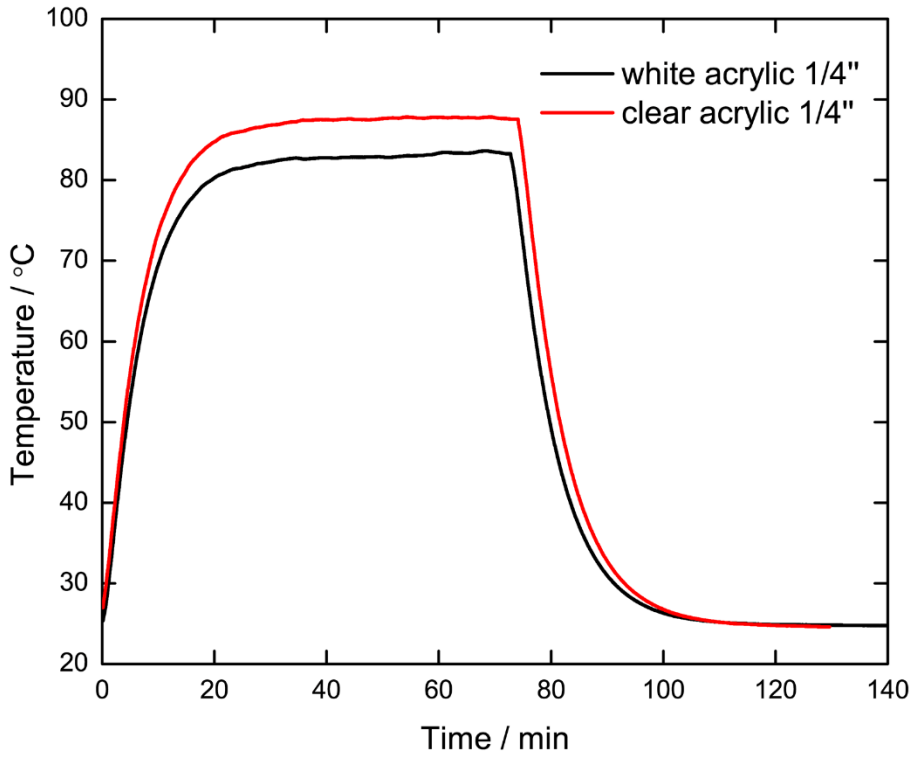

fig. S43. The temperature response with time under a flux of 1000 W m^{-2} measured for circular pieces of PMMA (diameter, 20 mm) of the same thickness ($^1/_4$″) coated with a white (red) and clear coating (black). A 7°C lower temperature was observed in case of the PMMA sample with white coating.

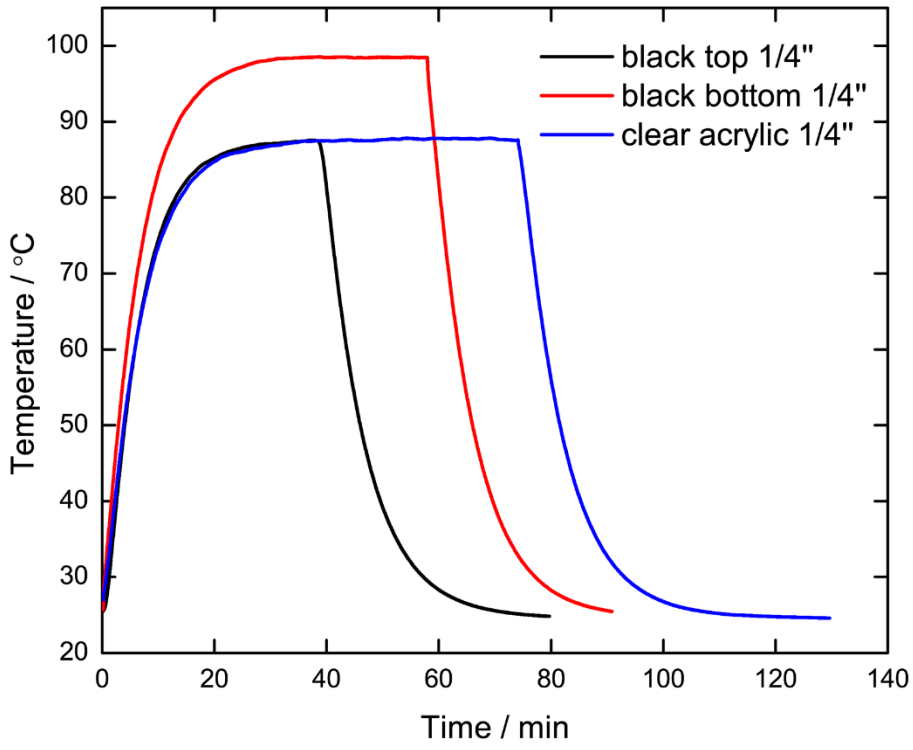

fig. S44. The temperature response with time under a flux of 1000 W m^{-2} measured for circular pieces of PMMA (diameter, 20 mm) of the same thickness ($^1/_4$″) coated with solar absorber coating (Pyromark paint). A comparison of a clear disc of PMMA (blue), and a coated disk in two different orientations, to coated (black) and bottom coated (red) is shown. A 13°C higher temperature was observed for the PMMA disc with pyromark coating on the bottom. The identical profile of temperature variation in the case of the transparent disc of PMMA and that coated on the top implies the preferable direction for heat transfer.

section S7.3. Near-IR properties

Absorption spectra of PMMA were recorded on a Shimadzu UV3600 between 285 and 3000 nm. A PMT detector was used in the UV and visible region, and an InGaAs and cooled PbS detector for long-wavelength detection. The spectrophotometer is equipped with a double monochromator with a wavelength range of 185 to 3300 nm. PMMA identical to that used for the construction of the cover (1/8") was used in all experiments. PMMA was measured uncoated and with thin coats of primer and white paint. For both, primer and white paint, an increase in the absorption in the visible and IR region is observed, which is explained by a higher reflectivity.

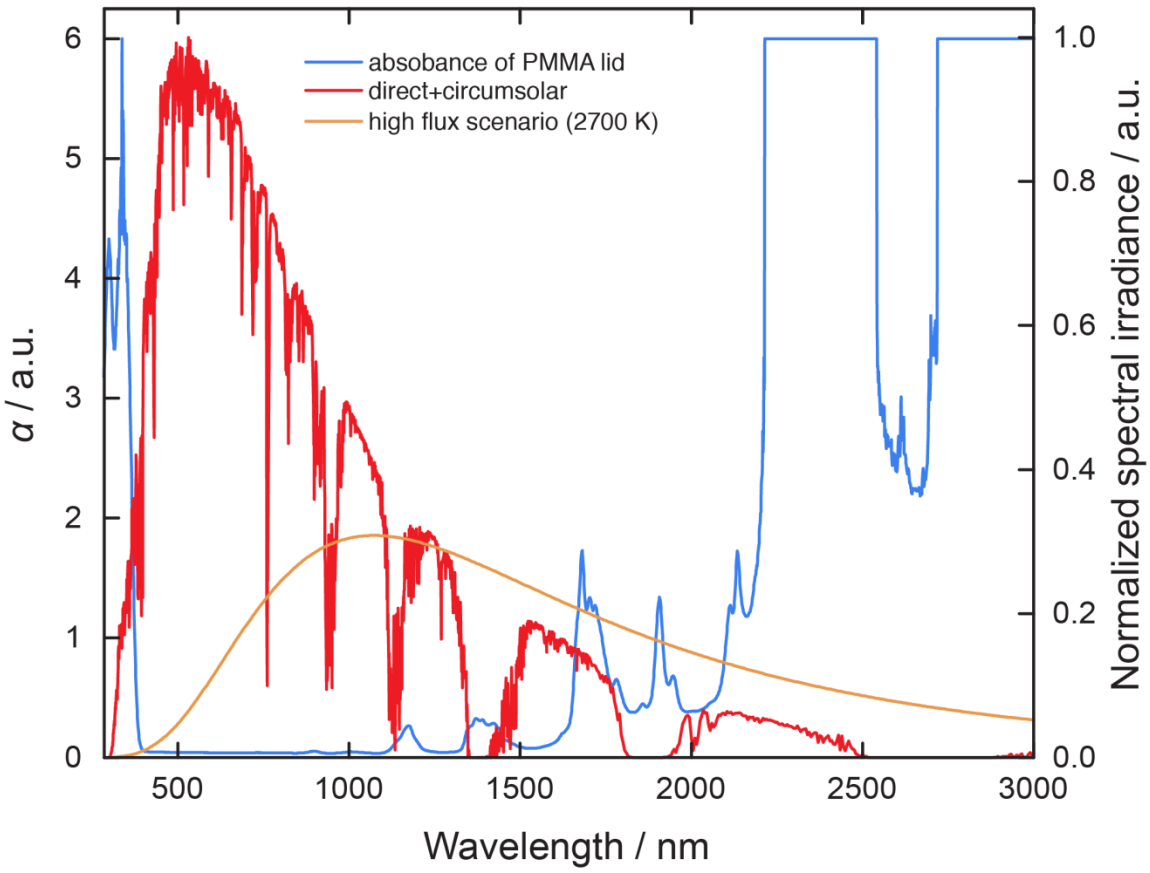

fig. S45. Absorption of PMMA (blue) compared to the spectral irradiance of the sun (red) and an incandescent lamp (orange) between 285 and 3000 nm. PMMA shows strong absorption below 400 and above 2300 nm.

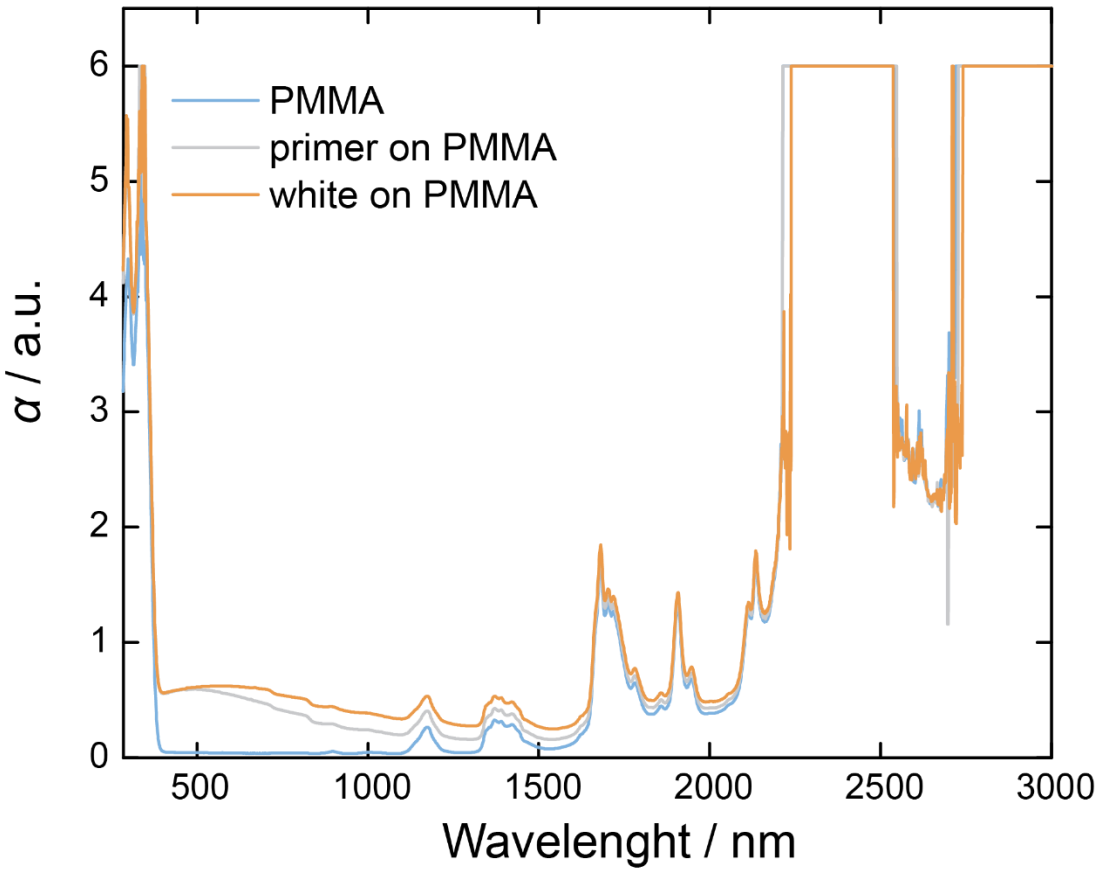

fig. S46. Comparison of absorption spectra for PMMA (light blue), PMMA coated with primer (light gray), and PMMA coated with white paint (orange). For both coated samples, an increase of the absorption in the visible and IR region is observed, arguably due to a higher reflectivity of the surface within the particular spectral range.

section S7.4. Water sorption unit

The water sorption unit is comprised of a sorbent container, support walls, and a thermal insulation compartment. The support walls are four rectangular transparent pieces (18.25" × 8.00" × 0.25") installed onto a bottom acrylic support plate (18.50" × 18.50" × 0.25") to hold the sorbent container at the desired position during the water capture/release. The sorbent container (16" × 16" × 1" deep) is subsequently glued to the upper side of the support walls to create a well-sealed enclosure eliminating water transfer to the thermal insulation.

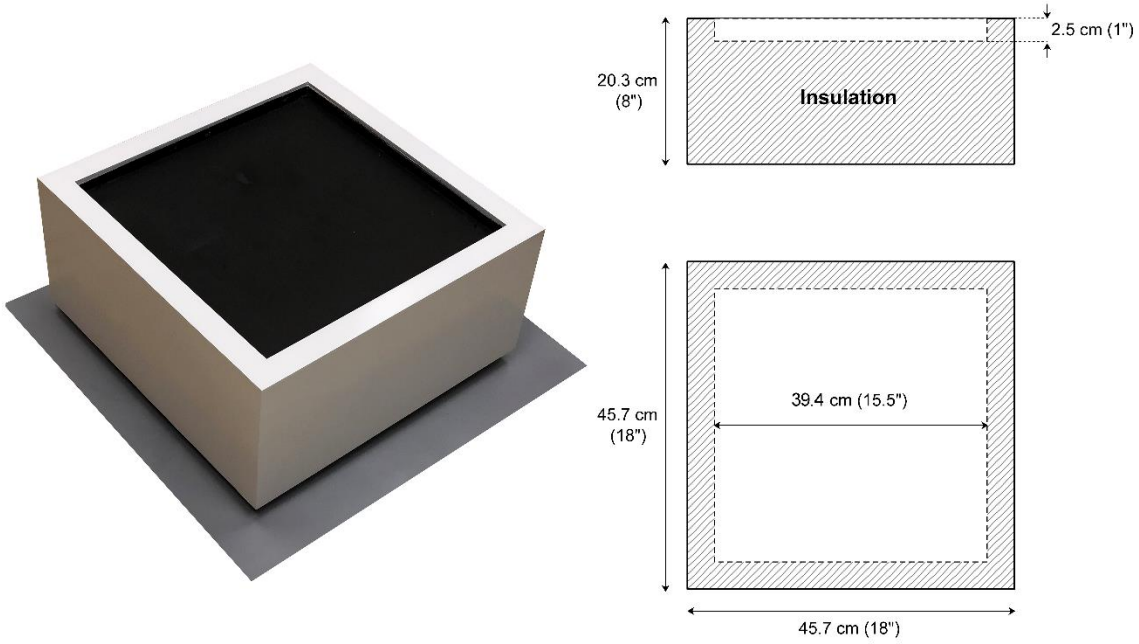

fig. S47. Water sorption unit. Photo of the water sorption unit (left) and schematic representation with dimensions (right).

To increase the temperature of the sorbent during the release period, the bottom surface and the side walls of the sorbent container was coated with a high solar absorptive black coating.

The thermal insulation compartment was packed with extruded polystyrene foam having of thermal conductivity and high heat capacity to minimize heat loss from the side and bottom surface of the container. Fiber glass was also placed between the side walls and the extruded polystyrene foam to avoid any buoyant air circulation within the water sorption unit and minimize the convective heat transfer in the thermal insulation compartment. The exterior surface of the support walls was coated with a white paint with high reflectivity in the infrared region of the solar spectrum to minimize irradiative heating of the water sorption unit and helped to maintain the condenser temperature below the dew point.

section S7.5. Case

The case is comprised of acrylic walls (22" × 22" × 0.25"). The side walls of the case prevent water transfer to/from the surroundings, and they participate in heat transfer occurring within the condenser and the pre-cooled airflow passages. The upper side of the case provides a rigid base for the installation of the cover and the solar reflector while the bottom acrylic plate (22" × 22" × 0.25") of the case is attached to the support frame and the stage (for the desert experiments). The cover is made of a transparent acrylic (24" × 24" × 0.125") with high transmissivity in the visible and near infrared range. The cover is screwed to the top of the case using 12 screws and sealed using a moisture resistant and water impermeable gasket to eliminate any potential gaps and thus prevent leakage.

During the release process, the vapor and heated air flow through airflow passages to the bottom of the case. Condensation is mainly observed on the side walls. The airflow passages are 45 mm wide and allow buoyant air circulation within the closed system. Heat transfer between the air and the side walls of the case is mainly due to convection, while the rejected heat is conducted to the surroundings through the side walls of the case. The droplets on the side walls gradually slide down and accumulate at the bottom of the case separated from the water sorption unit by 2.45 cm spacers.

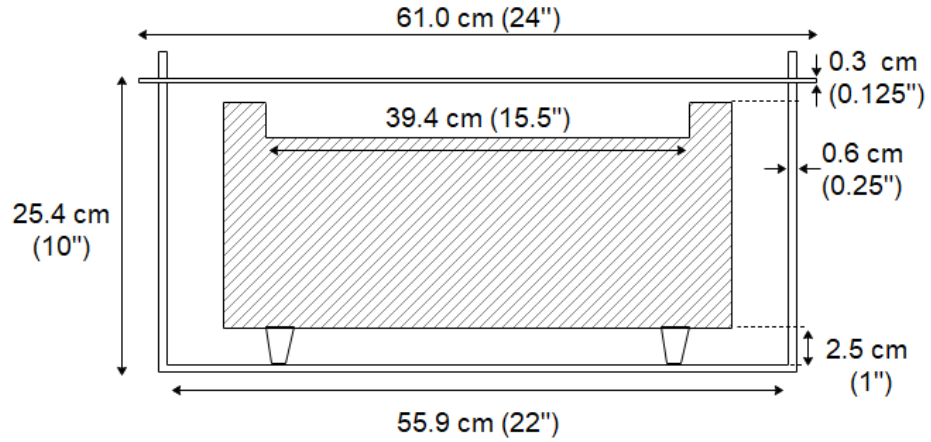

fig. S48. Schematic of the case, cover, and water sorption unit with dimensions.

section S7.6. Solar reflector

A solar reflector is positioned on top of the cover which facilitates (i) collection and deflection of solar radiation onto the sorbent and (ii) shading of the condenser, the exposed surfaces of the water sorption unit, the airflow passages, and the bottom of the case.

section S8. Data acquisition and sensors

Temperature and humidity readings were recorded during the harvesting experiment at various locations insides the case. In addition, the humidity and temperature of the ambient air were measured in close proximity to the water harvester.

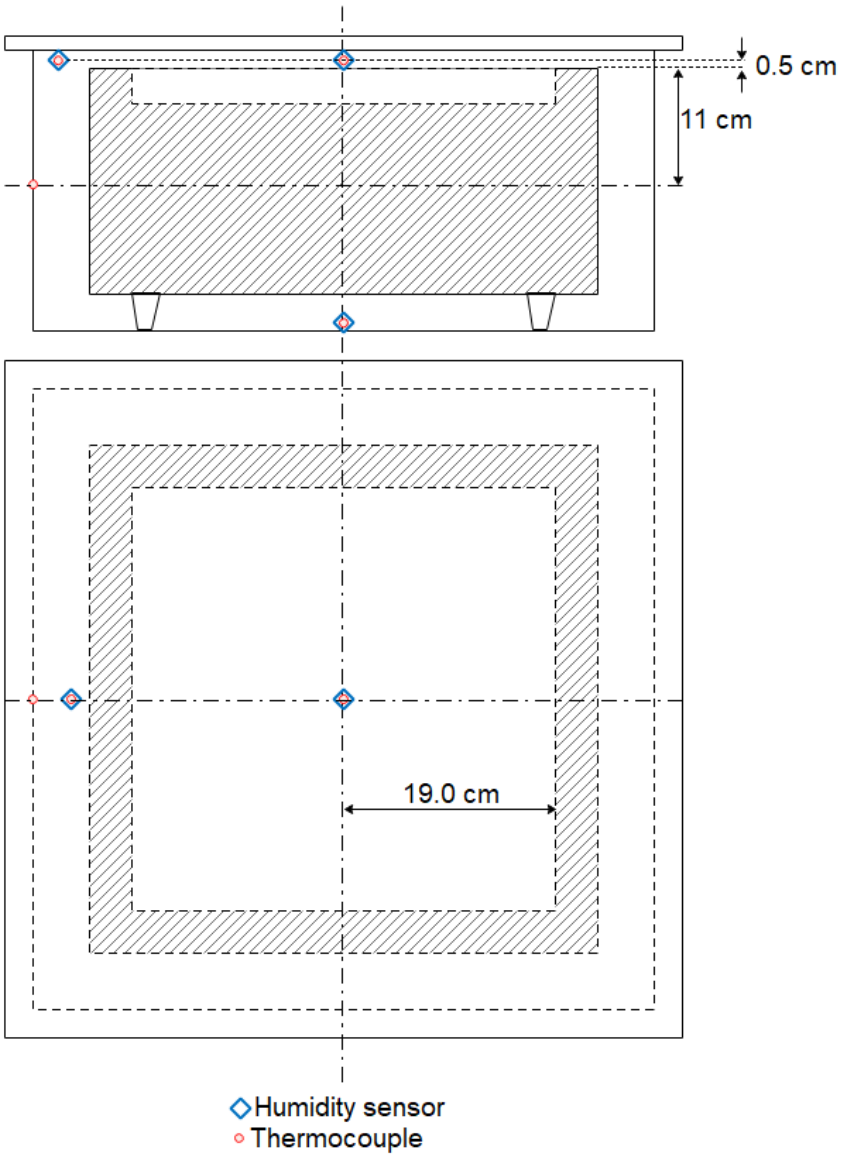

fig. S49. Locations of thermocouples and humidity sensors inside the case.

section S8.1. Humidity measurements

Humidity readings were recorded using integrated circuit sensors (Honeywell HIH-4021) with thermoset polymer capacitive sensing elements. The sensors were relatively small (12 mm × 4 mm × 2 mm) so that they did not significantly interact with the airflow inside the box. The voltage output of the humidity sensors was recorded using a National Instruments data acquisition system (cDAQ-9174 with NI 9205 32-Channel analog input module) and processed using LabView 2016 to collect and visualize the data (*28*). The humidity sensors were calibrated within a range of RH (5% < RH < 90%, with 5% RH increments and at T = 25°C) by using a HygroCal100 humidity generator (Michell Inc, MA, USA). Seven HygroSmart HS3 capacitive humidity sensors (with ±0.8% accuracy) were used to ensure humidity uniformity (less than ±0.5%) across the HygroCal 100 humidity chamber. The bias error was eliminated by using an external standard reference precision dew-point meter (the Optidew Vision precision, Michell Inc, MA, USA) with $\pm 0.2°C_{dew\text{-}point}$ and 0.5% RH accuracy within the relative humidity range of 0.5 to 100%. At each humidity level, the voltage output of the humidity sensors was measured 50 times with a sampling frequency of 30 seconds while the hysteresis effects were determined through a loop of increasing (5% to 90%) and decreasing (95% to 5%) humidity. The precision uncertainty (U_p) of the humidity sensors at each humidity level was calculated using equation (6)

$$U_p = S \times t \tag{6}$$

where S is the precision index, i.e. the square root of standard deviation of analog readings and t the two-tailed student's t-factor (2 for 50 data points). The maximum precision uncertainty for the humidity sensors was found to be ±0.01%. Linear regression was applied to convert sensor voltage output (0.5-3.0 V) to relative humidity (0-100%) (fig. S50). The large coefficient of determination ($R^2 > 0.99$) confirmed the linear response of the sensor at constant temperature resulting in a bias uncertainty of the data reduction, U_{fit}, of less than ±0.6%. The total bias uncertainty (U_B) of 0.7%, coming from the bias uncertainty in the reference humidity (U_{ref} = 0.5%) and the bias uncertainty of the data reduction (U_{fit} = 0.6%), was calculated using equation (7)

$$U_B = \left(U_{fit}^2 + U_{ref}^2\right)^{1/2} \tag{7}$$

The total uncertainty (U_T) in the humidity measurements was found to be less than ±1% according to equation (8)

$$U_T = \left(U_P^2 + U_B^2\right)^{1/2} \tag{8}$$

A temperature compensation relation, equation (9), provided by the manufacturer was used to adjust the relative humidity values at different temperature

$$RH\left(T\right)=\frac{RH\left(25°C\right)}{\left(1.0546-0.00216T\right)} \tag{9}$$

where T is the working temperature in degrees Celsius. It should be noted that although the temperature compensation relation can be used to determine the relative humidity at elevated temperatures, the uncertainty in humidity readings may increase drastically at higher temperature and relative humidity (e.g. ±5% RH when RH = 80% and T = 85°C).

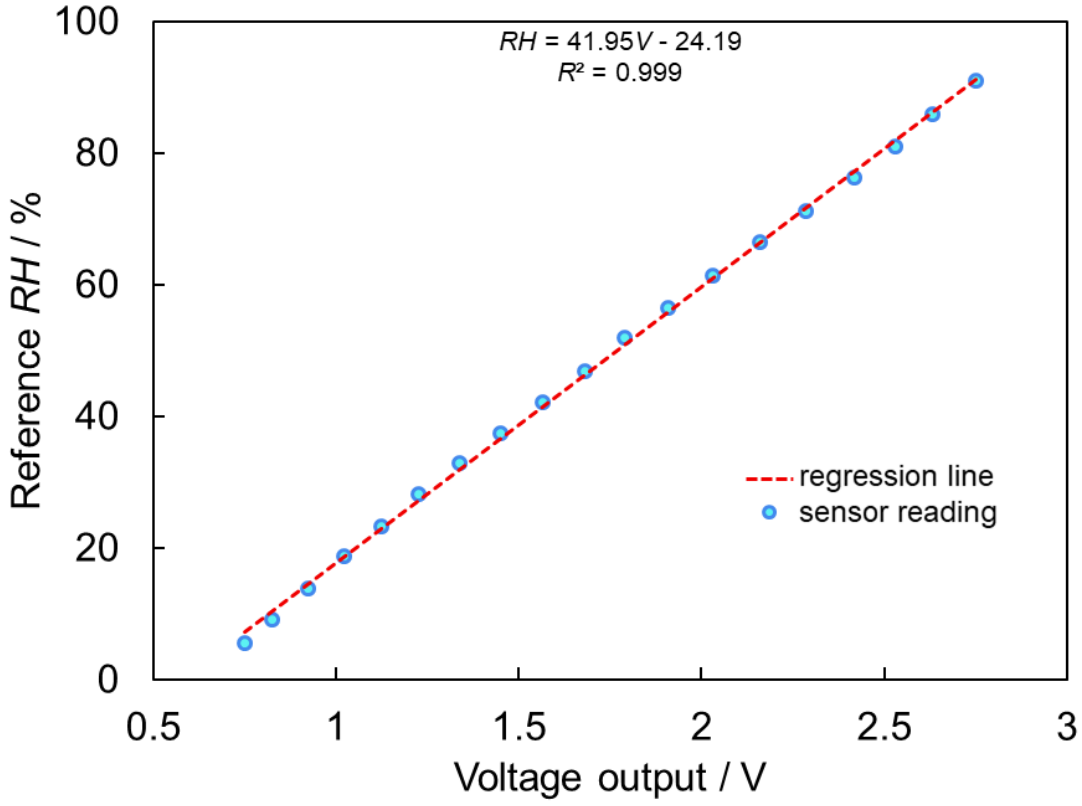

fig. S50. Calibration curve for humidity sensor converting the voltage output readings into the corresponding RH.

section S8.2. Temperature measurements

T-type thermocouples (Neoflon PFA, American Wire Gauge 40, Omega Eng.) were used for temperature measurements. The output signal of the thermocouples was acquired using a National Instruments data acquisition system (cDAQ-9174 with NI 9214 16-Ch Isothermal TC module) and processed using LabView 2016 to collect and visualize the data. The thermocouples were calibrated within the range of 15-105°C with 5°C increments using a Hart Scientific 9103 dry-well calibrator with the accuracy of ±0.25°C. At each reference temperature, 40 readings with a sampling rate of 5 s were taken while hysteresis effects were determined through an increasing and decreasing temperature loop. Using equation (6) with the student's t-factor of 2, the precision uncertainty was found to be less than ±0.01°C. A linear regression curve was used for data reduction which resulted in a bias error of ±0.04°C. Using equation (8) the maximum total uncertainty in the temperature readings was found to be less than ±0.25°C.

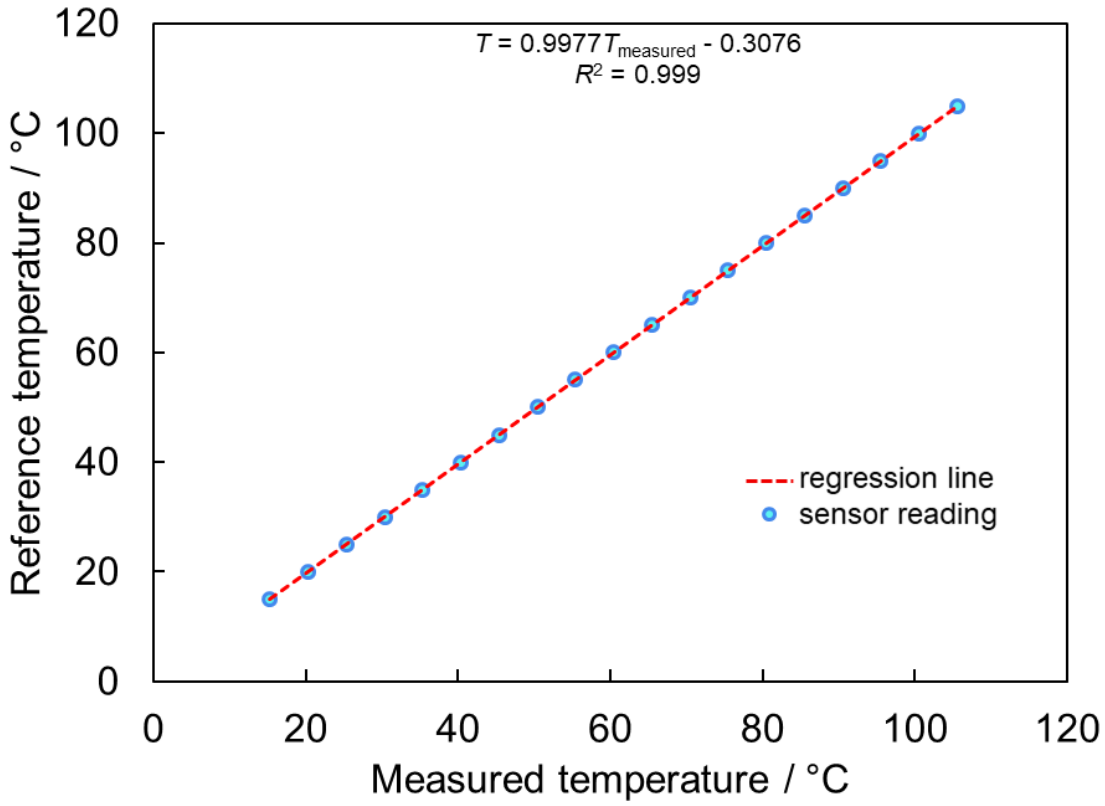

fig. S51. Calibration curve for the temperature sensor.

section S9. WHC under laboratory conditions

section S9.1. Artificial flux generator

In order to compare the irradiation under natural sunlight and that recorded for the harvesting experiment at laboratory conditions, the irradiance for the exposed top surface of the water harvester was scanned. For this purpose, two lamp configurations were tested (two and three lamps) and 25 data points were collected per run. The lamps were adjusted so that the pyranometer reading in the center of the cover of the case was within the range of the readings during the lab experiments reported in this work (830 W m^{-2} and 1140 W m^{-2} for two and three lamps, respectively). Two runs were performed for the two lamp-, and four runs for the four-lamp configuration. Based on these measurements, a correction factor for both configurations was calculated. The average irradiance (W m^{-2}) calculated for two lamps equals 67.25% and that calculated for three lamps equals 69.56% of the value measured in the center of the cover. For every run, two orientations, rotated by 90° with respect to each other were used (100 data points). This correction factor allows for a qualitative comparison of the solar irradiance (based on data provided by ASTM G173-03 Reference Spectra Derived from SMARTS v. 2.9.2, direct + circumsolar) and the theoretical spectra of the lamps, calculated using Planck's radiation law (see equation (10)) and a temperature of 2700 K, within the range of 285-3000 nm (the spectral range recorded by the pyranometer)

$$\dot{E}_{lab}(\lambda) = \frac{c_1}{\lambda^5} \frac{1}{e^{c_2/\lambda T} - 1} \tag{10}$$

where c_1 is $3.741832 \cdot 10^{-16}$ W m^2, c_2 is $438786 \cdot 10^{-2}$ K m, λ is the wavelength, T the temperature of the black body, and $\dot{E}_{lab}$ is the spectral irradiance. The resulting spectra are shown in fig. S52 (two lamps) and fig. S53 (three lamps). The distribution of incident flux measured for one orientation and an average of all orientations are given in fig. S52 and S53 for two and three lamps, respectively.

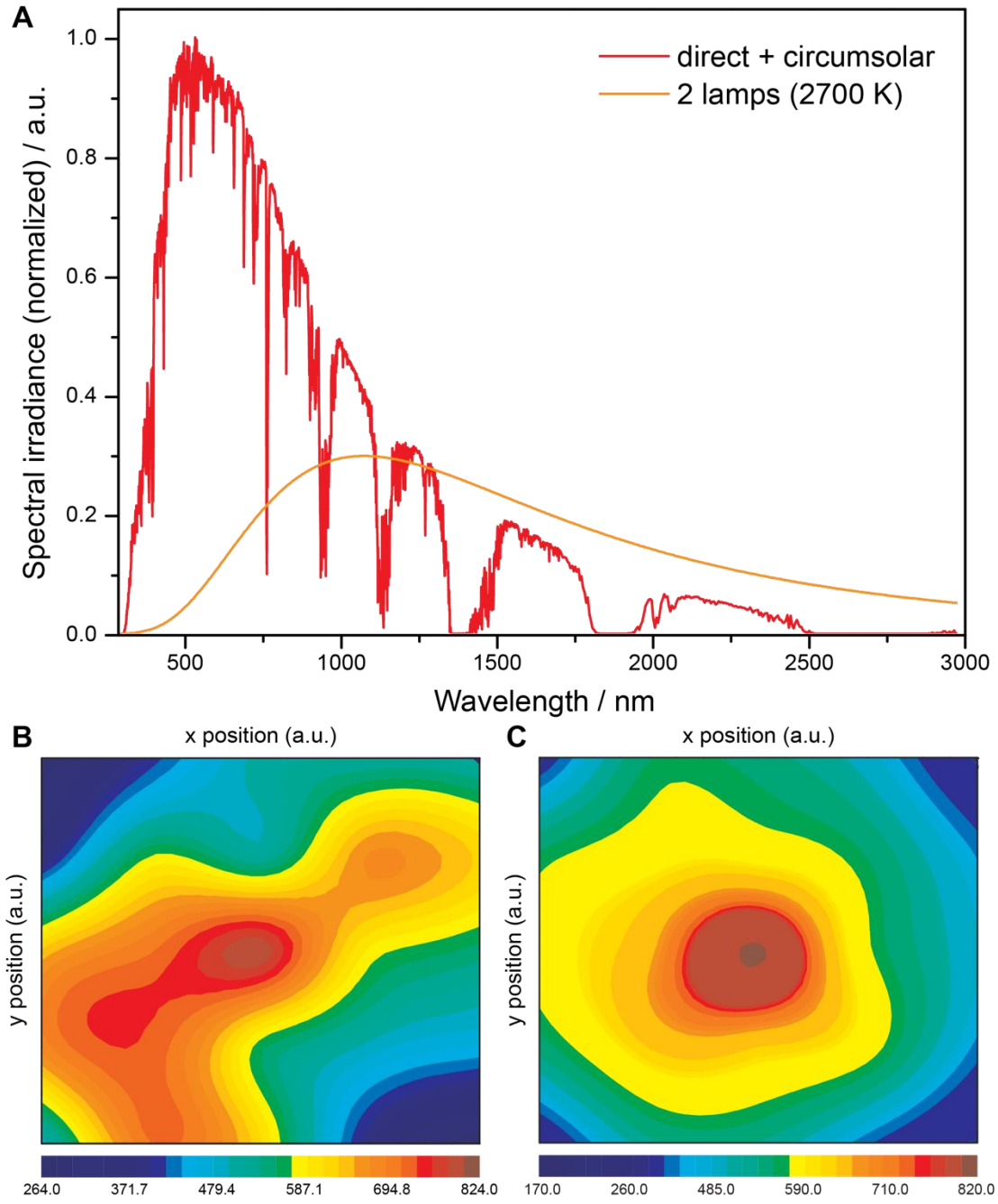

fig. S52. Artificial solar irradiance for low flux condition. (**A**) Comparison of the solar irradiance (red) and the irradiance for a two-lamp configuration (orange line) with a color temperature of 2700 K. (**B**) Contour diagram of the distribution of the irradiance measured on the cover of the case for a two-lamp configuration in one orientation using 25 data points (lamps located at the bottom left and top right). (**C**) Contour diagram of the distribution of the irradiance on the cover of the case for a two-lamp configuration and two different orientations with lamps located at the bottom left and top right, or on the top left and bottom right.

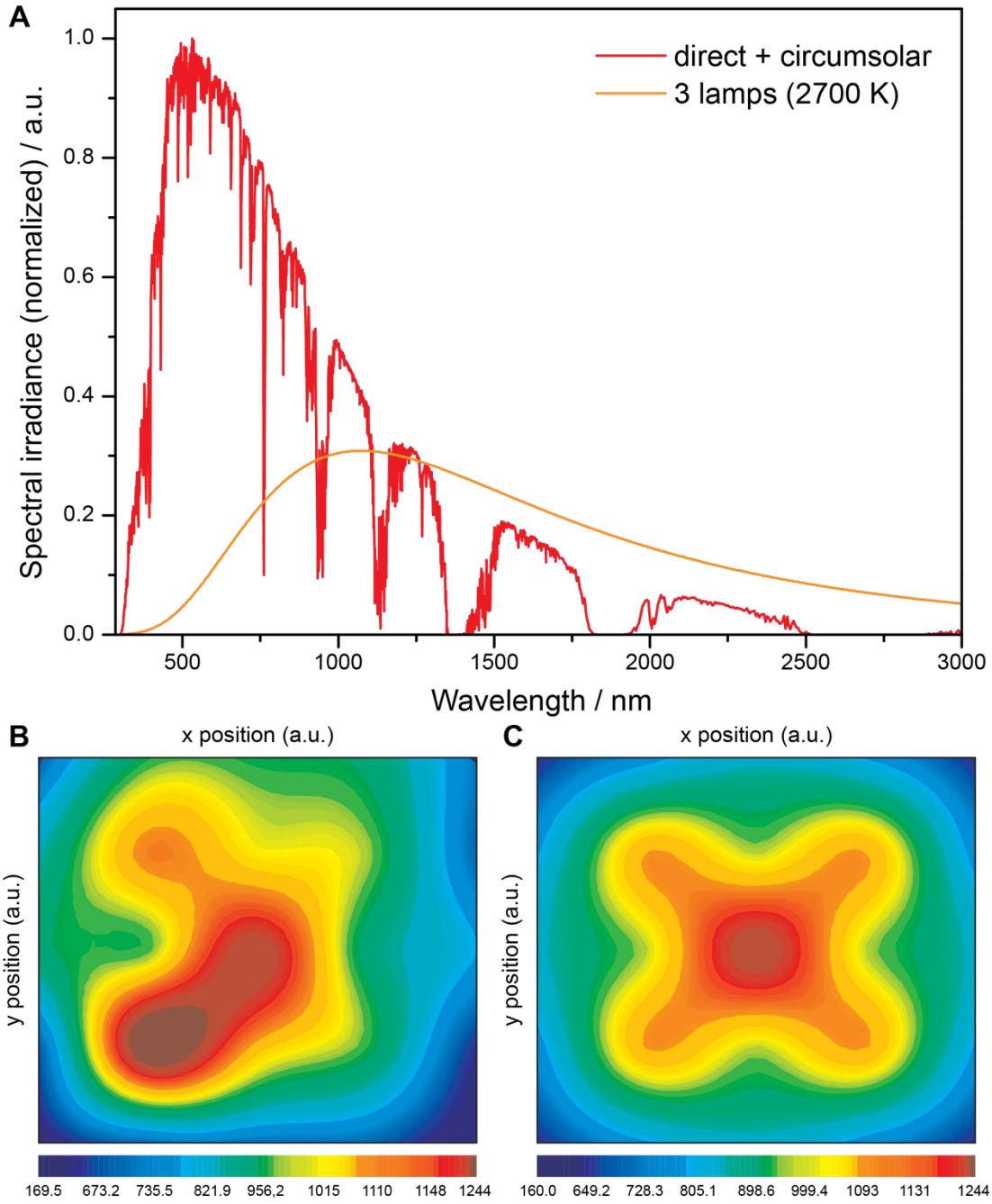

fig. S53. Artificial solar irradiance for high flux condition. (**A**) Comparison of the solar irradiance (red) and the irradiance for a three-lamp configuration (orange line) with a color temperature of 2700 K. (**B**) Contour diagram of the distribution of the irradiance measured on the cover of the case for a three-lamp configuration in one orientation using 25 data points (lamps located at the bottom left, bottom right, and top right). (**C**) Contour diagram of the distribution of the irradiance on the cover of the case for a three-lamp configuration and four different constellations of lamps.

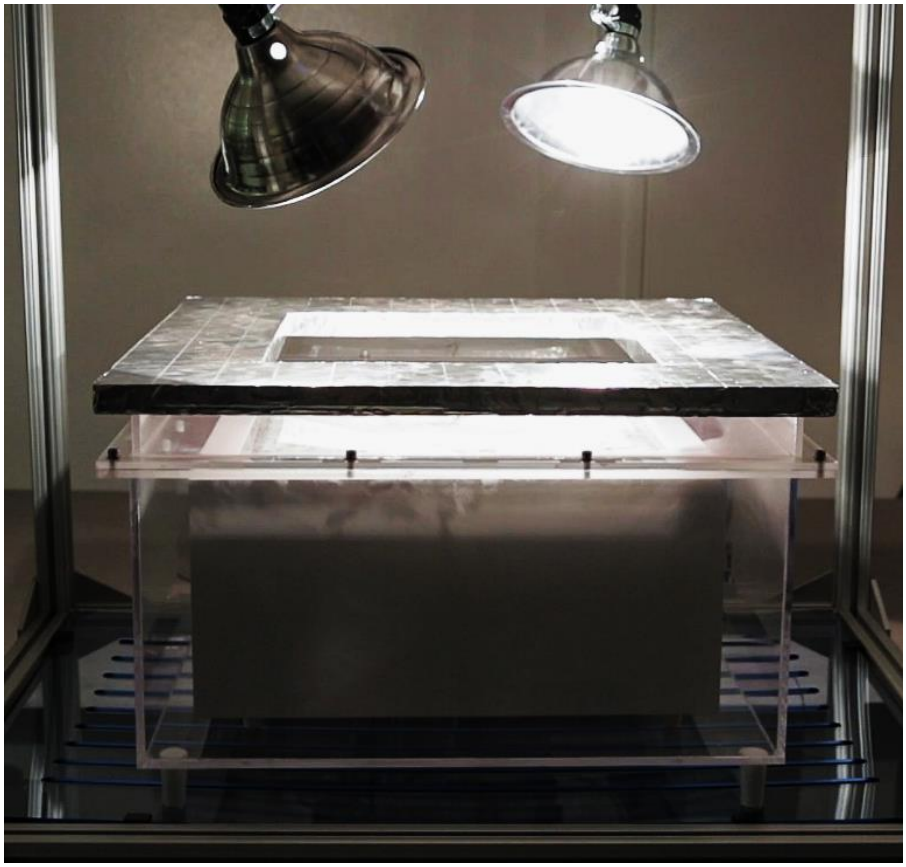

fig. S54. Image of the artificial flux generator in two lamps configuration.

The average hemispherical absorptivity (α) of the sorbents and transmissivity (τ) of the cover for artificial radiation were determined using the following equations

$$\alpha \approx \frac{\int_{285}^{2500} \alpha_{\lambda}(\lambda)\dot{E}_{lab}(\lambda)d\lambda}{\int_{285}^{2500} \dot{E}_{lab}(\lambda)d\lambda} \tag{11}$$

$$\tau \approx \frac{\int_{285}^{2500} \tau_{\lambda}(\lambda)\dot{E}_{lab}(\lambda)d\lambda}{\int_{285}^{2500} \dot{E}_{lab}(\lambda)d\lambda} \tag{12}$$

where $\alpha_{\lambda}(\lambda)$ and $\tau_{\lambda}(\lambda)$, are the spectral directional absorptivity and transmissivity, respectively, and $\dot{E}(\lambda)$ is spectral distribution of solar or artificial radiation (shown in fig. S52). The numerical integration was done using MATLAB R2017a (*29*), and the values calculated for α and τ are listed in the table S3.

table S3. The average hemispherical absorptivity and transmissivity of materials for artificial and solar radiation within the range of 285 to 2500 nm.

Material	Solar radiation	Artificial radiation
Zeolite-13X	α_{solar} = 0.10	α_{lab} = 0.04
MOF-801	α_{solar} = 0.01	α_{lab} = 0.02
MOF-801/G	α_{solar} = 0.56	α_{lab} = 0.62
MOF-303	α_{solar} = 0.01	α_{lab} = 0.03
MOF-303/G	α_{solar} = 0.67	α_{lab} = 0.71
Cover	τ_{solar} = 0.92	τ_{lab} = 0.83

section S9.2. Water production under laboratory conditions

A set of water harvesting experiments was performed on Zeolite 13X, MOF-801/G, MOF-303/G under controlled laboratory conditions. To exclude error originating from humidity remaining in the water sorption unit, the case, and in between the graphite particles, harvesting experiments were conducted with an empty sorbent container and graphite. Table S4 summarizes the amount of sorbent used in the experiment as well as the adsorption/desorption conditions.

table S4. Test conditions for the water harvesting in the laboratory.

# Test	Sorbent	Test conditions
1	no sorbent	adsorption: night conditions (30-50% RH, 18-25°C) desorption: low flux radiation (7.5 h)
2	graphite (0.25 kg)	adsorption: night conditions (30-50% RH, 18-25°C) desorption: low flux radiation (7.5 h)
3	Zeolite 13X (0.5 kg)	adsorption: night conditions (30-50% RH, 18-25°C) desorption: low flux radiation (7.5 h)
4	Zeolite 13X (0.5 kg)	adsorption: night conditions (30-50% RH, 18-25°C) desorption: high flux radiation (7.5 h)
5	MOF-801/G (1.650 kg)	adsorption: night conditions (30-50% RH, 18-25°C) desorption: low flux radiation (7.5 h)
6	MOF-801/G (1.650 kg)	adsorption: night conditions (30-50% RH, 18-25°C) desorption: high flux radiation (7.5 h)
7	MOF-801/G (0.825 kg)	adsorption: night conditions (30-50% RH, 18-25°C) desorption: low flux radiation (7.5 h)
8	MOF-801/G (0.825 kg)	adsorption: night conditions (30-50% RH, 18-25°C) desorption: high flux radiation (7.5 h)
9	MOF-801/G (0.412 kg,)	adsorption: night conditions (30-50% RH, 18-25°C) desorption: low flux radiation (7.5 h)
10	MOF-801/G (0.412 kg)	adsorption: night conditions (30-50% RH, 18-25°C) desorption: high flux radiation (7.5 h)
11	MOF-303/G (0.600 kg)	adsorption: night conditions (30-50% RH, 18-25°C) desorption: low flux radiation (7.5 h)
12	MOF-303/G (0.600 kg)	adsorption: night conditions (30-50% RH, 18-25°C) desorption: high flux radiation (7.5 h)
13	MOF-801/G (0.600 kg)	adsorption: controlled conditions (35% RH, 15°C) desorption: low flux radiation (7.5 h)
14	MOF-303/G (0.600 kg)	adsorption: controlled conditions (35% RH, 15°C) desorption: low flux radiation (7.5 h)

Relative humidity/temperature experimental data for water harvesting under laboratory conditions: The temperature and relative humidity profiles for all laboratory water harvesting cycles are shown in fig. S55-S68. The amount of collected liquid water is given for each experiment. The last 30 minutes of saturation are shown to evaluate the saturation conditions. Low and high fluxes are 558 and 792 W m^{-2}, respectively. The temperature sensors were placed at the surface of the sorbent (sorbent surface), in the sorbent (sorbent interior), at side wall of the case (exterior side wall), at the bottom of the condenser (condenser), and outside (ambient). The ambient dew temperature was estimated from the ambient RH and temperature readings. The relative humidity sensors were placed at the top of the sorbent surface (sorbent surface), at the bottom of the case in the proximity of the condenser (condenser) and outside (ambient).

For experiment 13 and 14 (table S4**)**, the saturation was carried out using an Espec environmental chamber. After the sorbent was taken out of the chamber and transferred to the water sorption unit, the case was sealed and the release process was started immediately.

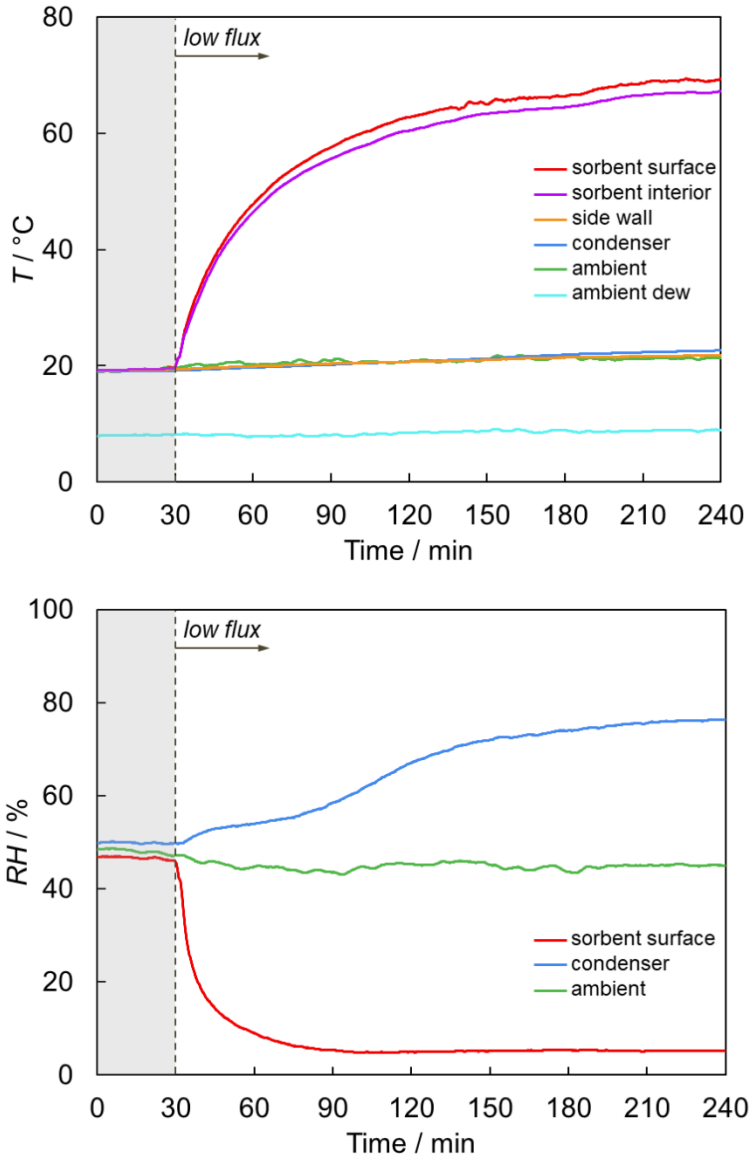

fig. S55. Relative humidity and temperature profiles for empty sorbent container under low flux artificial solar irradiance. The temperature (top) and relative humidity (bottom) profiles during water harvesting without material (i.e. empty sorbent container). Water harvesting was performed under low flux for 7.5 h. No condensation was observed.

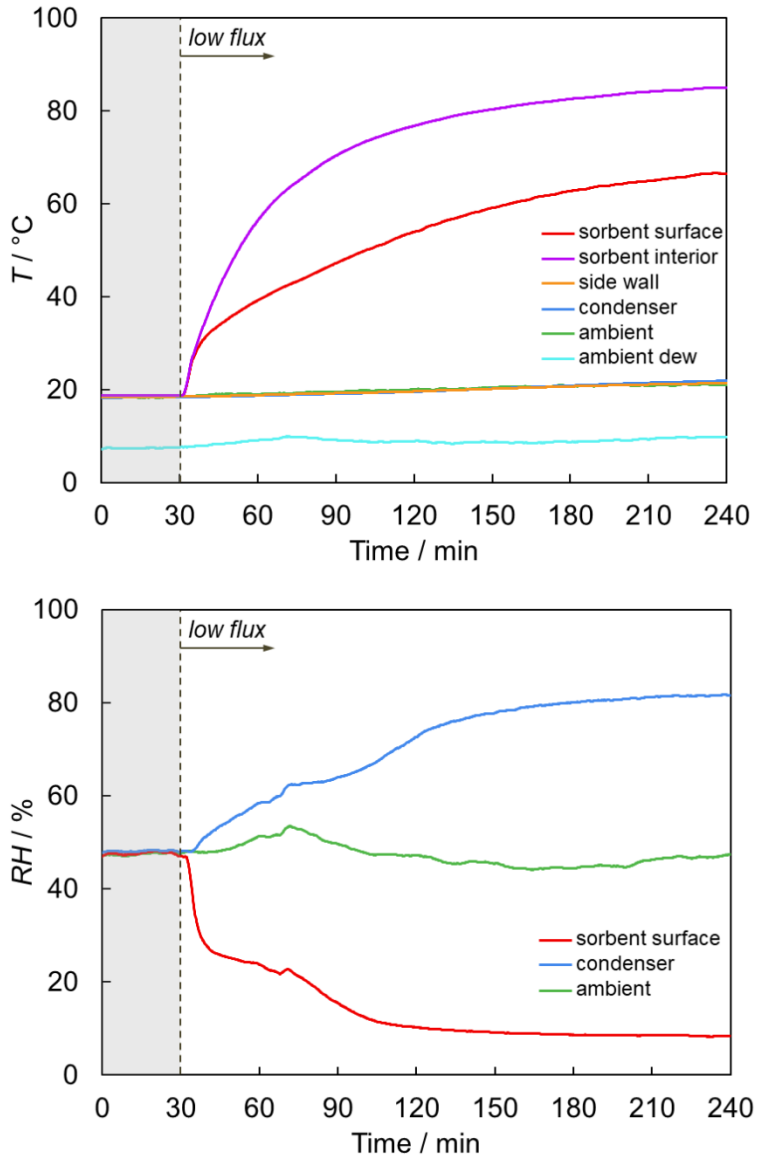

fig. S56. Relative humidity and temperature profiles for 0.25 kg graphite under low flux artificial solar irradiance. The temperature (top) and relative humidity (bottom) profiles during water harvesting using 0.25 kg graphite. Water harvesting was performed under low flux for 7.5 h. A small amount of fog formation was observed.

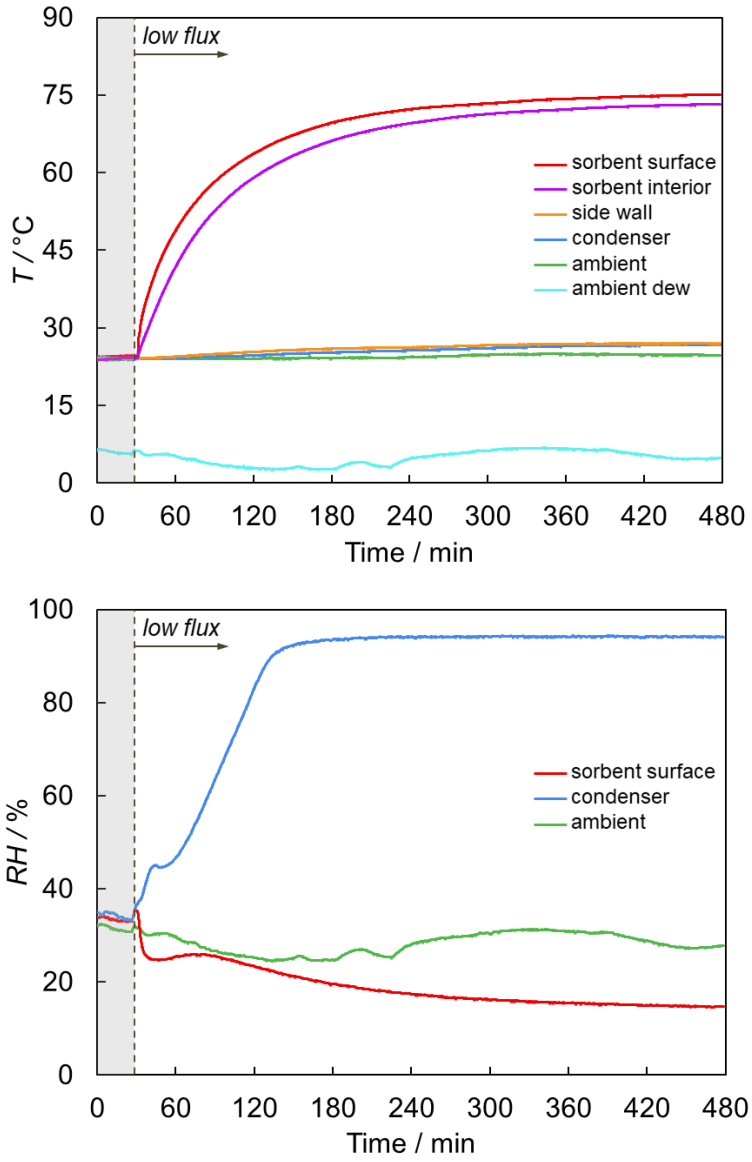

fig. S57. Relative humidity and temperature profiles for 0.5 kg of zeolite 13X under low flux artificial solar irradiance. The temperature (top) and relative humidity (bottom) profiles during water harvesting using 0.5 kg of Zeolite 13X. Water harvesting was performed under low flux for 7.5 h. 6 g of liquid water was collected.

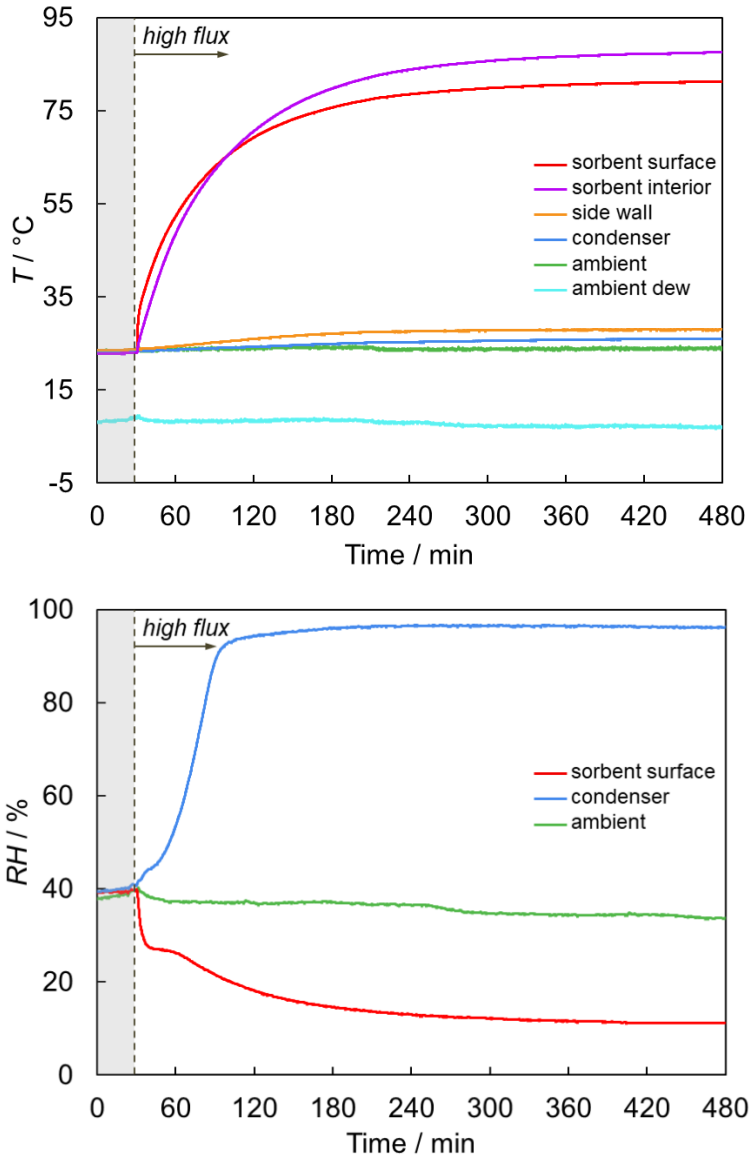

fig. S58. Relative humidity and temperature profiles for 0.5 kg of zeolite 13X under high flux artificial solar irradiance. The temperature (top) and relative humidity (bottom) profiles during water harvesting using 0.5 kg of Zeolite 13X. Water harvesting was performed under high flux for 7.5 h. 16 g of liquid water was collected.

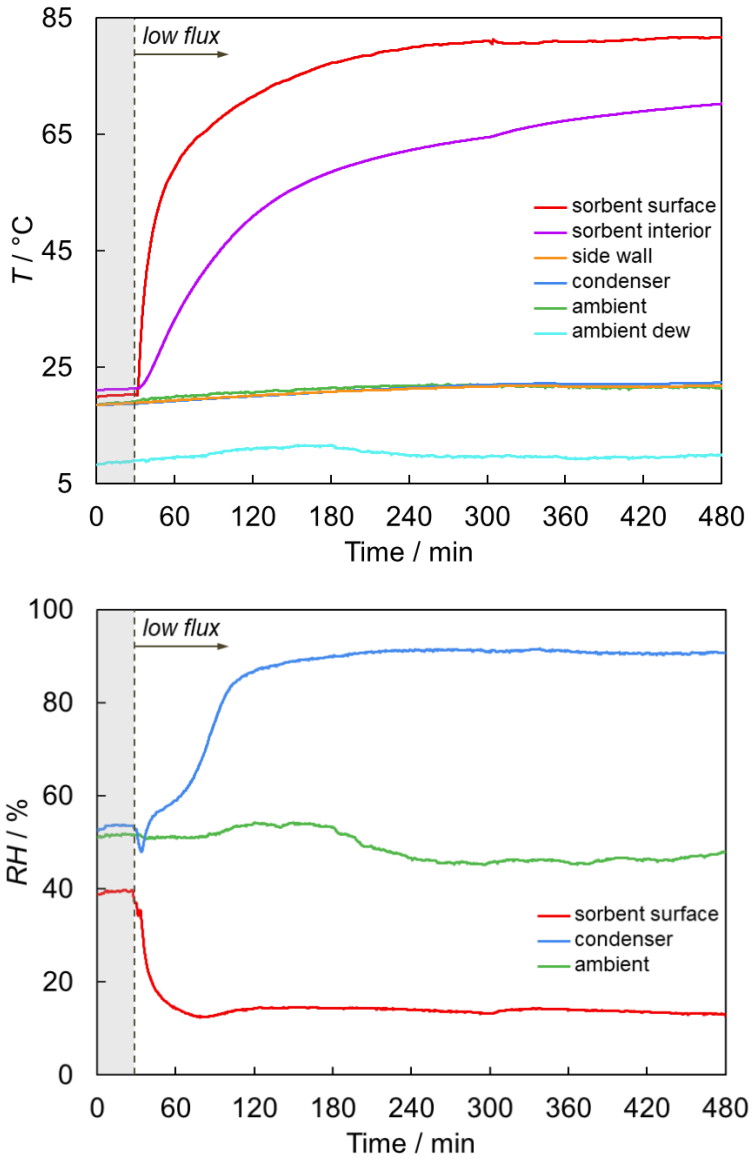

fig. S59. Relative humidity and temperature profiles for 1.65 kg of MOF-801/G under low flux artificial solar irradiance. The temperature (top) and relative humidity (bottom) profiles during water harvesting using 1.65 kg of MOF-801/G. Water harvesting was performed under low flux for 7.5 h. 25 g of liquid water was collected.

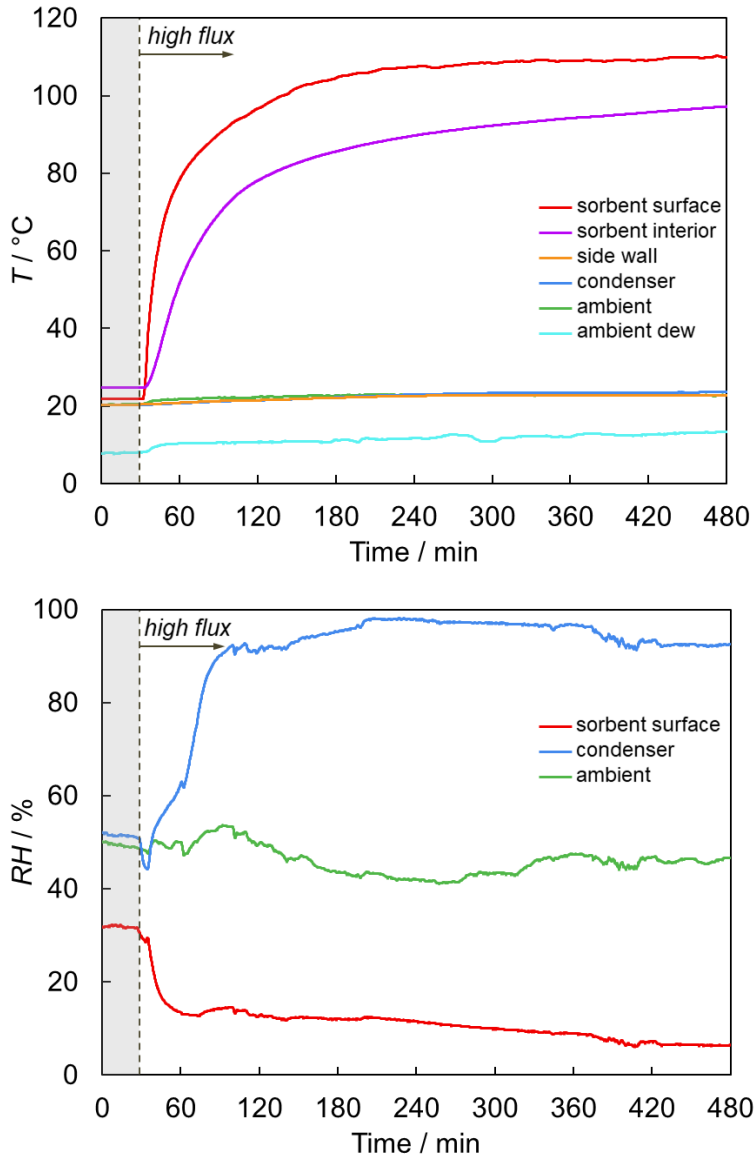

fig. S60. Relative humidity and temperature profiles for 1.65 kg of MOF-801/G under high flux artificial solar irradiance. The temperature (top) and relative humidity (bottom) profiles during water harvesting using 1.65 kg of MOF-801/G. Water harvesting was performed under high flux for 7.5 h. 63 g of liquid water was collected.

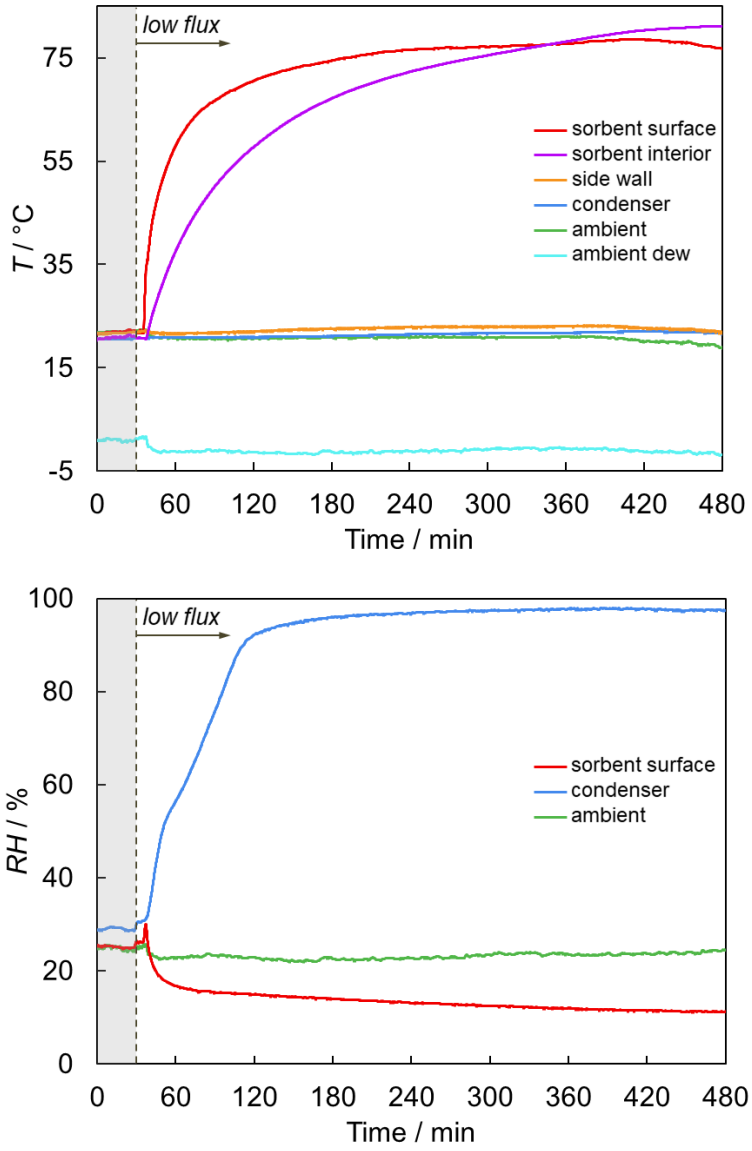

fig. S61. Relative humidity and temperature profiles for 0.825 kg of MOF-801/G under low flux artificial solar irradiance. The temperature (top) and relative humidity (bottom) profiles during water harvesting using 0.825 kg of MOF-801/G. Water harvesting was performed under low flux for 7.5 h. 37 g of liquid water was collected.

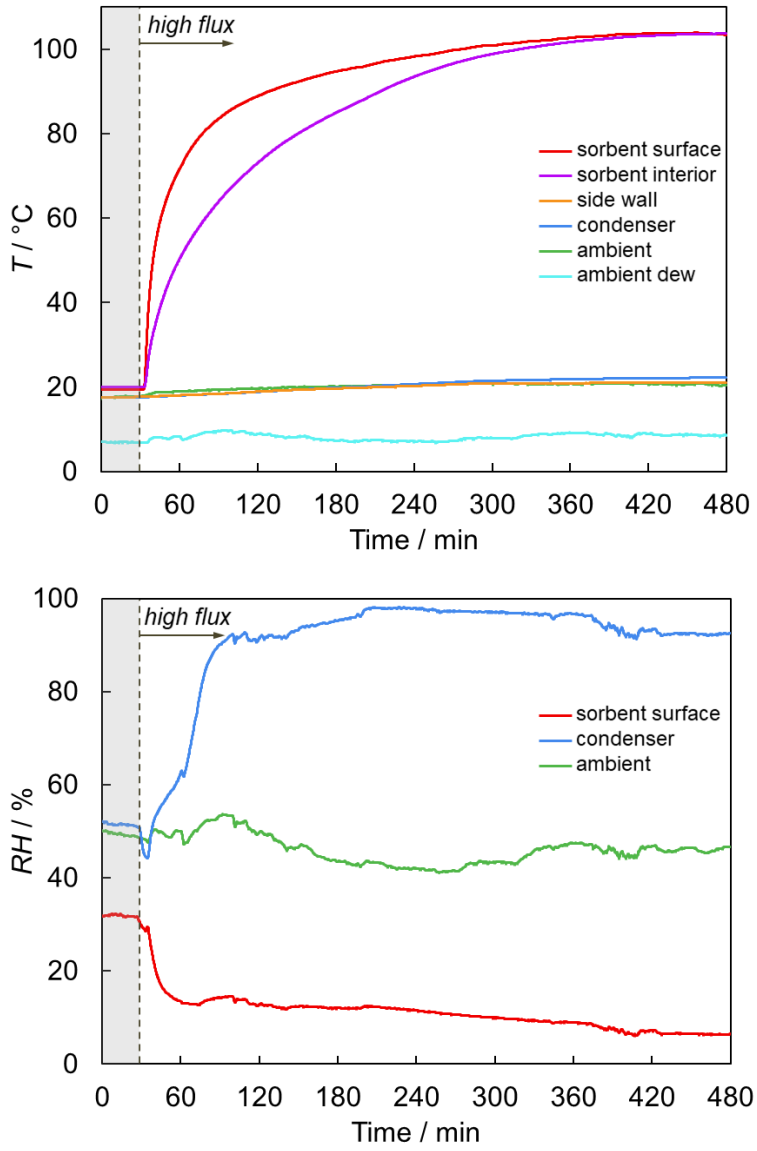

fig. S62. Relative humidity and temperature profiles for 0.825 kg of MOF-801/G under high flux artificial solar irradiance. The temperature (top) and relative humidity (bottom) profiles during water harvesting using 0.825 kg of MOF-801/G. Water harvesting was performed under high flux for 7.5 h. 78 g of liquid water was collected.

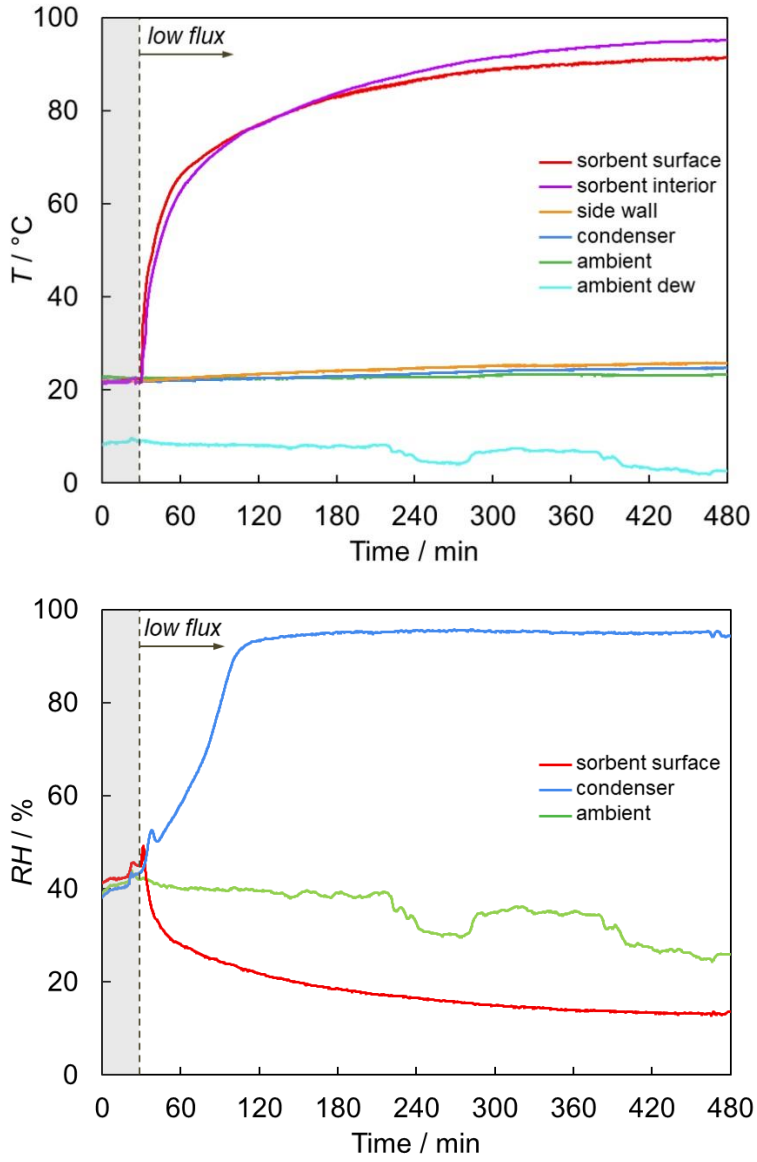

fig. S63. Relative humidity and temperature profiles for 0.412 kg of MOF-801/G under low flux artificial solar irradiance. The temperature (top) and relative humidity (bottom) profiles during water harvesting using 0.412 kg of MOF-801/G. Water harvesting was performed under low flux for 7.5 h. 26 g of liquid water was collected.

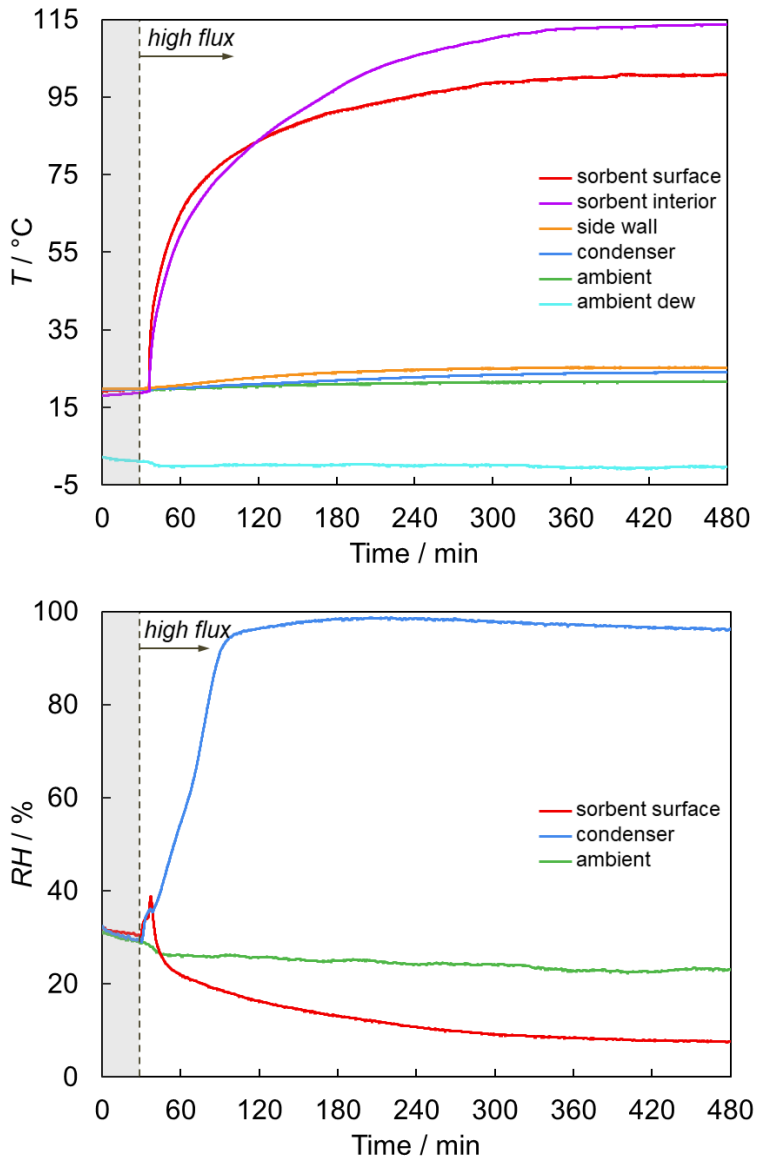

fig. S64. Relative humidity and temperature profiles for 0.412 kg of MOF-801/G under high flux artificial solar irradiance. The temperature (top) and relative humidity (bottom) profiles during water harvesting using 0.412 kg of MOF-801/G. Water harvesting was performed under high flux for 7.5 h. 36 g of liquid water was collected.

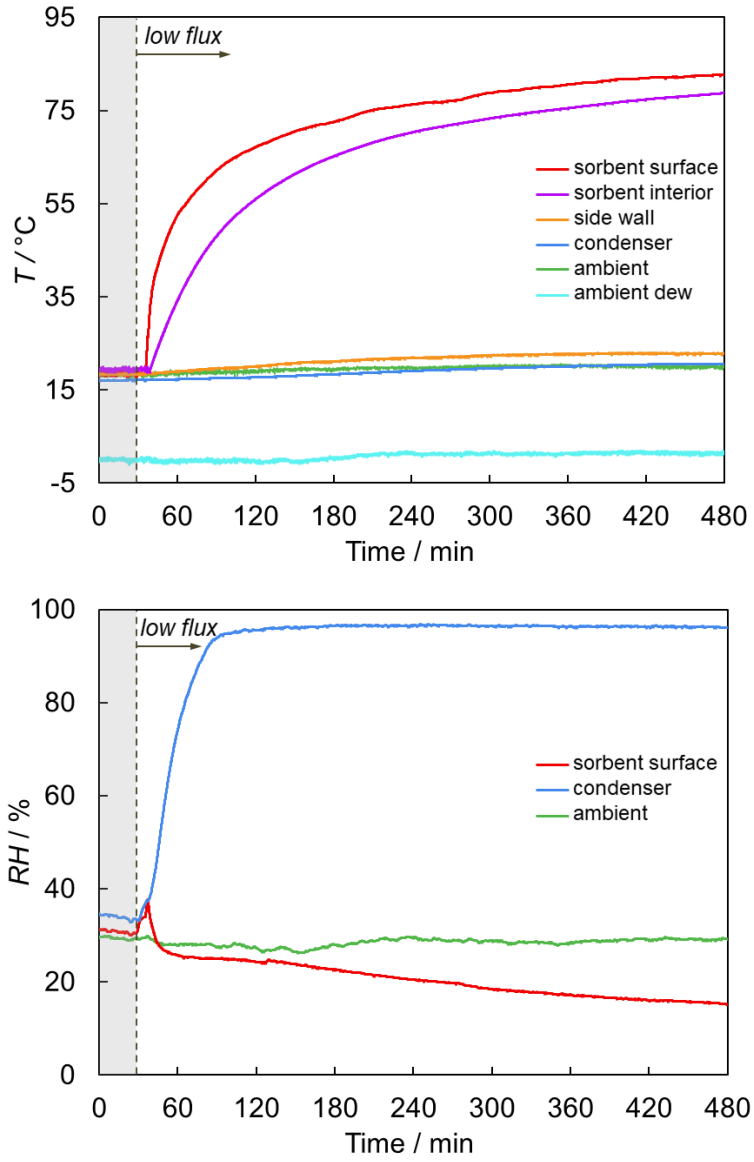

fig. S65. Relative humidity and temperature profiles for 0.600 kg of MOF-303/G under low flux artificial solar irradiance. The temperature (top) and relative humidity (bottom) profiles during water harvesting using 0.600 kg of MOF-303/G. Water harvesting was performed under low flux for 7.5 h. 60 g of liquid water was collected.

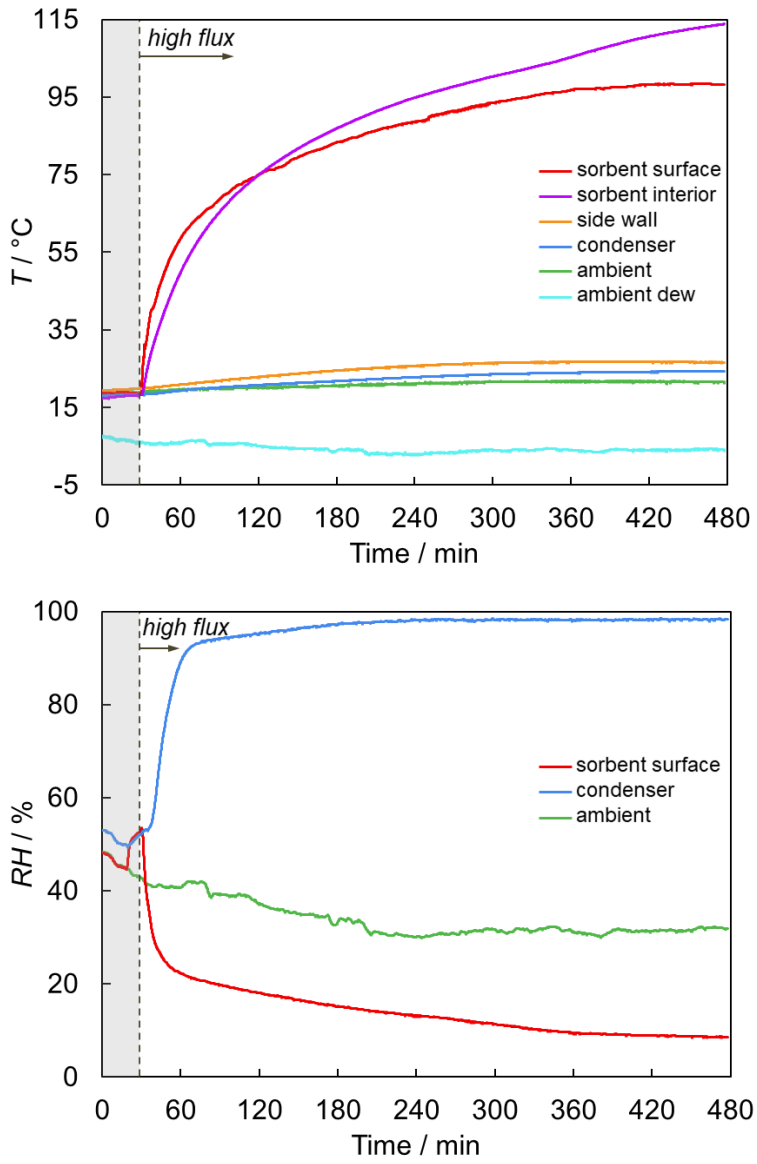

fig. S66. Relative humidity and temperature profiles for 0.600 kg of MOF-303/G under high flux artificial solar irradiance. The temperature (top) and relative humidity (bottom) profiles during water harvesting using 0.600 kg of MOF-303/G. Water harvesting was performed under high flux for 7.5 h. 105 g of liquid water was collected.

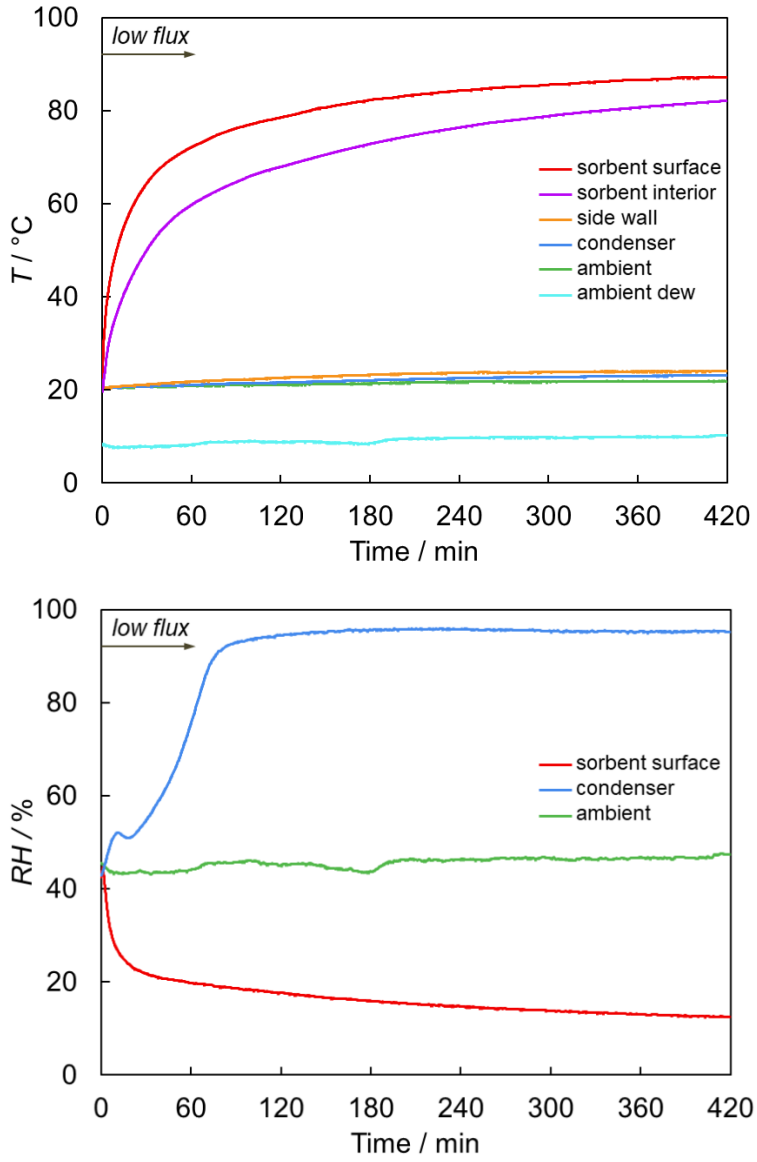

fig. S67. Relative humidity and temperature profiles for 0.600 kg of MOF-801/G under low flux artificial solar irradiance and controlled saturation conditions. The temperature (top) and relative humidity (bottom) profiles during water harvesting using 0.600 kg of MOF-801/G. Saturation was performed in an environmental chamber at 35% RH and 15°C for 5 days. Water harvesting was performed under low flux for 7.5 h. 28 g of liquid water was collected.

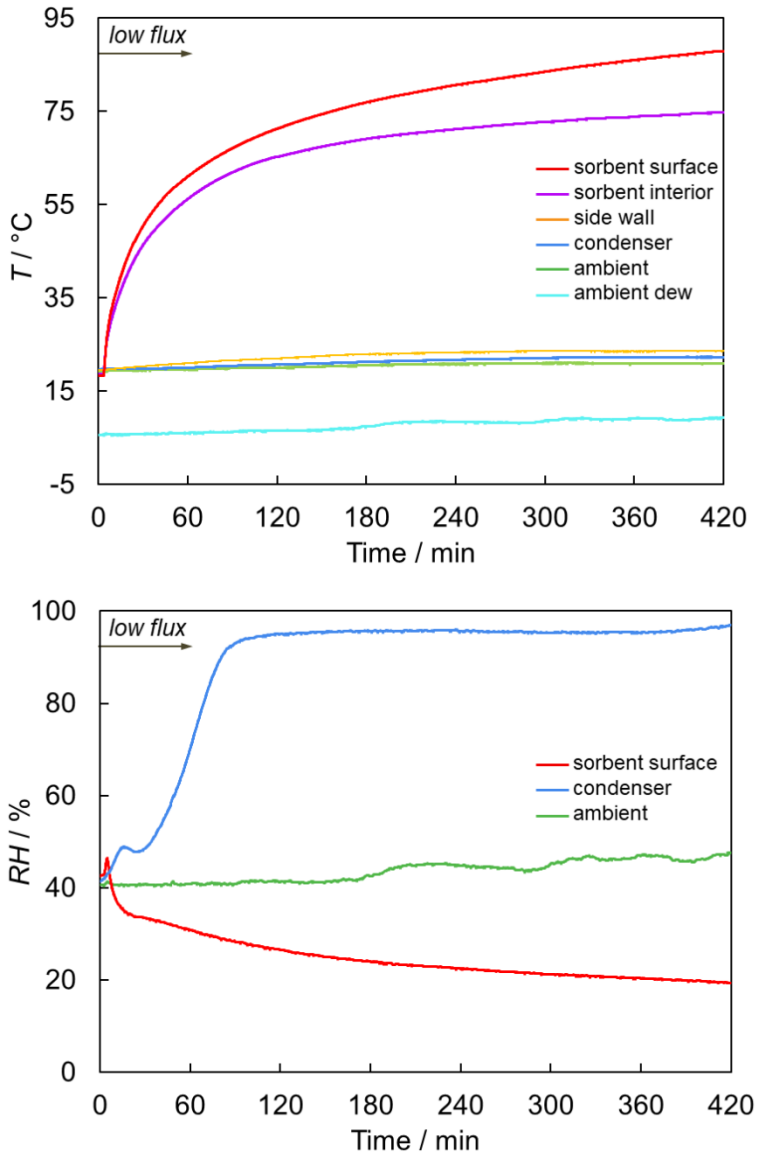

fig. S68. Relative humidity and temperature profiles for 0.600 kg of MOF-303/G under low flux artificial solar irradiance and controlled saturation conditions. The temperature (top) and relative humidity (bottom) profiles during water harvesting using 0.600 kg of MOF-303/G. Saturation was performed in an environmental chamber at 35% RH and 15°C for 5 days. Water harvesting was performed under low flux for 7.5 h. 60 g of liquid water was collected.

section S9.3. Evaluation of water harvesting cycle performance

The capture capacity ω_{cap} was estimated from the temperature and RH profiles for last 30 minutes of saturation. Final capacity ω_{fin} was estimated from the temperature and RH profiles assuming that the sorbent and air are in equilibrium with each other i.e. the change in RH and temperature values are smaller than their uncertainties for last 30 minutes of the harvesting experiment before liquid water collection. The amount of released water per mass of sorbent, ω_{rel}, is the difference between ω_{cap} and ω_{fin}. The capture, release, and water harvesting cycle efficiencies as well as the productivity are shown in table S5.

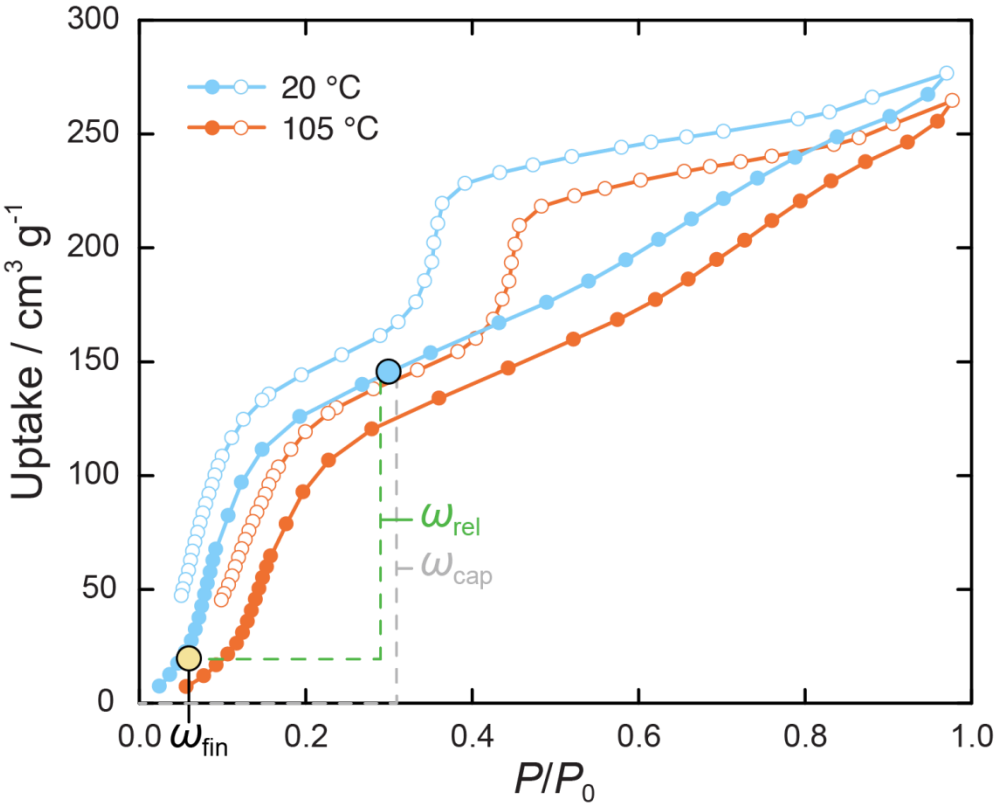

fig. S69. Water sorption isotherms for MOF-801/G. Blue and yellow points indicate the conditions for saturation and release for 1.65 kg of MOF-801/G at high flux during water harvesting experiment #6 (table S4).

table S5. The performance parameters for water production under laboratory conditions.

Sorbent	Test condition	Collected water (g)	ω_{cap}	ω_{rel}	η_R (%)	η_C (%)	η_{WHC} (%)	P (g.kg^{-1})
No sorbent (empty pan)	Low flux	0	–	–	–	–	–	–
Graphite (0.25 kg)	Low flux	0	–	–	–	–	–	–
Zeolite 13X (0.5 kg)	Low flux	6	0.31	0.01	4	100	4	12
Zeolite 13X (0.5 kg)	High flux	16	0.32	0.03	10	100	10	32
MOF801/G (1.650 kg)	Low flux	25	0.13	0.05	39	30	12	15
MOF801/G (1.650 kg)	High flux	65	0.12	0.09	76	43	33	39
MOF801/G (0.825 kg)	Low flux	37	0.11	0.05	44	93	41	45
MOF801/G (0.825 kg)	High flux	78	0.12	0.10	86	92	79	95
MOF801/G (0.412 kg)	Low flux	26	0.13	0.64	49	99	48	63
MOF801/G (0.412 kg)	High flux	36	0.12	0.10	83	90	75	87
MOF303/G (0.600 kg)	Low flux	60	0.25	0.15	57	68	39	100
MOF303/G (0.600 kg)	High flux	105	0.27	0.22	81	79	65	175
MOF801/G (0.600 kg)	Low flux controlled	28	0.12	0.05	42	88	37	47
MOF303/G (0.600 kg)	Low flux controlled	60	0.27	0.15	55	67	37	100

section S9.4. Design considerations for water release

In this section, a theoretical approach to estimate the energy requirements for release of water from the MOF and subsequent condensation is discussed.

Figure S70 shows the incident radiation flux $\left(\dot{E}\right)$, a portion of it passing through the transparent cover, which is subsequently absorbed by a unit mass of MOF ($\dot{q}_{abs}$). A fraction of this energy is lost in the forms of the radiative heat loss ($\dot{q}_{radiation}$) and convective heat loss ($\dot{q}_{convection}$). The thermal radiation emitted by cover was neglected and it is assumed that the conducive heat loss is minimized by using extruded polystyrene foam with low thermal conductivity (0.027 W m^{-1} K^{-1}).

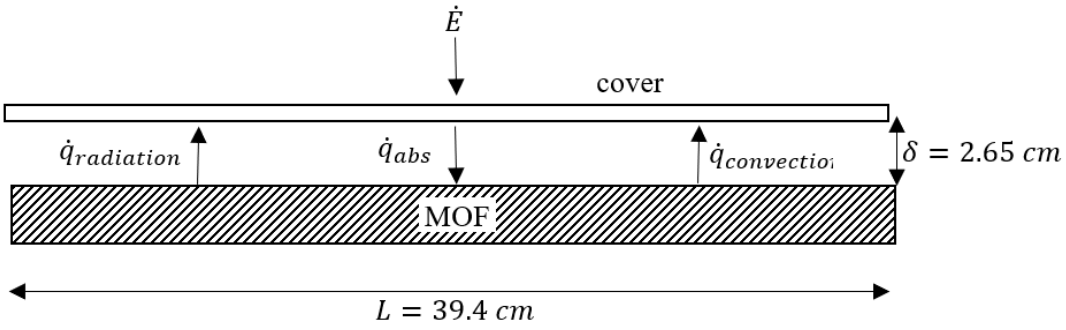

fig. S70. Schematic of energy flow on the top surface of the water sorption unit.

Considering the uniform temperature distribution within the MOF $\left(Bi = \frac{hL_c}{k} < 0.1\right)$ at any given time, the energy balance for a control volume including the MOF is

$$\rho_{eff} c_{p,eff} \frac{dT}{dt} - \rho_{MOF} q_{st} \frac{d\omega}{dt} = \left(\frac{A}{V_{bed}}\right)\left(\dot{q}_{abs} - \dot{q}_{radiation} - \dot{q}_{convection}\right) \tag{13}$$

Time-dependent effective properties of the sorbent packing are defined by the following equations

$$\rho_{eff} = \rho_{MOF}\left(1-\varepsilon\right)\left(1+\omega\right) + \rho_{air}\varepsilon \tag{14}$$

and

$$c_{p,eff} = \frac{\rho_{MOF,dry}\left(1-\varepsilon\right)\left(c_{p,MOF,dry} + \omega c_{p,water}\right) + \rho_{air} c_{p,air}\varepsilon}{\rho_{eff}} \tag{15}$$

where ε, c_p, ρ are the packing porosity (excluding the MOF internal pore volume), heat capacity, and density, respectively. Replacing the effective properties in equation (13) with equations (14) and (15) and integrating equation (13) over the release period results in

$$\begin{aligned} &\int_{T_{cap}}^{T_{rel}} \left(\rho_{MOF,dry}\left(1-\varepsilon\right)\left(c_{p,MOF,dry} + \omega c_{p,water}\right) + \rho_{air} c_{p,air}\varepsilon\right) dT \\ &\quad - \int_{\omega_{cap}}^{\omega_{rel}} \rho_{MOF} q_{st} d\omega = \left(\frac{A}{V_{bed}}\right) \int_{sunrise}^{sunset} \left(\dot{q}_{abs} - \dot{q}_{radiation} - \dot{q}_{convection}\right) dt \end{aligned} \tag{16}$$

Assuming that the entire amount of captured water is desorbed during the release process at the release temperature, the released water vapor is in thermal equilibrium with the MOF, and assuming that the variations of density and heat capacity with temperature are small, equation (16) becomes

$$\begin{aligned} &\left[\left(c_{p,MOF,dry} + \omega_{cap} c_{p,water}\right)\left(1-\varepsilon\right) + \left(\rho_{air} \Big/ \rho_{MOF,dry}\right) c_{p,air}\varepsilon\right]\left(T_{rel} - T_{cap}\right) \\ &+ \omega_{cap} q_{st} = \left(\frac{1}{\rho_{MOF,dry}}\right)\left(\frac{A}{V_{bed}}\right) \int_{sunrise}^{sunset} \left(\dot{q}_{abs} - \dot{q}_{radiation} - \dot{q}_{convection}\right) dt \end{aligned} \tag{17}$$

The total received energy per mass of MOF is defined

$$q_H = \left(\frac{1}{\rho_{MOF,dry}}\right)\left(\frac{A}{V_{bed}}\right)\int_{sunrise}^{sunset}\left(\dot{q}_{abs} - \dot{q}_{radiation} - \dot{q}_{convection}\right)dt \qquad (18)$$

The total sensible energy is defined as the amount of energy per unit mass of MOF spent to increase the temperature of MOF from the capture temperature to the release temperature as

$$q_{sensible} = \left[\left(c_{p,MOF,dry} + \omega_{cap}c_{p,water}\right)\left(1-\varepsilon\right) + \left(\frac{\rho_{air}}{\rho_{MOF,dry}}\right)c_{p,air}\varepsilon\right]\left(T_{rel} - T_{cap}\right) \qquad (19)$$

The total latent energy is defined as the amount of energy per unit mass of MOF spent to desorb the entire amount of captured water from the MOF as

$$q_{latent} = \omega_{cap}q_{st} \qquad (20)$$

$q_{sensible}$ and q_{latent} considerations: In this section, a comparison between the $q_{sensible}$ and q_{latent} for the designed water harvester is provided based on our preliminary laboratory data on MOF-801/G. The RH of 35% at 25°C was considered for the water capture process which results in ω_{cap} = 0.14. The average value of $q_{st,801}$ = 3000 kJ kg^{-1} was determined from the sorption isotherms resulting in q_{latent} = 420 kJ kg^{-1}. With $c_{p,801}$ = 760 J kg^{-1} K^{-1} and $\rho_{p,801}$ = 1400 kg m^{-3} (*15*), $c_{p,G}$ = 760 J kg^{-1} K^{-1} and 2150 kg m^{-3} (*30*), then the density and heat capacity of the mixture are $\rho_{p,801/G}$ = 1584 kg m^{-3} and $c_{p,801/G}$ = 743 J kg^{-1} K^{-1}, respectively. The values of $q_{sensible}$ and $q_{sensible}/q_{latent}$ for different $\Delta T_{WH} = T_{rel} - T_{cap}$ are shown in the fig. S71 where the water and air properties were calculated at the mean release and capture temperatures. The results indicate that the $q_{sensible} << q_{latent}$ during the release process, therefore, almost all the incident energy is spent on overcoming the MOF-water interactions.

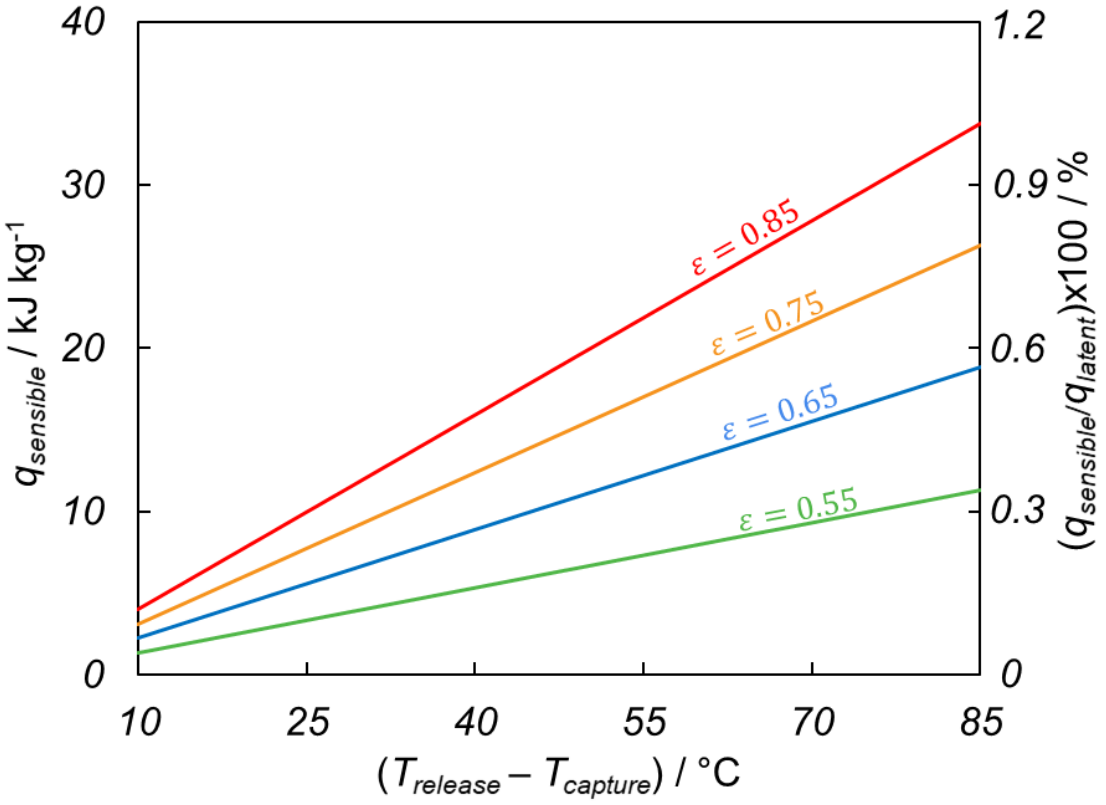

fig. S71. Variations of $q_{sensible}$ with the release and capture temperature for four values of packing porosities of 0.85, 0.75, 0.65, and 0.55. $q_{sensible}$ was calculated for a capture temperature of 20°C. The ratio of sensible to latent energy reveals that the majority of the energy is spent on breaking the MOF-water interactions, rather than increasing the temperature of the MOF during the release process.

$\dot{q}_H$ considerations: To determine $\dot{q}_H$, it is required to quantify $\dot{q}_{abs}$, $\dot{q}_{radiation}$, and $\dot{q}_{convection}$. For the laboratory experiment with artificial flux

$$\dot{q}_{abs} = \alpha_{MOF,lamp}\tau_{cover,lamp}\dot{E}_{lamp} \quad (21)$$

where α_λ and τ_λ are absorptivity of the MOF-801/G and transmissivity of the cover, respectively, and $\dot{E}_{lamp}$ is the measured incident radiation flux on the surface of the cover. With the average constant low and high fluxes $\dot{E}_{lamp}$ = 558 and 792 W m^{-2}, and the values of $\alpha_{MOF,lamp}$ and $\tau_{cover,lamp}$ taken from section 7.3, the total radiant flux received by a unit mass of MOF-801/G was determined and listed in table S6.

table S6. Total flux received by different sorbents for the laboratory experiment using low and high fluxes.

Sorbent	$\dot{q}_{abs}$ / W m^{-2}	
	Low flux	High flux
Zeolite 13X	18	28
MOF-801/G	277	430
MOF-303/G	317	492

The radiative heat loss from the sorbent surface can be determined by

$$\dot{q}_{radiation} = \varepsilon_m \sigma T_{MOF}^4 \tag{22}$$

where $\sigma = 5.670 \times 10^{-8}$ / W m^{-3} K^4 is the Stefan-Boltzmann constant and ε_m is the hemispherical emissivity of the sorbent. Variations of $\dot{q}_{radiation}$ with the temperature and emissivity are shown in fig. S72. It can be observed that for the range of temperature required for the release of water from MOF ($T_{release}$ < 80°C), the heat loss due to radiation is negligible (< 4 W m^{-2}) compared to the received flux (~ 250-500 W m^{-2}), even if the MOF is considered a blackbody emitter $(\varepsilon = 1)$. In the calculations of incident flux, the maximum value of 4 W m^{-2} was considered for the radiative heat loss.

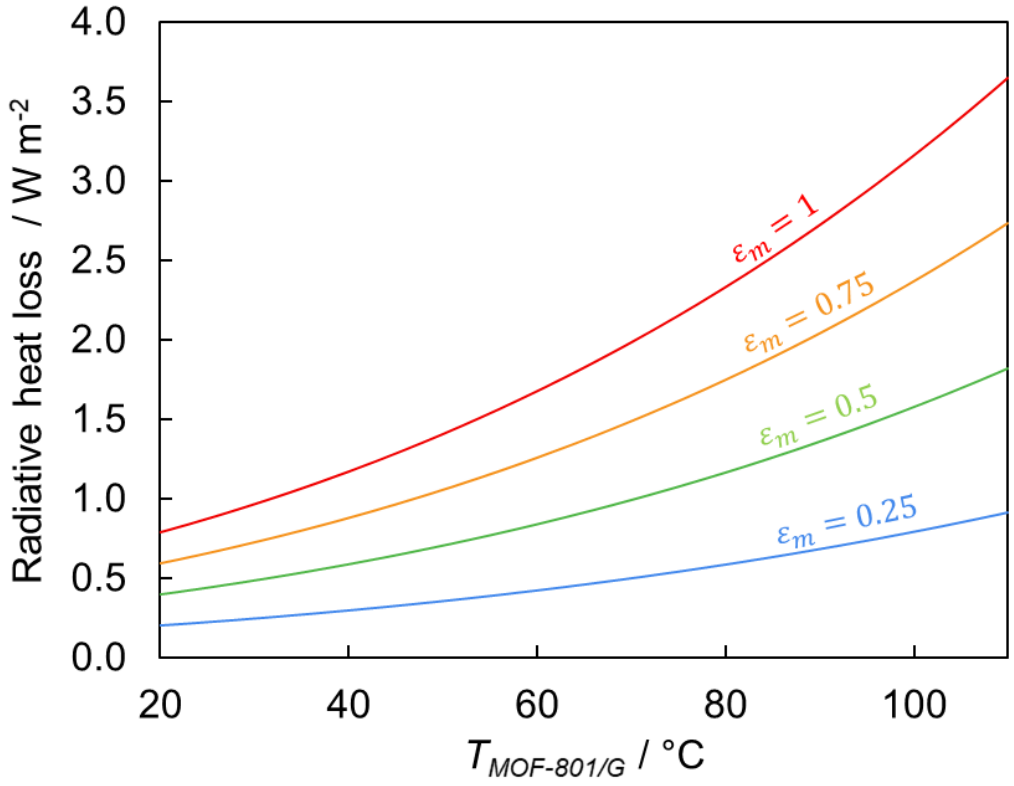

fig. S72. Variations of radiative heat loss with MOF-801/G temperature for different values of emissivity.

The heat loss from the MOF surface to the cover due to convection was determined by

$$\dot{q}_{convection} = \bar{h}\left(T_{MOF} - T_{cover}\right) \tag{23}$$

where $\bar{h}$ is the average convective heat transfer coefficient over the length of the MOF surface and T_{cover} is the surface temperature of the cover. The Rayleigh number was calculated using the following equation

$$Ra_L = \frac{g\rho\beta\left(T_{MOF} - T_{cover}\right)\delta^3}{\alpha_T \mu} \tag{24}$$

where β, α_T, and μ are the volumetric thermal expansion coefficient, thermal diffusivity, and dynamic viscosity of the air, respectively, and g is the gravitational acceleration. To determine the value of β, α_T, and μ, air was considered as an ideal gas and the following relations and correlations were used

$$\rho = \frac{P}{RT} \tag{25}$$

$$\beta = \frac{1}{T} \tag{26}$$

$$\mu = \mu_{ref}\left(\frac{T}{T_{ref}}\right)^{3/2}\left(\frac{T_{ref} + 110.4}{T + 110.4}\right) \tag{27}$$

where $\mu_{ref} = 1.8205\times10^{-5}\ \text{kg m}^{-1}\text{s}^{-1}$ at $T_{ref} = 293.15\ \text{K}$, and

$$c_p\left[\text{kJ kg}^{-1}\ \text{K}^{-1}\right] = 1.05 - 0.365\left(\frac{T}{1000}\right) + 0.85\left(\frac{T}{1000}\right)^2 - 0.39\left(\frac{T}{1000}\right)^3 \tag{28}$$

$$k\left[\text{W m}^{-1}\ \text{K}^{-1}\right] = 10^{-4}\times\left[1.52\times10^{-7}T^3 - 4.86\times10^{-4}T^2 + 1.02T - 3.93\right] \tag{29}$$

and

$$\alpha_T = \frac{k}{\rho c_p} \tag{30}$$

The Rayleigh number was estimated by taking the temporal measurement of the temperature of the MOF and the inner surface of the cover under low flux radiation. The temperature profile and instantaneous value of *Ra* are shown in fig. S73.

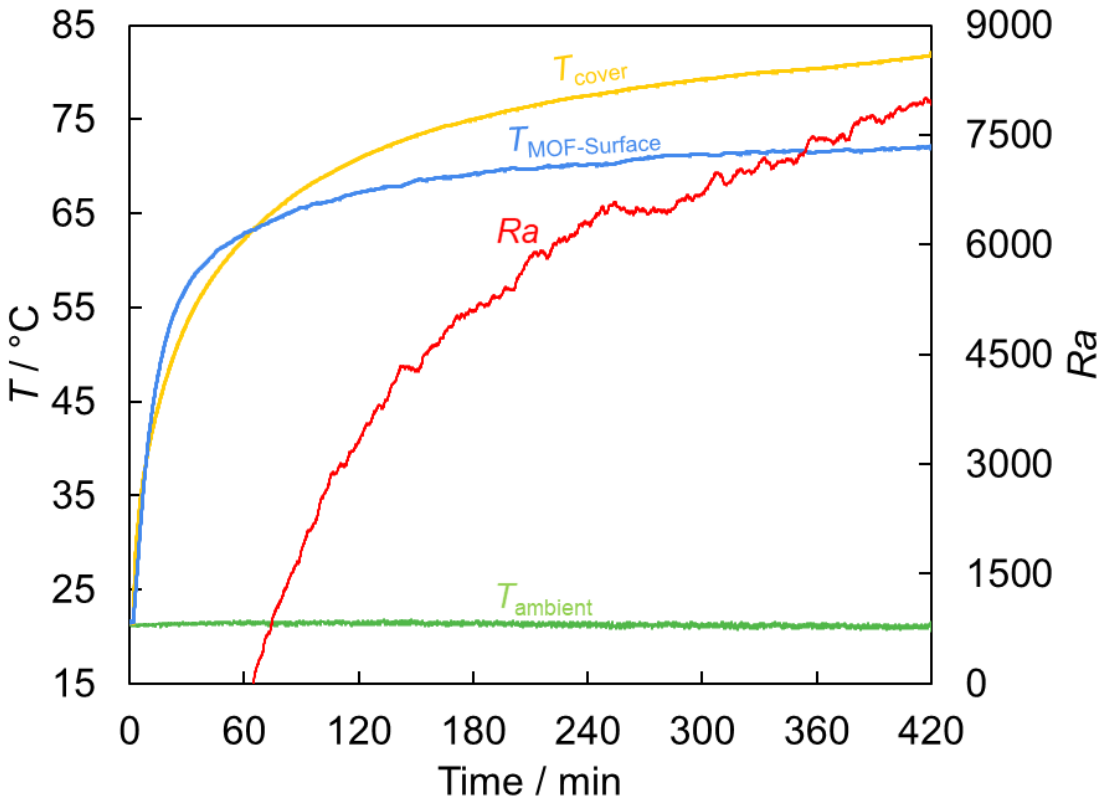

fig. S73. Variations of the temperature of MOF-801/G and the cover. Increase in the Rayleigh number is observed due to the increase in temperature difference. During the first 60 minutes, the cover temperature was higher than that of the MOF with no heat loss.

For $\delta/L > 12$ ($\delta/L = 14.2$ in the current design), the following correlation (*31*) was used to determine the Nusselt number (*Nu*)

$$\overline{Nu} = \begin{cases} 1.44\left(1-\frac{1708}{Ra}\right)+\left(\frac{Ra}{5830}\right)^{\frac{1}{3}} & 1708 < Ra <\sim 10000 \\ 1 & Ra < 1708 \end{cases} \quad (31)$$

where the critical Rayleigh number ($Ra_c = 1708$) determines whether buoyancy forces can overcome the resistance imposed by the viscous forces or not. With the known $\overline{Nu}$, $\bar{h}$ as a function of time was found using

$$\bar{h} = \frac{k\overline{Nu}}{\delta} \quad (32)$$

The total energy absorbed by MOF-801/G for the case of low flux is

$$q_{abs} = \int_{t=0}^{t=end} \dot{q}_{abs} dt = 277 W\, m^{-2} \times 7.5 h \times 3600 s\, h^{-1} = 7479 kJ\, m^{-2} \quad (33)$$

The radiative heat loss from the sorbent surface was determined by

$$q_{radiation} = \int_{t=0}^{t=end} \dot{q}_{radiation} dt = 4 W\, m^{-2} \times 7.5 h \times 3600 s\, h^{-1} = 108 kJ\, m^{-2} \quad (34)$$

Total heat loss per unit area during the entire release cycle was found by numerical integration of the measured data and calculated $\bar{h}$ using MATLAB R2017a

$$q_{convection} = \int_{t=0}^{t=end} \bar{h}\left(T_{MOF} - T_{cover}\right) dt = 3.4 kJ\, m^{-2} \quad (35)$$

Therefore, the total radiative heat loss and the total convective heat loss from the MOF surface are less than 1.5% and 0.05%, respectively. This would result in the total heat loss of less than 1.6%.

The total energy required for the release of water (q_H) was plotted versus the amount of MOF-801/G with and without the heat losses for and exposed surface of 0.155 m^2 (see fig. S74).

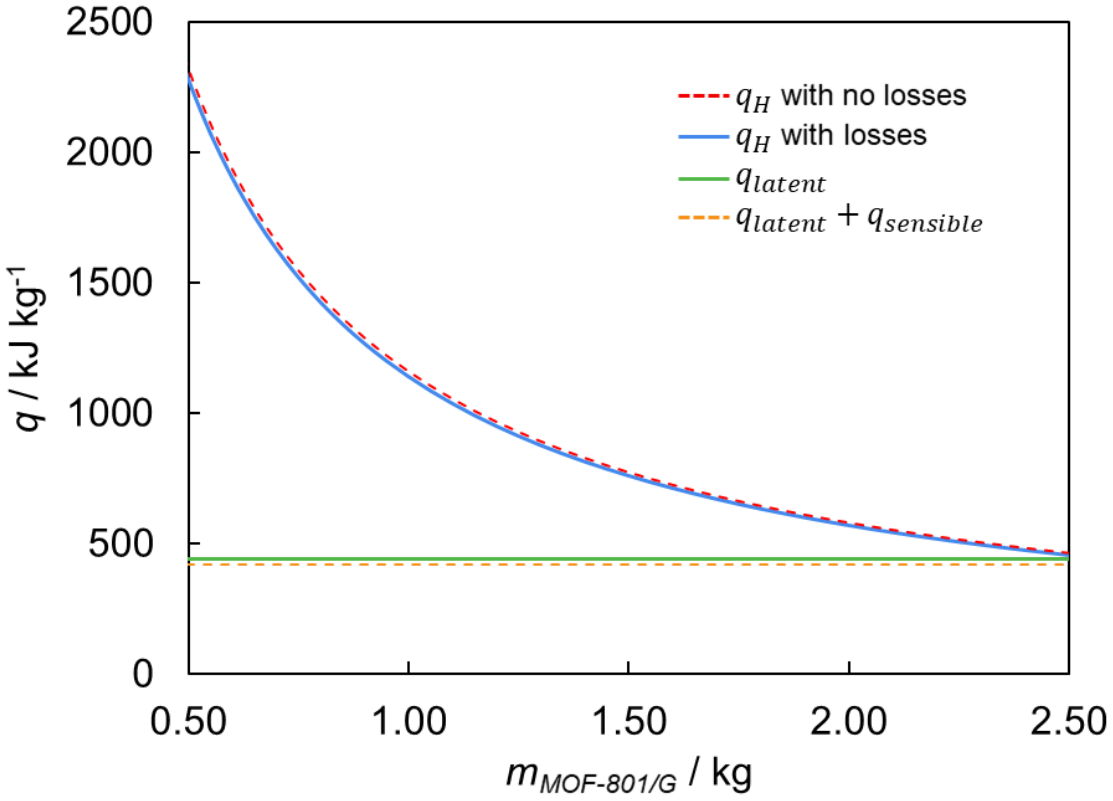

fig. S74. Comparison of q_H (with and without heat losses) and the amount of MOF-801/G to the latent and sensible energy per kilogram of MOF-801/G.

In addition, the total energy required to heat up the MOF and release the captured water $(q_{latent} + q_{sensible})$ is also plotted and compared to q_{latent}. The results reveal that up to 2.5 kg of MOF-801/G can be used in this water harvester; below this mass, the incident radiant energy is sufficient to fully release the captured water from the MOF. It should be noted that the same result is achieved by considering no energy losses from the MOF to the surroundings and neglecting the sensible energy. This eliminates the complication in the calculation and allows a simple criterion to be defined

$$q_H \geq q_{latent} \tag{36}$$

or

$$\left(\frac{1}{\rho_{MOF,dry}}\right)\left(\frac{A}{V_{bed}}\right)\int_{sunrise}^{sunset}\left(\dot{q}_{abs}\right)dt \geq \omega_{cap} q_{st} \tag{37}$$

section S9.5. Design considerations for water condensation

In this section, a theoretical approach to estimate the energy requirements for condensation of water released from the MOF is discussed.

$\dot{q}_C$ **considerations:** The energy required for condensation of water vapor is used to decrease the temperature of the released water vapor ($q_{sensible}$), and liquefy water vapor (q_{latent}) with a portion of it being lost to the surroundings. Thus, the conservation of energy within the condenser over the condensation period is

$$\begin{aligned} q_{c,sensible} + q_{c,latent} + q_{c,loss} = \\ \omega_{rel} c_{p,wv}\left(T_{wv} - T_{dew}\right) + \frac{m_{air}}{m_{MOF}} c_{p,a}\left(T_a - T_{dew}\right) + \omega_{rel} h_{fg} + q_{c,loss} \end{aligned} \tag{38}$$

where T_{wv}, T_a, and T_{dew} are the temperature of the water vapor, dry air, and dew temperature, respectively. $c_{p,wv}$ and $c_{p,a}$ are the heat capacity of water vapor and air, respectively. Considering the heat loss to be negligible, thermal equilibrium between the water vapor and dry air ($T_a = T_w$), maximum possible water release, and subsequent condensation of the released water ($\omega_{rel} = \omega_{cap}$), then

$$q_{c,sensible} + q_{c,latent} = \left(T_a - T_{dew}\right)\left(\omega_{cap} c_{p,w} + \frac{m_{air}}{m_{MOF}} c_{p,a}\right) + \omega_{cap} h_{fg} \tag{39}$$

In the case that the condensation process relies solely on natural cooling, the cooling energy can be estimated as follows

$$q_c = \int_{sunrise}^{sunset} \dot{q}_c(t)\,dt = A_c \int_{sunrise}^{sunset} \bar{h}\left[T_a - T_c\right]dt \tag{40}$$

where $\bar{h}$ is the average convective heat transfer coefficient within the condenser at any given time. Considering that $\frac{m_{air}}{m_{MOF}} c_{p,a} << \omega_{cap} c_{p,w}$, the following relation can be obtained

$$\frac{A_c}{m_{MOF}} \int_{sunrise}^{sunset} \bar{h}\left[T_a - T_c\right]dt = \left(T_a - T_{dew}\right)\left(\omega_{cap} c_{p,w}\right) + \omega_{cap} h_{fg} \tag{41}$$

Here, to ensure a sufficiently large condenser surface, a minimum value of $\bar{h}$ was assumed for the case of film condensation (rather than dropwise condensation with higher heat transfer rate) on a vertical channel by using $Nu = 3.36$ throughout the condensation period using a correlation in the literature (*32*). It should be noted that accurate calculation of $\bar{h}$ is possible through advanced numerical simulation or experimental measurement with the identical geometrical constrains and boundary conditions which would result in a better estimation of the required cooling energy and condenser design. Here, we considered that the release of water occurred at 65°C and the condenser temperature was the same as the dew point ($T_c = T_a$). The total area required for condensation versus amount of MOF was calculated for different condenser temperatures and two Nusselt numbers ($Nu = 3.36$ and $Nu = 1.18$) which are plotted in the fig. S75. In the current design, the total area of 3100 cm^2 allowed for a sufficiently large case to enclose the water sorption unit and provided an adequately large surface for the condensation of the released water from up to 2.5 kg of MOF-801/G. Less than 1% variation in cooling area was observed by neglecting the sensible cooling. This implies that the minimum cooling energy required for the condensation of released water can be determined by neglecting the sensible cooling as follows

$$q_{c.min} \geq m_{MOF} \omega_{cap} h_{fg} \tag{42}$$

Although increasing the size of the cooling surface provides more cooling energy for condensation, there is a theoretical limit for the volume of the condenser. The humidity ratio (w in $kg_{(water)}\ kg_{(dry\ air)}^{-1}$) in the vicinity of the condenser can be related to the relative humidity according to

$$w = 10^4 RH / \left[e^{5294/(T_c+273.15)} - 1.61\times10^4 RH \right] \tag{43}$$

Considering that the *RH* of 100% is required for the condensation, then

$$\frac{\omega_{cap} m_{MOF}}{\rho_{air} V_c} = 10^6 / \left[e^{5294/(T_c+273.15)} - 1.61\times10^6 \right] \tag{44}$$

With the ratio known for A_c and m_{MOF} from equation (39), the maximum length of the condenser ($L_{c,max}$) can be expressed as follows

$$L_{c,max} = \frac{\omega_{cap} m_{MOF} \left[e^{5294/(T_c+273.15)} - 1.61\times10^6 \right]}{A_c \rho_{air} 10^6} \tag{45}$$

Considering the minimum amount of the MOF of 0.4 kg, ω_{cap} = 0.14, A_c = 3100 cm^2, T_c = 30°C, then $L_{c,max}$ = 3.16 m. In the current design, L_c = 25.4 cm which allowed to fully saturate the condenser when $\omega_{rel} = 0.08\omega_{cap}$.

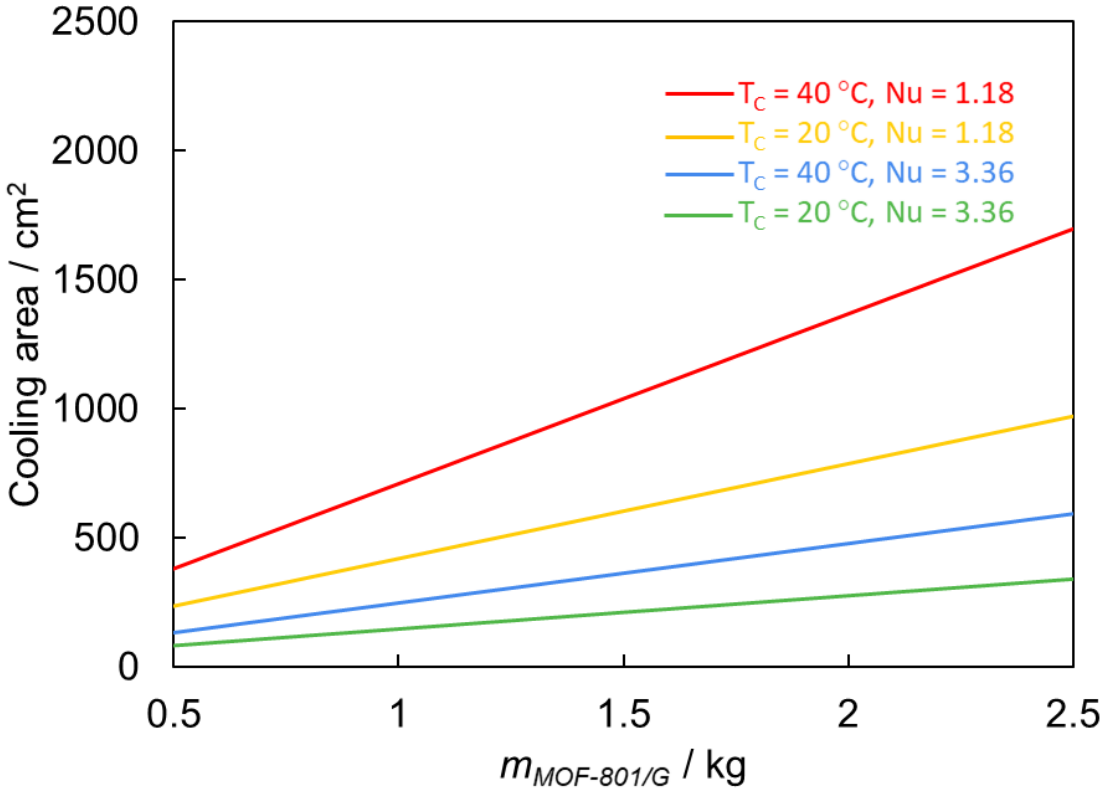

fig. S75. Variations of the size of the cooling surface with the amount of MOF-810/G for a temperature of 65°C for the released water, a condenser temperature of 20° and 40°C, and average heat condensation Nusselt numbers of 3.36 and 1.18. The cooling surface of 3100 cm^2 ensure enough cooling energy at the high condenser temperature (40°C) and low heat transfer rate (*Nu* = 1.18).

section S10. Harvesting experiments at Scottsdale, AZ, under desert conditions

The description of the setup for the harvesting experiment conducted at Scottsdale, Arizona, United States in late October is described in the main text. Figure S76-S77 show the temperature and relative humidity profile for two runs using 1.65 and 0.825 kg of MOF-801/G, respectively. Figure S78 describes the exterior insulation used in these experiments.

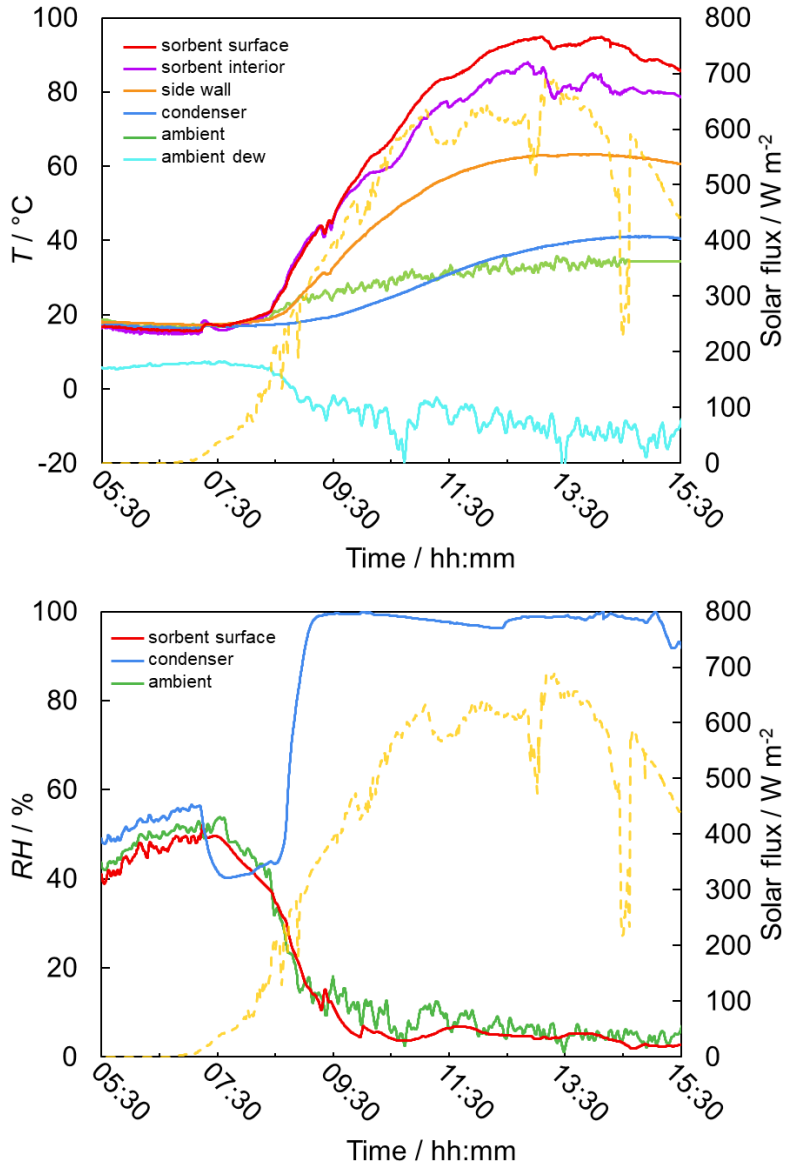

fig. S76. Relative humidity and temperature profiles for 1.65 kg of MOF-801/G under desert conditions. The temperature (top) and relative humidity (bottom) profiles recorded during water harvesting under desert conditions using 1.65 kg of MOF-801/G. 55 g of liquid water was collected. Release efficiency: 94%, collection efficiency: 25%, WHC efficiency: 24%, productivity: 33 g kg^{-1}.

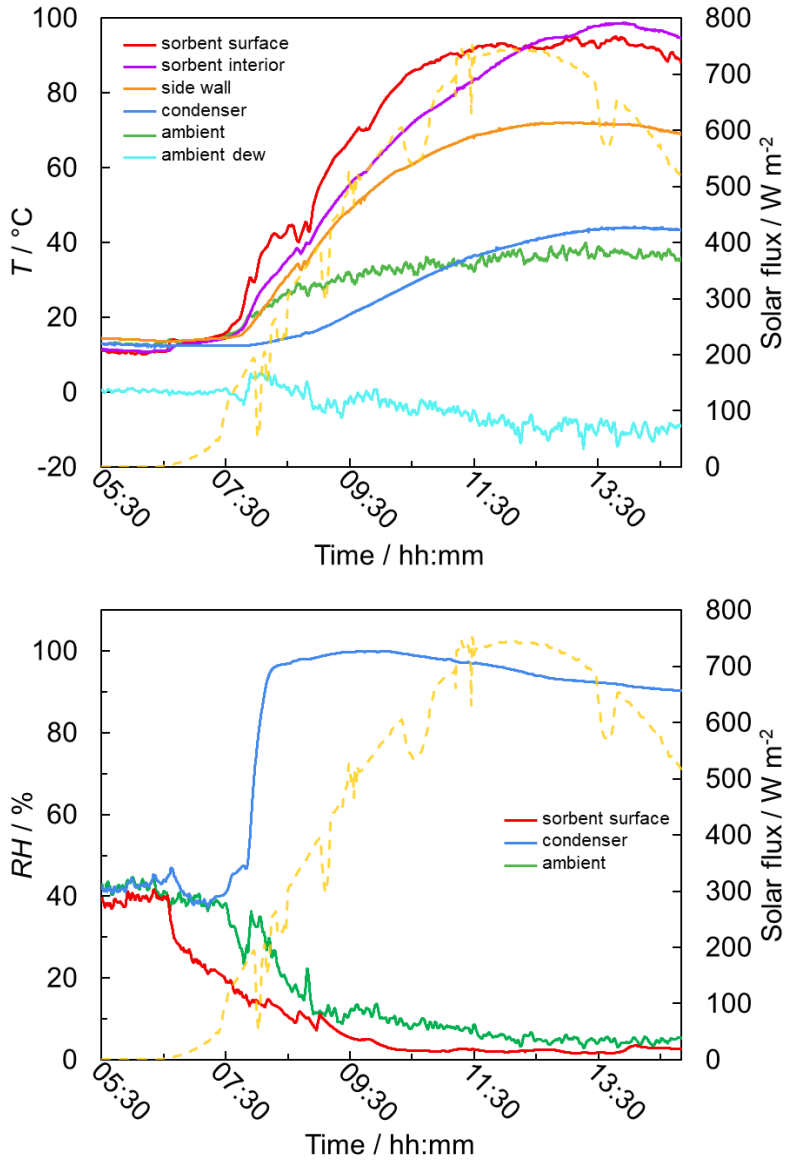

fig. S77. Relative humidity and temperature profiles for 0.825 kg of MOF-801/G under desert conditions. The temperature (top) and relative humidity (bottom) profiles recorded during water harvesting under desert conditions using 0.825 kg of MOF-801/G. 55 g of liquid water was collected. Release efficiency: 92%, collection efficiency: 56%, WHC efficiency: 51%, productivity: 67 g kg^{-1}.

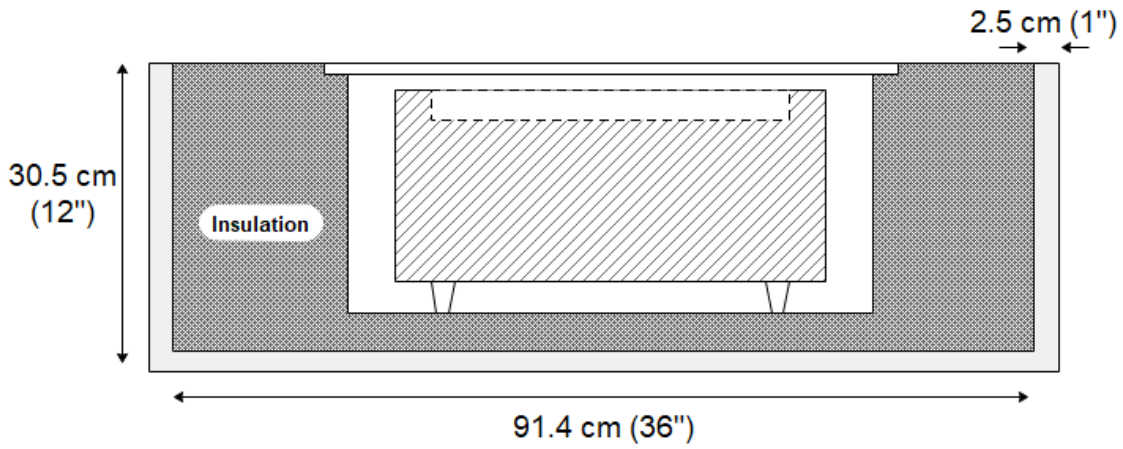

fig. S78. Schematic of the exterior insulation (soil) surrounding the case of the water harvester in desert climate.

section S11. Chemical analysis of collected water samples and MOF chemical stability

Activated microcrystalline powder MOF-801 was placed into an NMR tube with D_2O. ^{1}H-NMR spectra were recorded prior to heating the NMR tube for two hours at 85 C and after heating. Chemical shifts are reported in parts per million (ppm) with reference to the appropriate residual solvent signal from deuterated solvents. ^{1}H NMR: D_2O δ: 4.79 ppm, DMSO-d_6 δ: 2.50 ppm. Traces of *N*,*N*-dimethylformamide, *N*,*N*-dimethylamine and formic acid were found to be present in the sample, presumably due to non-ideal activation procedures. After heating the MOF powder in deuterated water, traces of these compounds remained unchanged. No traces of fumaric acid were found leaching out of the MOF, confirming its hydrolytic stability.

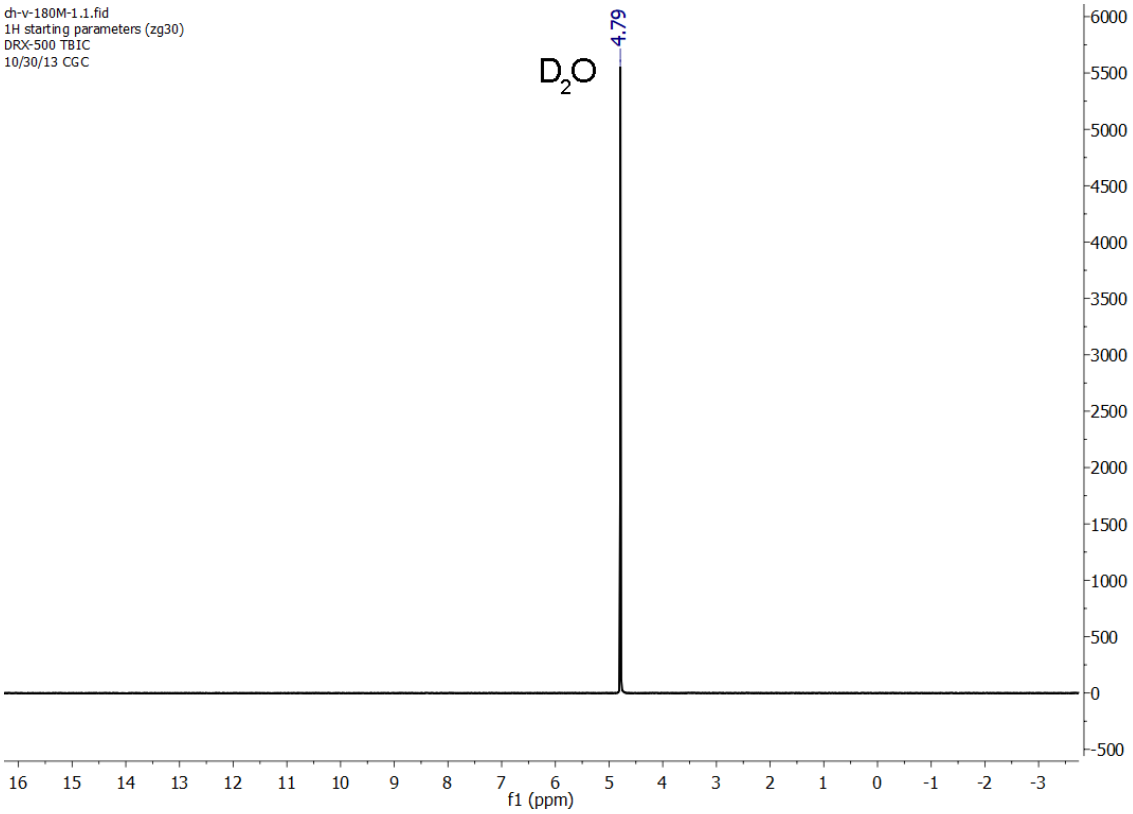

fig. S79. ^{1}H-NMR spectrum of pure D_2O before heating.

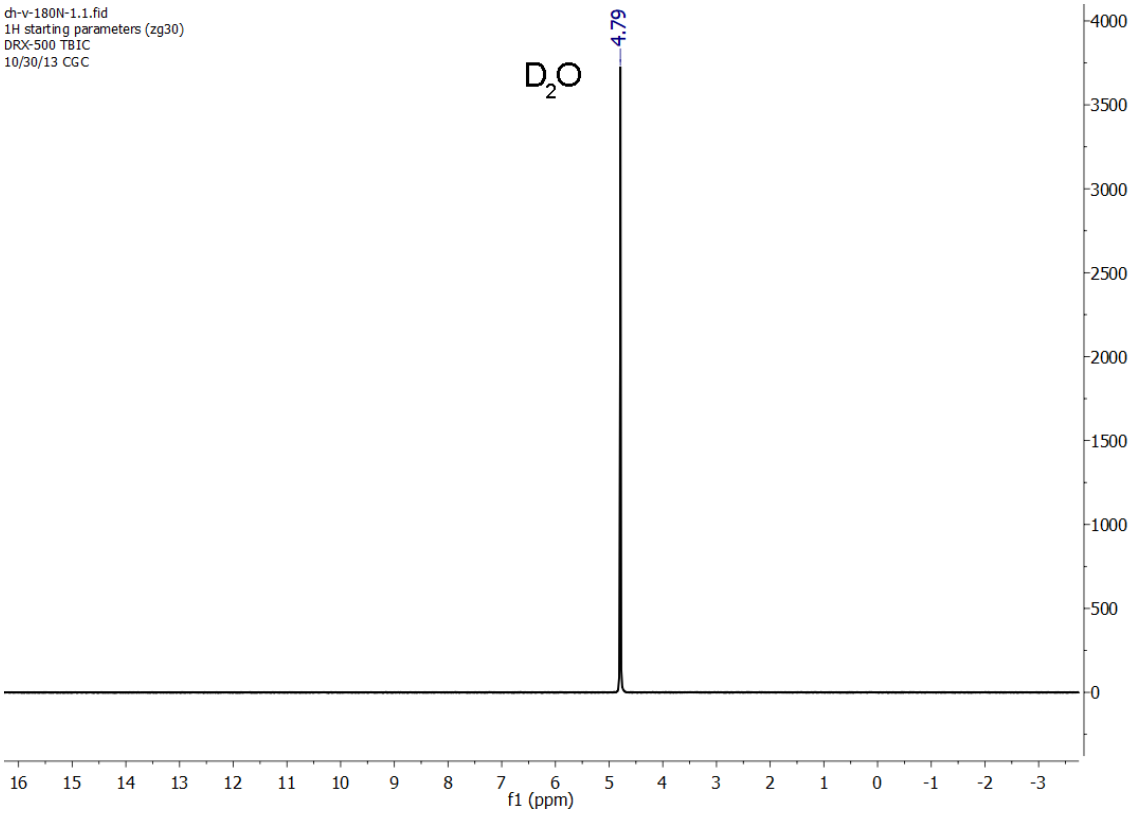

fig. S80. ^{1}H-NMR spectrum of pure D_2O after heating.

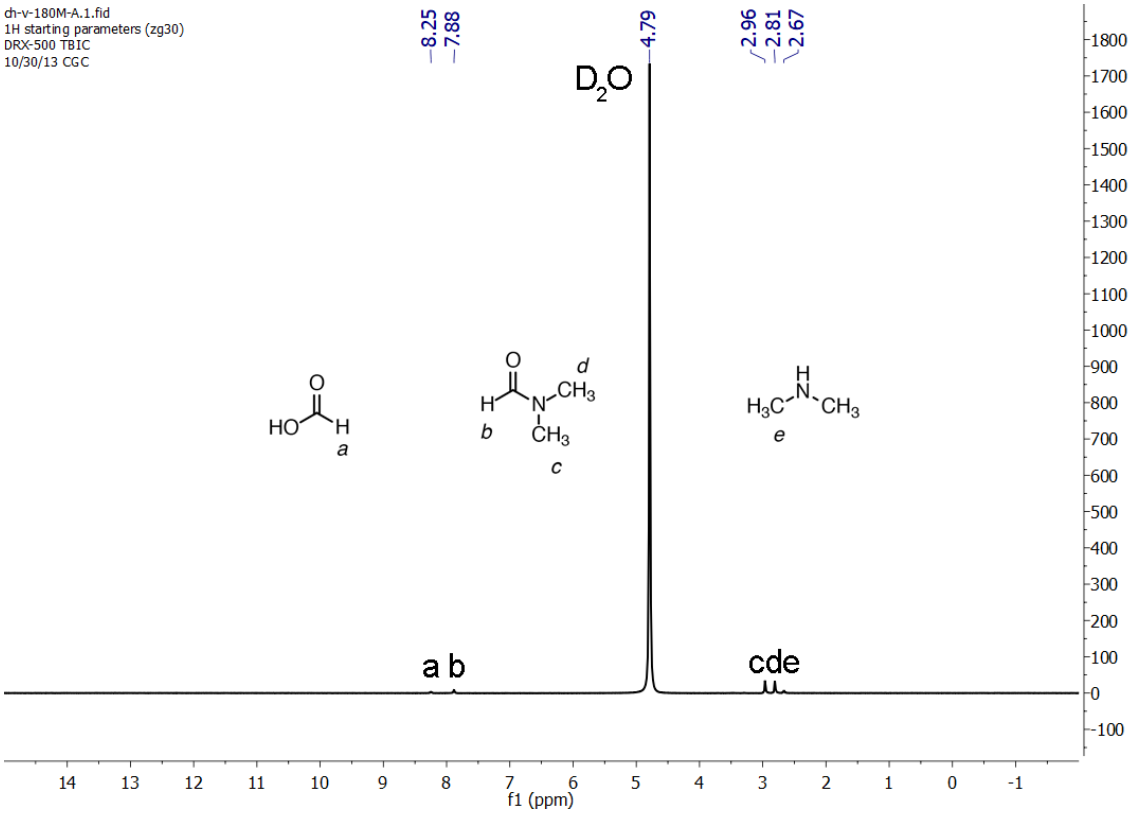

fig. S81. ^{1}H-NMR spectrum of MOF-801 in D_2O before heating. Observed signals: formic acid (8.25 ppm), *N*,*N*-dimethylformamide (7.88, 2.96, 2.81 ppm), *N*,*N*-dimethylamine (2.67 ppm).

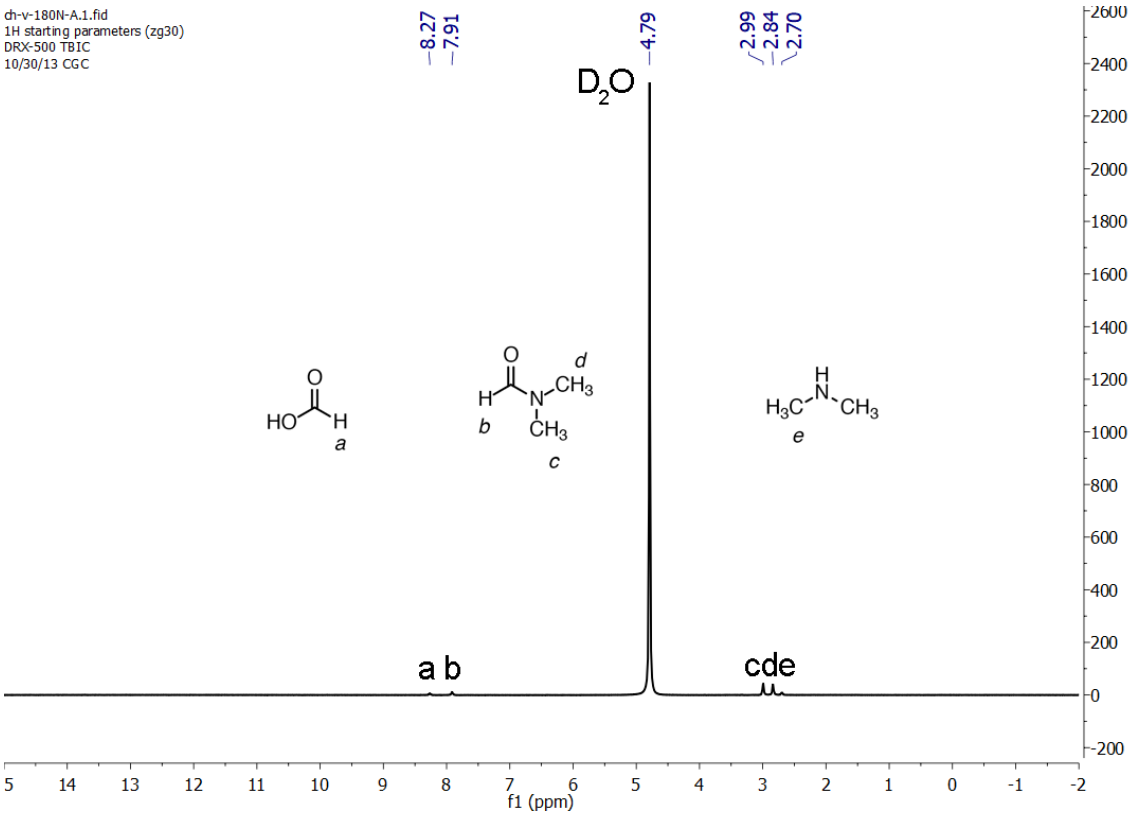

fig. S82. ^{1}H-NMR spectrum of MOF-801 in D_2O after heating. Observed signals: formic acid (8.27 ppm), *N*,*N*-dimethylformamide (7.91, 2.99, 2.84 ppm), *N*,*N*-dimethylamine (2.70 ppm).

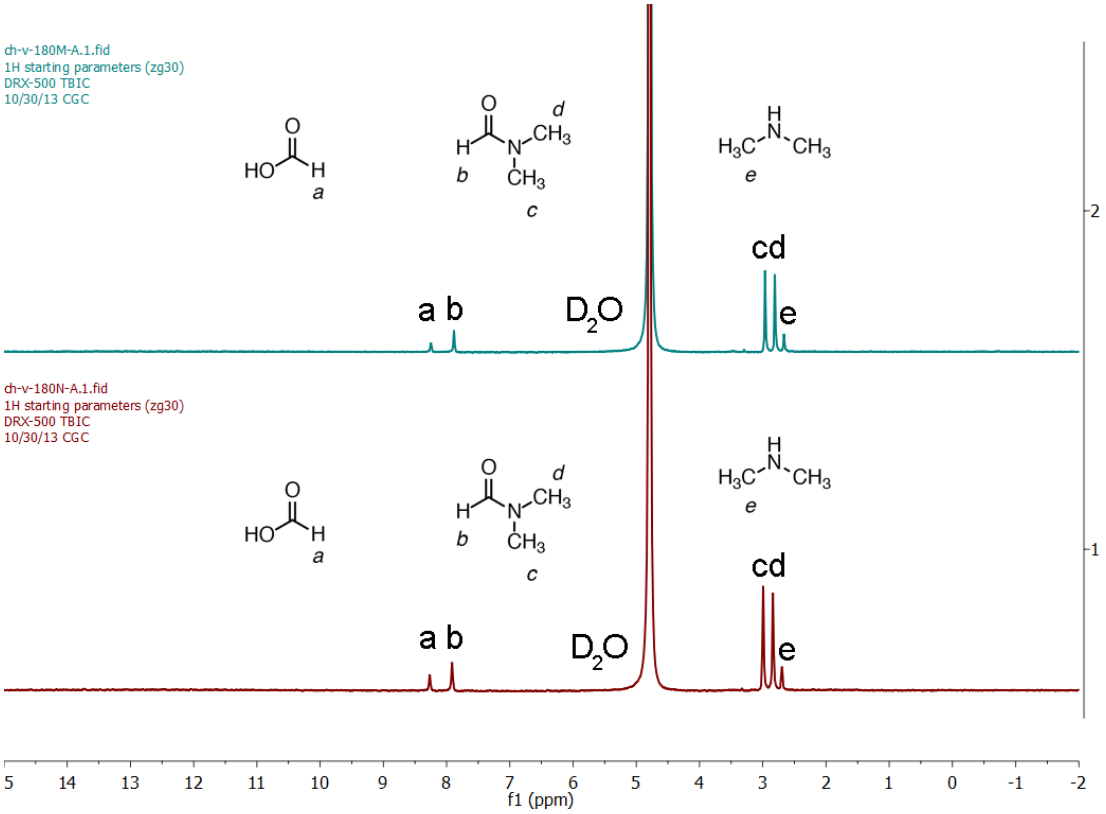

fig. S83. ^{1}H-NMR spectra of MOF-801 in D_2O: Overlay of before/after heating.

4 ml of water were taken out of a 37 ml batch of water collected using 0.825 kg of MOF-801/G under low flux, and placed into a 4 ml vial. The water was evaporated overnight at 100°C. The vial was rinsed with 0.6 ml of DMSO-d_6 and an ^{1}H-NMR spectrum was recorded. No organic impurities soluble in DMSO were found.

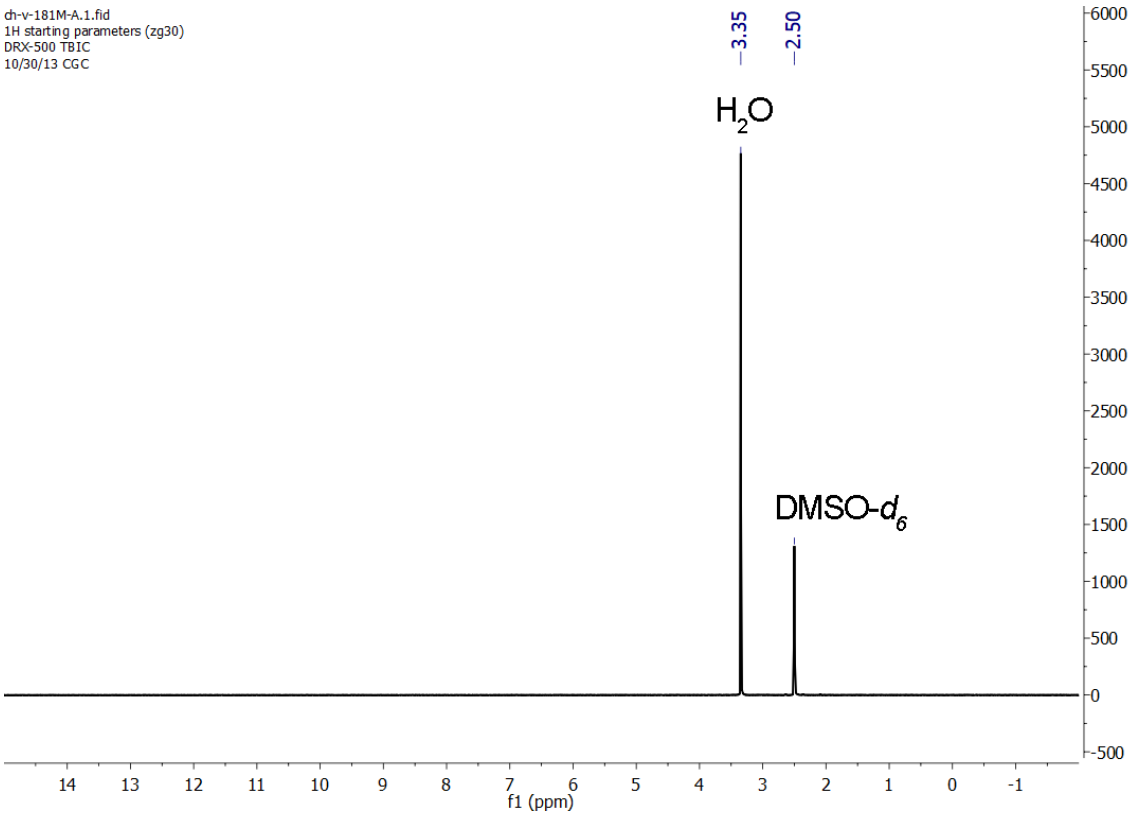

fig. S84. ^{1}H-NMR spectrum of water collected using 0.825 kg of MOF-801/G. Observed signal: water (3.35 ppm).

Activated microcrystalline MOF-303 powder was placed into an NMR tube with D_2O. ^{1}H-NMR spectra were recorded prior to heating the NMR tube for two hours at 85°C and after heating. Chemical shifts are reported in parts per million (ppm) with reference to appropriate residual solvent signal from the deuterated solvents. ^{1}H NMR: D_2O δ: 4.79 ppm, DMSO-d_6 δ: 2.50 ppm. Traces of methanol were found to be present in the sample, presumably due to non-ideal activation procedure. After heating the MOF powder in deuterated water, the traces of compounds mentioned above remained. No traces of 3,5-pyrazoledicarboxylic acid were found leaching out of the MOF, confirming its hydrolytic stability.

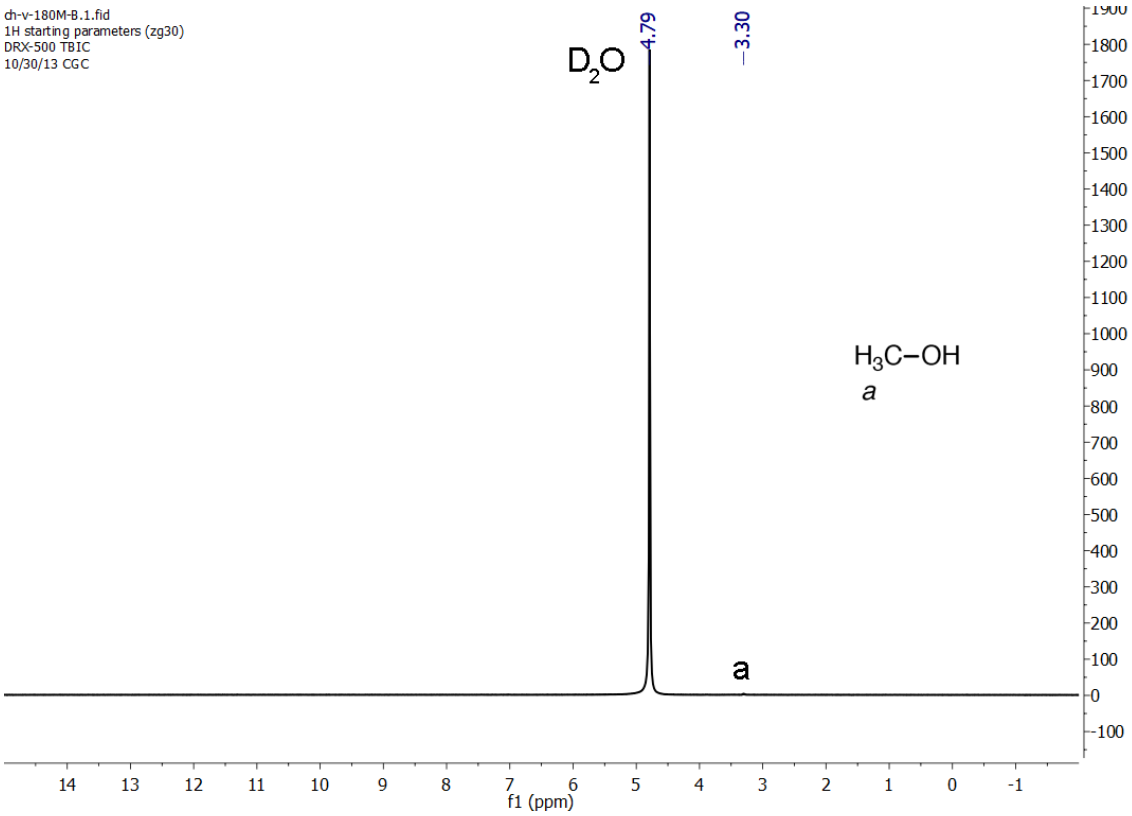

fig. S85. ^{1}H-NMR spectrum of MOF-303 in D_2O before heating. Observed signal: methanol (3.30 ppm).

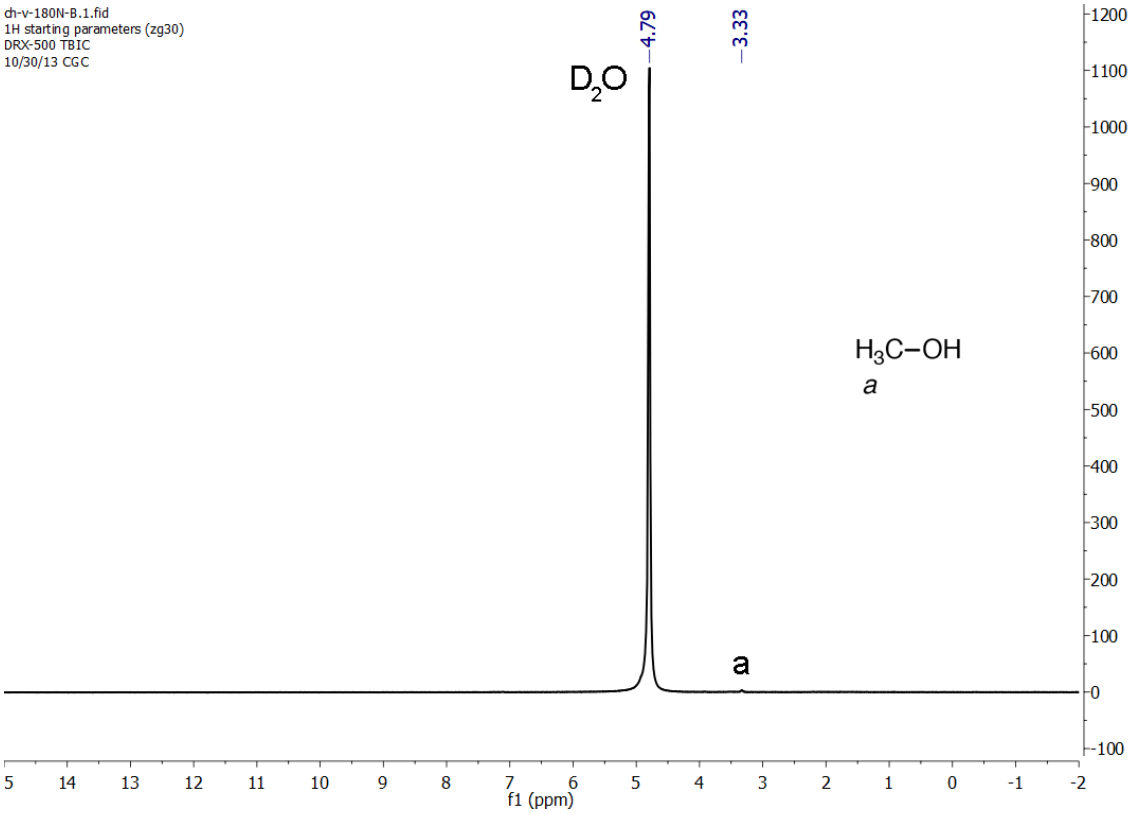

fig. S86. ^{1}H-NMR spectrum of MOF-303 in D_2O after heating.

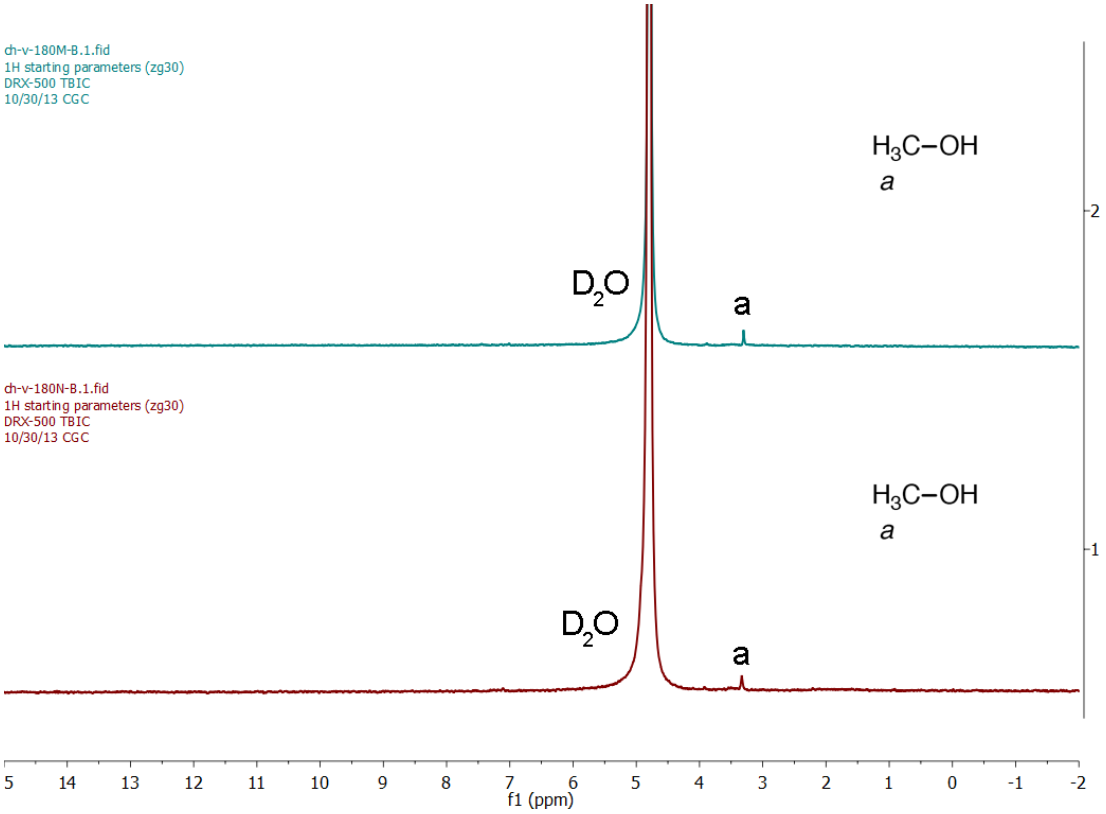

fig. S87. ^{1}H-NMR spectra of MOF-303 in D_2O: Overlay of before/after heating.

4 ml of water were taken out of a 105 ml batch of water collected using 0.600 kg of MOF-303/G under high flux, and placed into a 4 ml vial. The water was evaporated overnight at 100°C. The vial was rinsed with 0.6 ml DMSO-d_6 and an ^{1}H-NMR spectrum was recorded. No organic impurities soluble in DMSO were found.

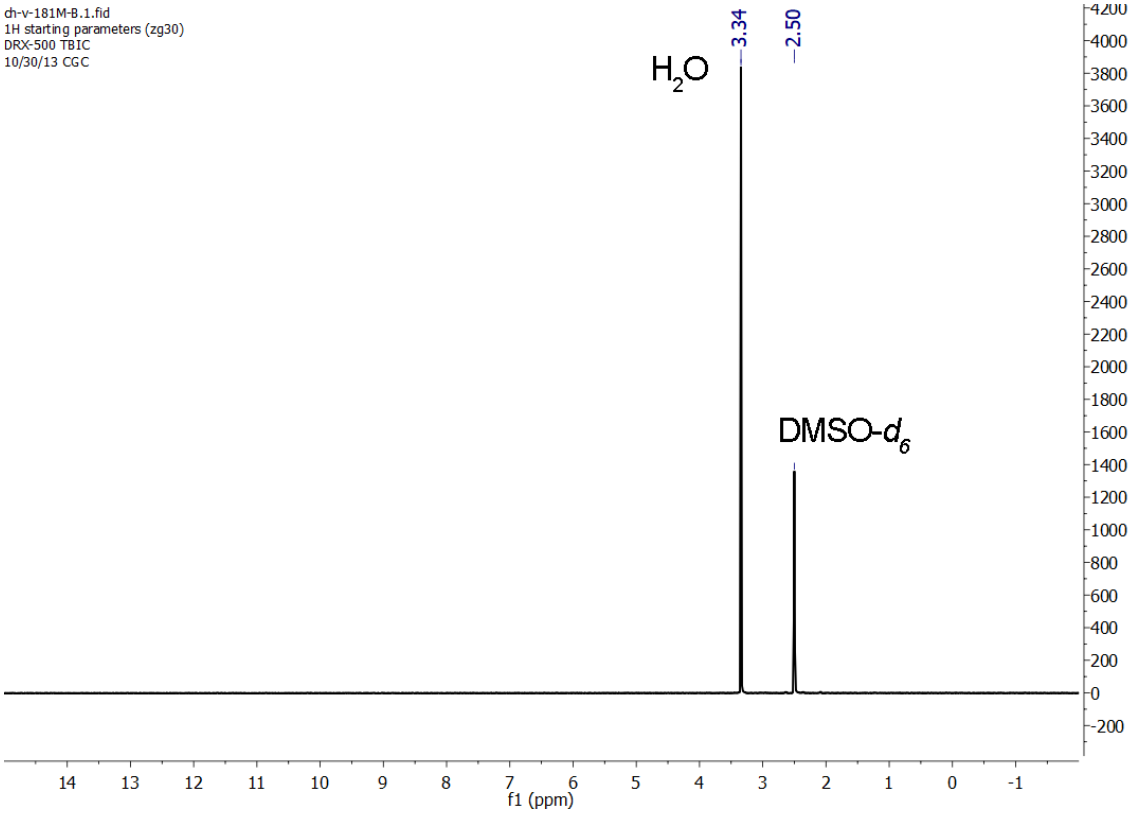

fig. S88. ^{1}H-NMR spectrum of water collected using 0.600 kg of MOF-303/G. Observed signal: water (3.34 ppm).

20 ml of water were taken out of a 65 ml batch of water collected using 1.65g of MOF-801/G under high flux, and placed into a 45 ml centrifuge tube. The sample was centrifuged for 30 minutes at 12000 rpm. The supernatant was collected and placed into a 20 ml scintillation vial, and the water was evaporated overnight at 100°C. The vial was rinsed with 10 ml of 2% v/v aqueous nitric solution and analyzed with ICP. Next, concentrations of standard zirconium solutions were used for the signal vs. concentration calibration curve: 0, 0.005, 0.05, 0.5, 5 ppm. The amount of zirconium in analyzed sample was found to be 0.009 ppm, indicating that the MOF-801 sample does not decompose during water harvesting.

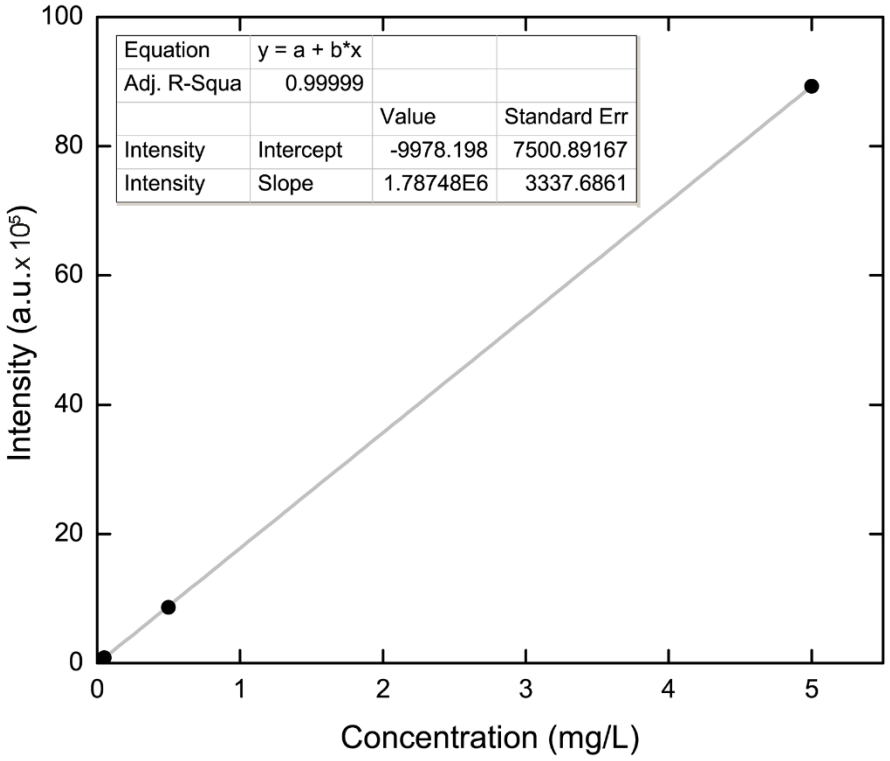

fig. S89. The calibration curve for zirconium standard solutions. The intensity of zirconium signal for the analyzed sample is 22639.7 a.u.

20 ml of water were taken out of a 105 ml batch of water collected using 0.600 kg of MOF-303/G under high flux, and placed into a 45 ml centrifuge tube. The sample was centrifuged for 30 minutes at 12000 rpm. The supernatant was collected and placed into a 20 ml scintillation vial, and the water was evaporated overnight at 100°C. The vial was rinsed with 10 ml of 2% v/v aqueous nitric solution and analyzed with ICP. Next concentrations of standard aluminum solutions were used for the signal vs. concentration calibration curve: 0, 0.005, 0.05, 0.5, 5 ppm. The amount of aluminum in analyzed sample was found to be 0.005 ppm, indicating that the MOF-303 sample does not decompose during water harvesting.

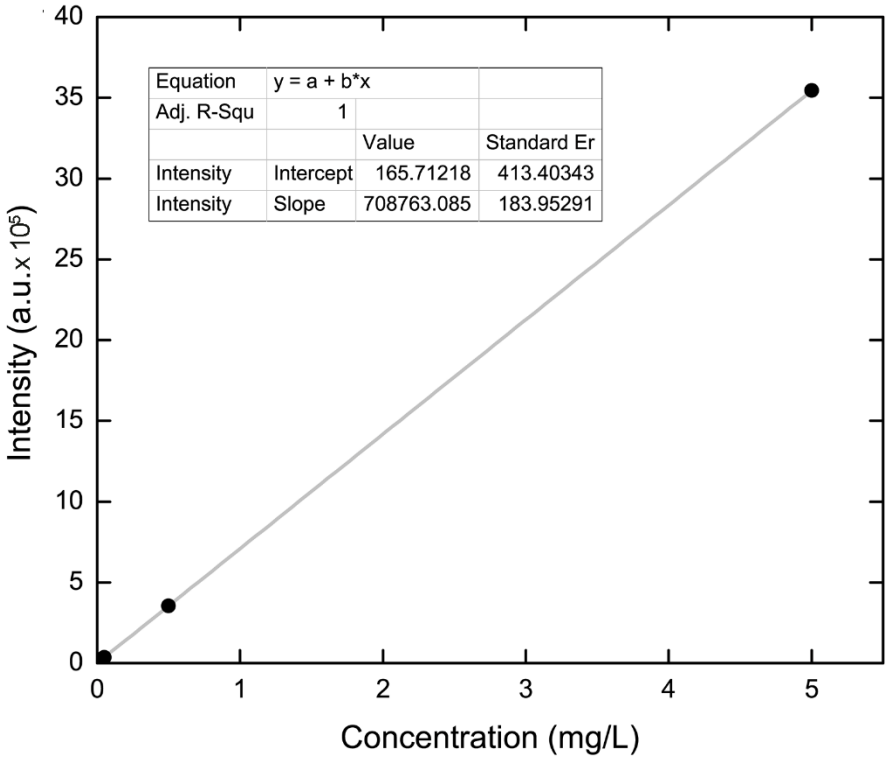

fig. S90. The calibration curve for aluminum standard solutions. The intensity of aluminum signal for the analyzed sample is 7739.6 a.u.

section S12. Movies of the water production experiment

The multimedia files for the water production experiment including movies of water condensation and of droplet formation and running liquid water can be downloaded from the *Science Advances* website.

movie S1. Initial stage of water condensation on the side walls of the case at 10,000% speed.

movie S2. Formation of running droplets of water on the side walls of the case at 10,000% speed.

movie S3. Coalescence of water droplets into puddles of liquid water at the condenser at 700% speed.

movie S4. Collision of puddles of liquid water at the bottom of the case at 1000% speed.